DHI-WASY Software

FEFLOW®

Finite Element Subsurface Flow
& Transport Simulation System

White Papers
Vol. IV

DHI-WASY GmbH

DHI-WASY GmbH,
Waltersdorfer Straße 105, D-12526 Berlin, Germany
Phone: +49-30-67 99 98-0, Fax: +49-30-67 99 98-99
E-Mail: mail@dhi-wasy.de

Contents

Reactive multi-species transport

1

H.-J. G. Diersch[a], A. Pönitz[a], D. Etcheverry[b] & Y. Rossier[b]

[a]*WASY Institute for Water Resources Planning and Systems Research, Berlin, Germany*
[b]*Sita Remediation SAS, Meyzieu, France*

1.1 Introduction

Starting with release 5.2, FEFLOW[5] solves reactive multi-species transport processes in multi-dimensional (2D, 3D) porous media under variably saturated, variable-density and nonisothermal conditions involving an arbitrary number of species. A given species can be either *mobile*, i.e., associated with a fluid (aqueous) phase, or *immobile*, i.e., associated with a solid phase. Chemicals in a fluid phase are subject to advection and dispersion, while in a solid phase there is no advection and dispersion.

FEFLOW provides enhanced tools in introducing and editing reactive multi-species transport problems. A powerful new *reaction kinetics editor*, FEMATHED, allows the user to freely define chemical or biochemical reactions in a fully graphics-based and interactive manner without requiring any programming or code compiling. Furthermore, the rate equations can be combined with conditional (if-else) expressions allowing a high degree of freedom in formulating the chemical reaction kinetics. FEFLOW incorporates a fast code interpreter for the user-defined reactions. The computational performance is comparable to precompiled code. Precompiled code versions of reaction kinetics are available for reactions of the degradation, Arrhenius and Monod type.

1.2 Theory

1.2.1 Reaction kinetics

1.2.1.1 Symbolic reaction stoichiometry

The basis of the chemical modeling represents the equations of reactions r which can be written in their general stoichiometric symbolic form[4] (symbols are summarized in the Appendix *Notation*):

$$|\nu_{1r}|A_1 + |\nu_{2r}|A_2 + \ldots + |\nu_{N^\circ r}|A_{N^\circ} \rightarrow |\nu_{(N^\circ+1)r}|B_{(N^\circ+1)} + |\nu_{(N^\circ+2)r}|B_{(N^\circ+2)} + \ldots + |\nu_{Nr}|B_N \qquad (1\text{-}1)$$

for $N° < N$ ($N°$ = number of reactants)
and $r = 1, \ldots, N_r$

which is related and quantified by the stoichiometric coefficients $|\nu_{kr}|$. The algebraic stoichiometric numbers ν_{kr} are subject to:

$$\nu_{kr} < 0 \quad \text{for} \quad 1 \le k \le N° \quad \text{(reactants)}$$
$$\nu_{kr} > 0 \quad \text{for} \quad N° < k \le N \quad \text{(products)}.$$

In (1-1) A and B represent chemical species (reactants and products, respectively) and the symbol $\rightarrow$ identifies the direction of the irreversible (nonequilibrium) reactions.

1.2.1.2 Examples

To illustrate the symbolic reaction stoichiometry (1-1) we exemplify the following reactions occurring in different applications of subsurface mass transport simulations.

(i) Pyrite oxidation
One mechanism involves oxidation of pyrite by O_2. Another possible mechanism for the oxidation of pyrite is the reaction with Fe(III) as the oxidant. These reactions for the pyrite oxidation read[19]:

$$\left.\begin{aligned} FeS_2 + \frac{7}{2}O_2 + H_2O &\rightarrow Fe^{+2} + 2SO_4^{2-} + 2H^+ \\ FeS_2 + 14Fe^{3+} + 8H_2O &\rightarrow 15Fe^{2+} + 2SO_4^{2-} + 16H^+ \end{aligned}\right\} \quad (1\text{-}2)$$

(ii) Aerobic biodegradation of BTEX
The overall aerobic reaction stoichiometry for a fuel hydrocarbon (e.g., benzene) can be written as[1,3]

$$C_6H_6 + 7.5O_2 \rightarrow 6CO_2 + 3H_2O \quad (1\text{-}3)$$

(iii) Degradation of BTEX using multiple electron acceptors
The biodegradation of BTEX can occur via five different degradation pathways[1,17,23]: aerobic respiration, denitrification, iron reduction, sulfate reduction and methanogenesis. Accordingly, the following instantaneous five reactions are given ($N_r = 5$):

$$\left.\begin{aligned} C_6H_6 + 7.5O_2 &\rightarrow 6CO_2 + 3H_2O \\ 6NO_3^- + 6H^+ + C_6H_6 &\rightarrow 6CO_2 + 6H_2O + 3N_2 \\ 30Fe(OH)_3 + 60H^+ + C_6H_6 &\rightarrow 6CO_2 + 78H_2O + 30Fe^{2+} \\ 3.75\,SO_4^{2-} + 7.5H^+ + C_6H_6 &\rightarrow 6CO_2 + 3H_2O + 3.75\,H_2S \\ C_6H_6 + 4.5\,H_2O &\rightarrow 2.25\,CO_2 + 3.75\,CH_4 \end{aligned}\right\} \quad (1\text{-}4)$$

(iv) Leaching of low-grade uranium ores
Two principal types of low-grade uranium ores are uraninite (UO_2) and pitchblende (U_3O_8). Typical reaction equations may be written as[16]

$$\left.\begin{aligned} UO_2 + \frac{1}{2}O_2 + CO_3^{2-} + 2HCO_3^- &\rightarrow UO_2(CO_3)_3^{4-} + H_2O \\ U_3O_8 + \frac{1}{2}O_2 + 3CO_3^{2-} + 6HCO_3^- &\rightarrow 3UO_2(CO_3)_3^{4-} + 3H_2O \end{aligned}\right\} \quad (1\text{-}5)$$

consisting of four reactants ($N° = 4$) for each reaction.

(v) Radionuclide decay chain of uranium
The radionuclide decay of ^{238}U occurs in the following decay series of serial and parallel reactions (note that U - uranium, Th - thorium, Pa - protactinium, Ra - radium, Rn - radon, Po - polonium, Pb - lead, Bi - bismuth, At - astatine, Tl - thallium)[12]:

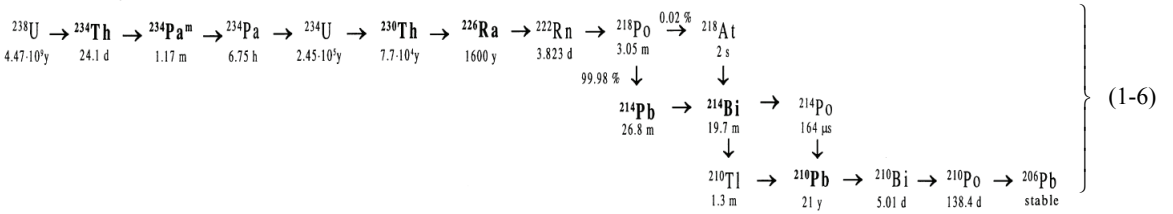

(1-6)

1.2.2 Governing transport equations

1.2.2.1 Basic balance statements

The mass conservation of chemical species in the fluid f and solid s phases of a porous medium can be concisely written in the following form[4,5,8,14], assuming that each species k exists (per definition) only in one phase (f or s):

$$\frac{\partial}{\partial t}(\varepsilon_\alpha C_k^\alpha) - \nabla\cdot(\boldsymbol{D}_k^\alpha\cdot\nabla C_k^\alpha) + \nabla\cdot(\boldsymbol{q}^\alpha C_k^\alpha) - \varepsilon_\alpha Q_k^\alpha = R_k \qquad \begin{cases} \alpha = f, s \ \text{(fluid, solid)} \\ \boldsymbol{q}^\alpha = D_{d_k}^\alpha \equiv \boldsymbol{0} \quad \text{for} \quad \alpha = s \ \text{(solid)} \\ k = 1, \ldots, N \end{cases} \tag{1-7}$$

$$\left.\begin{aligned} R_k &= \varepsilon_\alpha R_{\text{hom}_k}^\alpha + R_{\text{het}_k} \\ \sum_{k=1}^{N} R_k &= 0 \\ \boldsymbol{D}_k^\alpha &= (\varepsilon_\alpha D_{d_k}^\alpha + \beta_T \|\boldsymbol{q}\|^\alpha)\boldsymbol{I} + (\beta_L - \beta_T)\frac{\boldsymbol{q}^\alpha \otimes \boldsymbol{q}^\alpha}{\|\boldsymbol{q}\|^\alpha} \end{aligned}\right\} \tag{1-8}$$

where each species, labeled by the subscript k, is associated with a particular phase $\alpha \in (f, s)$, where f and s indicate the fluid and the solid phase, respectively. In (1-7) we have

C_k^α = concentration of species k of α-phase;

$\boldsymbol{D}_k^\alpha$ = tensor of hydrodynamic dispersion of species k of α-phase;

$D_{d_k}^\alpha$ = coefficient of molecular diffusion of species k of α-phase;

$\boldsymbol{I}$ = unit tensor;

k = species indicator, $k = 1, \ldots, N$;

N = total number of chemical species;
Q_k^α = zero-order nonreactive production term of α-phase;
$\boldsymbol{q}^\alpha$ = $\varepsilon_\alpha \boldsymbol{v}^\alpha$, Darcy flux of α-phase;
$\boldsymbol{v}^\alpha$ = pore velocity of α-phase;
R_k = bulk rate of chemical reaction of species k;
$R^\alpha_{\text{hom}_k}$ = homogeneous rate of reaction of species k within the α-phase;
R_{het_k} = heterogeneous rate reaction of species k associated with different phases;
α = phase indicator, $\alpha = f, s, \ldots$;
β_L, β_T = longitudinal and transverse dispersivity of porous medium, respectively.
ε_α = volume fraction of α-phase;

Considering the fluid phase as a wetting liquid in an unsaturated porous medium, it is often convenient to express the volume fraction ε_α for the fluid phase $\alpha = f$ and for one solid phase $\alpha = s$ in a porous medium as

$$\varepsilon_f = s_f \varepsilon \qquad \varepsilon_s = 1 - \varepsilon \tag{1-9}$$

with

$$0 < s_f \leq 1 \tag{1-10}$$

where ε is the porosity (void space) of the porous medium, and s_f is the saturation referring to the fluid (liquid) f-phase. For saturated media we have $s_f \equiv 1$ and $\varepsilon_f = \varepsilon$. Using (1-9) the balance equations (1-7) can be written for the f- and s-phases in their specific forms according to

$$\begin{aligned} \frac{\partial}{\partial t}(s_f \varepsilon C_k^f) - \nabla \cdot (\boldsymbol{D}_k^f \cdot \nabla C_k^f) + \nabla \cdot (\boldsymbol{q}^f C_k^f) - s_f \overline{Q}_k^f &= R_k \qquad \text{fluid phase } f \text{ and species } k \\ \frac{\partial}{\partial t}(\varepsilon_s C_k^s) - \overline{Q}_k^s &= R_k \qquad \text{solid phase } s \text{ and species } k \end{aligned} \tag{1-11}$$

where

$\overline{Q}_k^f$ = εQ_k^f, bulk zero-order nonreactive production term of fluid phase and fluid species k;
$\overline{Q}_k^s$ = $\varepsilon_s Q_k^s$, bulk zero-order nonreactive production term of solid phase and solid species k;

1.2.2.2 Generalized balance equations

Let us assume that a species k of a fluid phase f for (1-11) can also be subjected to a reversible equilibrium reaction with a species, say m, which is associated with the solid phase s, so that we find the adsorption isotherms[8]

$$|\nu_k| A_k^f + |\nu_m| A_m^s \;\leftrightarrows\; |\nu_k| A_k^s + |\nu_m| A_m^f \tag{1-12}$$

where A_k^f is the fluid species, A_m^s is the sorbed (solid) species, and the symbol $\leftrightarrows$ identifies reversible reactions at a chemical equilibrium. The law of mass action

(LMA)[8] can be used to explicitly express the (sorbed) solid species C_m^s as a function of the (dissolved) fluid species C_k^f, *viz.*[8],

$$C_m^s = \chi_k \cdot C_k^f \tag{1-13}$$

where $\chi_k = \chi_k(C_k^f)$ is the adsorption function, which can be dependent on C_k^f.

As stated in[8] for equilibrium reactions (adsorptions) under unsaturated conditions the solid volume fraction ε_s should be subdivided into chemically active and inactive parts $\varepsilon_s = \varepsilon_{s^{\text{active}}} + \varepsilon_{s^{\text{inactive}}}$. It is shown[8] that $\varepsilon_{s^{\text{active}}} = f(\varepsilon_f)\varepsilon_s \approx s_f \varepsilon_s$. Then, the balance equations for species k and m can be written as

$$\begin{aligned} \frac{\partial}{\partial t}(s_f \varepsilon C_k^f) - \nabla \cdot (\boldsymbol{D}_k^f \cdot \nabla C_k^f) + \nabla \cdot (\boldsymbol{q}^f C_k^f) - s_f \overline{Q}_k^f &= R_k^* \\ \frac{\partial}{\partial t}(\varepsilon_{s^{\text{active}}} C_m^s) - \varepsilon_{s^{\text{active}}} Q_m^s &= R_m^* \end{aligned} \tag{1-14}$$

(Note that we identify the chemical rates by * for species having additionally equilibrium reactions.) Using the adsorption isotherms (1-13) the following balance equation results after summation of both equations (1-14)

$$\frac{\partial}{\partial t}(s_f \varepsilon \Re_k C_k^f) - \nabla \cdot (\boldsymbol{D}_k^f \cdot \nabla C_k^f) + \nabla \cdot (\boldsymbol{q}^f C_k^f) \tag{1-15}$$

$$-s_f \underbrace{(\overline{Q}_k^f + \overline{Q}_m^s)}_{\overline{Q}_k} = \underbrace{R_k^* + R_m^*(C_k^f)}_{R_k}$$

where the *retardation factor* $\Re_k$ is introduced according to[8]

$$\Re_k = 1 + \frac{1-\varepsilon}{\varepsilon}\chi_k \tag{1-16}$$

with the *adsorption function* χ_k

$$\chi_k = \begin{cases} \kappa & \text{Henry} \\ \dfrac{k_1}{1 + k_2 C_k^f} & \text{Langmuir} \\ b_1 C_k^{f(b_2 - 1)} & \text{Freundlich} \end{cases} \tag{1-17}$$

where $\kappa, k_1, k_2, b_1, b_2$ correspond to sorption coefficients.

1.2.2.3 Final equations

In summation we use the following generalized mass balance equations for chemically reacting species k in the fluid phase f and solid phase s (species $k = 1, \ldots, N$ are subjected to nonequilibrium reactions):

$$\left.\begin{aligned} \frac{\partial}{\partial t}(s_f \varepsilon \Re_k C_k^f) - \nabla \cdot (\boldsymbol{D}_k^f \cdot \nabla C_k^f) + \nabla \cdot (\boldsymbol{q}^f C_k^f) - s_f \overline{Q}_k &= R_k \qquad \text{fluid phase } f \text{ and species } k \\ \frac{\partial}{\partial t}(\varepsilon_s C_k^s) - \overline{Q}_k^s &= R_k \qquad \text{solid phase } s \text{ and species } k \end{aligned}\right\} \tag{1-18}$$

$$\left.\begin{aligned} \Re_k &= 1 + \frac{1-\varepsilon}{\varepsilon}\chi_k \\ \boldsymbol{D}_k^f &= (s_f \varepsilon D_{d_k}^f + \beta_T \|\boldsymbol{q}\|^f)\boldsymbol{I} + (\beta_L - \beta_T)\frac{\boldsymbol{q}^f \otimes \boldsymbol{q}^f}{\|\boldsymbol{q}\|^f} \end{aligned}\right\} \tag{1-19}$$

For depth-integrated *2D horizontal* formulations of the basic equations (1-18) and (1-19) the following specific multi-species transport equations in confined and unconfined aquifers result:

$$\left.\begin{aligned} \frac{\partial}{\partial t}(\varepsilon \overline{\Re}_k C_k^f) - \nabla \cdot (\overline{\boldsymbol{D}}_k^f \cdot \nabla C_k^f) + \nabla \cdot (\overline{\boldsymbol{q}}^f C_k^f) - \widehat{Q}_k &= BR_k \qquad \text{fluid phase } f \text{ and species } k \\ \frac{\partial}{\partial t}(\varepsilon_s B C_k^s) - \widehat{Q}_k^s &= BR_k \qquad \text{solid phase } s \text{ and species } k \end{aligned}\right\} \tag{1-20}$$

$$\left.\begin{aligned} \overline{\Re}_k &= B\left(1 + \frac{1-\varepsilon}{\varepsilon}\chi_k\right) \\ \overline{\boldsymbol{D}}_k^f &= (\varepsilon B D_{d_k}^f + \beta_T \|\overline{\boldsymbol{q}}\|^f)\boldsymbol{I} + (\beta_L - \beta_T)\frac{\overline{\boldsymbol{q}}^f \otimes \overline{\boldsymbol{q}}^f}{\|\overline{\boldsymbol{q}}\|^f} \end{aligned}\right\} \tag{1-21}$$

and

$$\left.\begin{aligned} \overline{\boldsymbol{q}}^f &= B\boldsymbol{q}^f \\ \widehat{Q}_k &= B\overline{Q}_k \\ \widehat{Q}_k^s &= B\overline{Q}_k^s \end{aligned}\right\} \tag{1-22}$$

where B denotes the aquifer thickness (cf. FEFLOW's Reference Manual[5]).

1.2.3 Reaction rates R_k

For a given number of irreversible reactions $r = 1, \ldots, N_r$ the reaction rate R_k for a species k can be expressed in the following general form[4,8,14]

$$R_k = \sum_{r=1}^{N_r} \nu_{kr} r_r \qquad (k = 1, \ldots, N) \qquad (1\text{-}23)$$

where

N_r = number of reactions;
r_r = rate of reaction associated with the type of reaction r;
ν_{kr} = stoichiometric number of species k and reaction r.

Reactive systems can be broadly classified into simple and complex kinetic systems. The former consists of unimolecular and bimolecular reactions while the latter encompasses opposing, concurrent, and consecutive reactions. According to the mechanism of a given reaction, the functional form of r_r can be very complicated.

A typical *constitutive representation* of r_r has a functional

$$r_r = r_r(C_1^\alpha, \ldots, C_N^\alpha, s_f, \varepsilon) \qquad \alpha = f \text{ or } s \qquad (1\text{-}24)$$

which can be developed by a polynomial expression of low order in terms of concentrations C_k^α for simple kinetic systems or more complex rate expressions of higher order, cf. Fig. 1.1. We can distinguish the following classes of rate expressions.

1.2.3.1 Degradation type kinetics

For degradation type kinetics the rate r_r can be developed in a polynomial representation of low order, *viz.*,

$$r_r = \sum_{m=1}^{N} B_{rm} (C_m^\alpha)^{n_m} \qquad \alpha = f \text{ or } s \qquad (1\text{-}25)$$

where B_{rm} is a rate constant and $n_m \geq 0$ corresponds to an exponent of species m. For such a type the reaction rate R_k (1-23) can be written in the general form

$$\begin{aligned} R_k &= \sum_{m=1}^{N} \kappa_m (C_m^\alpha)^{n_m} \qquad \alpha = f \text{ or } s \\ &= \kappa_1 (C_1^\alpha)^{n_1} + \kappa_2 (C_2^\alpha)^{n_2} + \ldots + \kappa_N (C_N^\alpha)^{n_N} \end{aligned} \qquad (1\text{-}26)$$

where κ_m $(m = 1, \ldots, N)$ are bulk rate constants that can be dependent on ε and s_f.

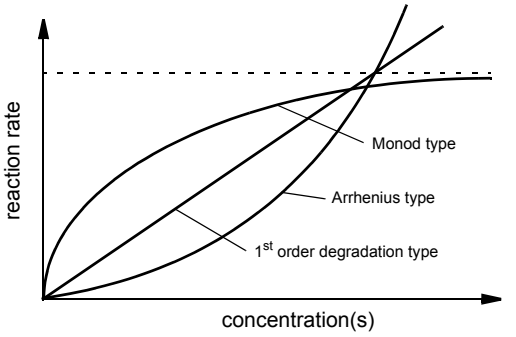

Figure 1.1 Variation of reaction rate with concentration.

1.2.3.2 Arrhenius type kinetics

The Arrhenius type kinetics are expressed by a polynomial representation of higher order for the rate r_r,

$$r_r = \sum_{m=1}^{N} B^1_{rm}(C^\alpha_m)^{n_m} + \sum_{m,n}^{N} B^2_{rm}(C^\alpha_m)^{n_m}(C^\beta_n)^{n_n} + \ldots \quad (1\text{-}27)$$
$$+ \prod_{m=1}^{N} B^N_{rm}(C^\alpha_m)^{n_m}$$

introducing a number of rate constants $B^1_{rm}, \ldots, B^N_{rm}$. Accordingly, we find for the reaction rate R_k (1-23) the following expression

$$R_k = \kappa_1(C^\alpha_1)^{n_1} + \kappa_2(C^\alpha_1)^{n_1}(C^\alpha_2)^{n_2} + \ldots \quad (1\text{-}28)$$
$$+ \kappa_N \prod_{m=1}^{N}(C^\alpha_m)^{n_m} \qquad \alpha = f \text{ or } s$$

where κ_m $(m = 1, \ldots, N)$ are bulk rate constants that can be dependent on ε and s_f. For the species exponents $n_m \geq 0$ is assumed.

1.2.3.3 Monod type kinetics

Monod type kinetics describe more complex biochemical reaction systems. Monod was the first to recognize that the growth rate of a microbial population is restricted by the concentration of the growth-limiting substrate. Monod established that the form of the relationship was analogous to the Michaelis-Menten enzyme kinetics equation[8]. Its mathematical representation can be written as

$$r_r = \sum_{m=1}^{N} A_{rm}(C^\alpha_r)^{n_r} \prod_{n=1}^{N^\circ}\left(\frac{B_{rn}(C^\alpha_n)^{n_n}}{D^{n_n}_{rn} + E_{rn}(C^\alpha_n)^{n_n}}\right) \quad (1\text{-}29)$$

where $A_{rm}, B_{rn}, D_{rn}, E_{rn}$ are rate constants. In (1-29) C^α_n represents the concentration of the growth-limiting substrate. The term B_{rn} is the maximum specific growth rate and the term D_{rn} denotes the half-saturation constant and is defined as the concentration C^α_n at which the microorganisms grow at half the maximum specific growth rate B_{rn}. The half-saturation constant may be viewed as a measure of the affinity the microorganisms have for the growth-limiting substrate: (1) the lower the value of D_{rn}, the greater the capacity to grow rapidly in an environment with low concentrations of growth-limiting substrate, and (2) the lower the value of D_{rn}, the lower the growth-limiting substrate concentration at which the maximum specific growth rate B_{rn} is attained.

Using (1-29) with (1-23) the following expression for the reaction rate R_k is obtained:

$$R_k = \kappa_1^1 (C_1^\alpha)^{n_1} \left(\frac{b_{11}^1 (C_2^\alpha)^{n_2}}{d_{11}^1 + e_{11}^1 (C_2^\alpha)^{n_2}} \right) + \kappa_2^1 (C_1^\alpha)^{n_1} \left(\frac{b_{21}^1 (C_2^\alpha)^{n_2}}{d_{21}^1 + e_{21}^1 (C_2^\alpha)^{n_2}} \right) \left(\frac{b_{22}^1 (C_3^\alpha)^{n_3}}{d_{22}^1 + e_{22}^1 (C_3^\alpha)^{n_3}} \right) \tag{1-30}$$

$$+ \kappa_3^1 (C_1^\alpha)^{n_1} \left(\frac{b_{31}^1 (C_2^\alpha)^{n_2}}{d_{31}^1 + e_{31}^1 (C_2^\alpha)^{n_2}} \right) \left(\frac{b_{32}^1 (C_3^\alpha)^{n_3}}{d_{32}^1 + e_{32}^1 (C_3^\alpha)^{n_3}} \right) \left(\frac{b_{33}^1 (C_4^\alpha)^{n_4}}{d_{33}^1 + e_{33}^1 (C_4^\alpha)^{n_4}} \right) + \ldots + \kappa_N^1 (C_1^\alpha)^{n_1} \prod_{n=2}^{N^\circ} \left(\frac{b_{Nn}^1 (C_n^\alpha)^{n_n}}{d_{Nn}^1 + e_{Nn}^1 (C_n^\alpha)^{n_n}} \right)$$

$$+ \kappa_1^2 (C_2^\alpha)^{n_2} \left(\frac{b_{11}^2 (C_1^\alpha)^{n_1}}{d_{11}^2 + e_{11}^2 (C_1^\alpha)^{n_1}} \right) + \kappa_2^2 (C_2^\alpha)^{n_2} \left(\frac{b_{21}^2 (C_1^\alpha)^{n_1}}{d_{21}^2 + e_{21}^2 (C_1^\alpha)^{n_1}} \right) \left(\frac{b_{22}^2 (C_3^\alpha)^{n_3}}{d_{22}^2 + e_{22}^2 (C_3^\alpha)^{n_3}} \right)$$

$$+ \kappa_3^2 (C_2^\alpha)^{n_2} \left(\frac{b_{31}^2 (C_1^\alpha)^{n_1}}{d_{31}^2 + e_{31}^2 (C_1^\alpha)^{n_1}} \right) \left(\frac{b_{32}^2 (C_3^\alpha)^{n_3}}{d_{32}^2 + e_{32}^2 (C_3^\alpha)^{n_3}} \right) \left(\frac{b_{33}^2 (C_4^\alpha)^{n_4}}{d_{33}^2 + e_{33}^2 (C_4^\alpha)^{n_4}} \right) + \ldots + \kappa_N^2 (C_2^\alpha)^{n_2} \prod_{n=1, n \neq 2}^{N^\circ} \left(\frac{b_{Nn}^2 (C_n^\alpha)^{n_n}}{d_{Nn}^2 + e_{Nn}^2 (C_n^\alpha)^{n_n}} \right)$$

$$+ \ldots$$

$$+ \kappa_1^{N_r} (C_{N_r}^\alpha)^{n_{N_r}} \left(\frac{b_{11}^{N_r} (C_1^\alpha)^{n_1}}{d_{11}^{N_r} + e_{11}^{N_r} (C_1^\alpha)^{n_1}} \right) + \kappa_2^{N} (C_{N_r}^\alpha)^{n_{N_r}} \left(\frac{b_{21}^{N_r} (C_1^\alpha)^{n_1}}{d_{21}^{N_r} + e_{21}^{N_r} (C_1^\alpha)^{n_1}} \right) \left(\frac{b_{22}^{N_r} (C_2^\alpha)^{n_2}}{d_{22}^{N_r} + e_{22}^{N_r} (C_2^\alpha)^{n_2}} \right)$$

$$+ \kappa_3^{N_r} (C_{N_r}^\alpha)^{n_{N_r}} \left(\frac{b_{31}^{N_r} (C_1^\alpha)^{n_1}}{d_{31}^{N_r} + e_{31}^{N_r} (C_1^\alpha)^{n_1}} \right) \left(\frac{b_{32}^{N_r} (C_2^\alpha)^{n_2}}{d_{32}^{N_r} + e_{32}^{N_r} (C_2^\alpha)^{n_2}} \right) \left(\frac{b_{33}^{N_r} (C_3^\alpha)^{n_3}}{d_{33}^{N_r} + e_{33}^{N_r} (C_3^\alpha)^{n_3}} \right) + \ldots + \kappa_N^{N_r} (C_{N_r}^\alpha)^{n_{N_r}} \prod_{n=1, n \neq N_r}^{N^\circ} \left(\frac{b_{Nn}^{N_r} (C_n^\alpha)^{n_n}}{d_{Nn}^{N_r} + e_{Nn}^{N_r} (C_n^\alpha)^{n_n}} \right)$$

or in general terms

$$R_k = \sum_{m=1}^{N_r} \sum_{n=1}^{N} \kappa_n^m (C_m^\alpha)^{n_m} \prod_{i=1, i \neq m}^{N^\circ} \left(\frac{b_{ni}^m (C_i^\alpha)^{n_i}}{d_{ni}^m + e_{ni}^m (C_i^\alpha)^{n_i}} \right) \qquad \alpha = f \text{ or } s \tag{1-31}$$

with bulk rate constants $\kappa_n^m, b_{ni}^m, d_{ni}^m, e_{ni}^m$ $(m = 1, \ldots, N_r)(n = 1, \ldots, N)(i = 1, \ldots, N^\circ)$, which can be dependent on ε and s_f. For the species exponents $n_n \geq 0$ is assumed. In (1-31) b_{ni}^m is a maximum specific growth rate and d_{ni}^m is a half-saturation constant.

1.2.3.4 Parallel irreversible and reversible reactions

Let us consider the case when irreversible and reversible reactions occur together. For instance, species are dissolved in the fluid phase f and undergo a decay reaction. At the same time, these species may be adsorbed at the solid phase s in equilibrium reactions. As exemplified for a reactive eight-species system with a degradation-type kinetics we can write

$$\begin{array}{ccccccc} A^{\mathrm{f}} & \longrightarrow & B^{\mathrm{f}} & \longrightarrow & C^{\mathrm{f}} & \longrightarrow & D^{\mathrm{f}} \\ \downarrow\uparrow & & \downarrow\uparrow & & \downarrow\uparrow & & \downarrow\uparrow \\ E^{\mathrm{s}} & \longrightarrow & F^{\mathrm{s}} & \longrightarrow & G^{\mathrm{s}} & \longrightarrow & H^{\mathrm{s}} \end{array} \qquad (1\text{-}32)$$

Accordingly, the following balance equations result for the mobile species k of the fluid phase f

$$\frac{\partial}{\partial t}(s_f \varepsilon C_k^f) - \nabla \cdot (\boldsymbol{D}_k^f \cdot \nabla C_k^f) + \nabla \cdot (\boldsymbol{q}^f C_k^f) - s_f \overline{Q}_k^f \qquad (1\text{-}33a)$$
$$= s_f \varepsilon (\vartheta_{k-1} C_{k-1}^f - \vartheta_k C_k^f) \qquad (k = A, B, C, D)$$

and for the immobile species m associated with the solid phase s

$$\frac{\partial}{\partial t}(s_f \varepsilon_s C_m^s) - s_f \varepsilon_s Q_m^s \qquad (1\text{-}33b)$$
$$= s_f \varepsilon_s (\vartheta_{m-1} C_{m-1}^s - \vartheta_m C_m^s) \qquad (m = E, F, G, H)$$

where ϑ_k are decay rate constants. Using the adsorption isotherms (1-13) with

$$C_m^s = \chi_k \cdot C_k^f \qquad (k = A, B, C, D) \quad (m = E, F, G, H) \qquad (1\text{-}34)$$

and assuming that the decay rate constants ϑ_k are identical for the fluid and solid phases, the balance equations (1-33a) and (1-33b) can be simply added. This yields the following overall species mass balance equation

$$\frac{\partial}{\partial t}(s_f \varepsilon \Re_k C_k^f) - \nabla \cdot (\boldsymbol{D}_k^f \cdot \nabla C_k^f) + \nabla \cdot (\boldsymbol{q}^f C_k^f) - s_f \overline{Q}_k \qquad (1\text{-}35a)$$
$$= R_k \qquad (k = A, B, C, D)$$

with the reaction rates of a degradation type

$$R_k = s_f \varepsilon (\vartheta_{k-1} \Re_{k-1} C_{k-1}^f - \vartheta_k \Re_k C_k^f) \qquad (1\text{-}35b)$$
$$(k = A, B, C, D)$$

where $\Re_k$ denotes the retardation factor defined by (1-16).

Similar to (1-35b), rate expressions can be derived for more complex parallel reaction kinetics when all or only part of the species undergo a reversible equilibrium reaction (adsorption isotherms). Here, the corresponding species of the solid phase are substituted via the adsorption isotherms (1-13) and the balance equations for the fluid and solid species are added, resulting in modified rate expressions R_k that incorporate the retardation factor $\Re_k$.

In the case of single-species transport ($N = 1$) the reacting species is always considered as mobile. The reaction rate R_1 is then

$$R_1 = -s_f \varepsilon \vartheta_1 \Re_1 C_1^f$$

***Notice,** the decay rate ϑ_k can be expressed by the reaction half-life $t_{k,1/2}$ of species k in the form:*

$$\vartheta_k = \frac{\ln 2}{t_{k,1/2}}$$

where $\ln 2 = 0.693$.

1.3 Numerical Solution

1.3.1 Finite-element equation system

FEFLOW uses the finite-element method to solve the final mass balance equations (1-18) of species k in

the fluid *f* or solid phase *s*. It ends up with the following matrix system:

$$\boldsymbol{S} \cdot \frac{d\boldsymbol{C}}{dt} + \boldsymbol{K} \cdot \boldsymbol{C} - \boldsymbol{R} = \boldsymbol{0} \qquad \text{(1-36a)}$$

or

$$\begin{bmatrix} \boldsymbol{S}_1 & 0 & 0 & \dots & 0 \\ 0 & \boldsymbol{S}_2 & 0 & \dots & 0 \\ 0 & 0 & \boldsymbol{S}_3 & \dots & 0 \\ & & & \dots & \\ 0 & 0 & 0 & \dots & \boldsymbol{S}_N \end{bmatrix} \begin{Bmatrix} \frac{d\boldsymbol{C}_1}{dt} \\ \frac{d\boldsymbol{C}_2}{dt} \\ \frac{d\boldsymbol{C}_3}{dt} \\ \dots \\ \frac{d\boldsymbol{C}_N}{dt} \end{Bmatrix} + \begin{bmatrix} \boldsymbol{K}_1 & 0 & 0 & \dots & 0 \\ 0 & \boldsymbol{K}_2 & 0 & \dots & 0 \\ 0 & 0 & \boldsymbol{K}_3 & \dots & 0 \\ & & & \dots & \\ 0 & 0 & 0 & \dots & \boldsymbol{K}_N \end{bmatrix} \begin{Bmatrix} \boldsymbol{C}_1 \\ \boldsymbol{C}_2 \\ \boldsymbol{C}_3 \\ \dots \\ \boldsymbol{C}_N \end{Bmatrix} \qquad \text{(1-36b)}$$

$$- \begin{Bmatrix} \boldsymbol{R}_1 \\ \boldsymbol{R}_2 \\ \boldsymbol{R}_3 \\ \dots \\ \boldsymbol{R}_N \end{Bmatrix} = \begin{Bmatrix} 0 \\ 0 \\ 0 \\ \dots \\ 0 \end{Bmatrix}$$

where $\boldsymbol{S}_k = \boldsymbol{S}_k(\boldsymbol{C})$ $(k = 1, \dots, N)$ are the nonlinear storage matrices including retardation effects, $\boldsymbol{K}_k$ $(k = 1, \dots, N)$ are the 'conductance' matrices encompassing advection and dispersion effects, and $\boldsymbol{R}_k = \boldsymbol{R}_k(\boldsymbol{C})$ $(k = 1, \dots, N)$ are the chemical rate vectors, which represent nonlinear dependencies on the total concentration vector $\boldsymbol{C} = \{\boldsymbol{C}_1, \boldsymbol{C}_2, \boldsymbol{C}_3, \dots, \boldsymbol{C}_N\}$ according to the considered reaction kinetics. Furthermore, we note that there is no conductance $\boldsymbol{K}_k \equiv \boldsymbol{0}$ for a species *k* belonging to a solid phase *s*.

The matrix system (1-36a) can be highly nonlinear mainly due to the dependence of the reaction rate $\boldsymbol{R}$ on $\boldsymbol{C}$ so that an efficient numerical solution strategy is required here. One possibility would be the solution of the coupled matrix system (1-36a) in a direct and simultaneous manner. Although mathematically rigorous, practical implementation of that approach has been limited and is not generally applicable to large, geometrically complex and multidimensional problems because of the significant memory and/or computational burden. The size of the coefficient matrices $\boldsymbol{S}$ and $\boldsymbol{K}$ in the discretized system (1-36a) grows as a product of the number of nodes *NP* and the number of species *N*. In general, the direct approach involves solving a $NP \times N$ system of nonlinear equations at each time step. Furthermore, the system for a simultaneous solution can be ill-conditioned due to the significantly different scales of the processes involved. Alternatively, in order to reduce the computational requirements, a *decoupled* (or split-operator) solution strategy is preferred, in which the species equations are solved sequentially by using efficient iteration techniques. Kanney *et al*.[13] discuss different strategies of such split-operator approaches. Among a variety of split-operator techniques the sequential iterative approach (SIA) have proven superior and powerful. In FEFLOW, we prefer an adaptive error-controlled SIA strategy which is based on an efficient predictor-corrector time-stepping technique. In contrast to a common SIA technique the transport equations with the reaction terms are solved in an adaptive full time interval using predictor solutions to linearize the nonlinear reaction terms. The overall iteration control is fully embedded in a time-marching strategy via a sophisticated error-based time-step adaptation.

1.3.2 Adaptive predictor-corrector time-stepping solution strategy

The predictor-corrector solution strategy with automatically adapted time stepping has been shown very cost-efficient and robust for classes of nonlinear systems such as variable density[9] and/or variably saturated[6] problems. We also apply this technique for solving the present chemically reactive systems.

We rewrite the composed matrix system in separate matrix systems for each species k as follows

$$\boldsymbol{S}_k(\boldsymbol{C}) \cdot \dot{\boldsymbol{C}}_k + \boldsymbol{K}_k \cdot \boldsymbol{C}_k - \boldsymbol{R}_k(\boldsymbol{C}) = \boldsymbol{0} \quad (k = 1, \ldots, N) \quad (1\text{-}37)$$

or

$$\left.\begin{aligned} \boldsymbol{S}_1(\boldsymbol{C}_1, \ldots, \boldsymbol{C}_N) \cdot \dot{\boldsymbol{C}}_1 + \boldsymbol{K}_1 \cdot \boldsymbol{C}_1 - \boldsymbol{R}_1(\boldsymbol{C}_1, \ldots, \boldsymbol{C}_N) &= \boldsymbol{0} \\ \boldsymbol{S}_2(\boldsymbol{C}_1, \ldots, \boldsymbol{C}_N) \cdot \dot{\boldsymbol{C}}_2 + \boldsymbol{K}_2 \cdot \boldsymbol{C}_2 - \boldsymbol{R}_2(\boldsymbol{C}_1, \ldots, \boldsymbol{C}_N) &= \boldsymbol{0} \\ \boldsymbol{S}_3(\boldsymbol{C}_1, \ldots, \boldsymbol{C}_N) \cdot \dot{\boldsymbol{C}}_3 + \boldsymbol{K}_3 \cdot \boldsymbol{C}_2 - \boldsymbol{R}_3(\boldsymbol{C}_1, \ldots, \boldsymbol{C}_N) &= \boldsymbol{0} \\ \ldots & \\ \boldsymbol{S}_N(\boldsymbol{C}_1, \ldots, \boldsymbol{C}_N) \cdot \dot{\boldsymbol{C}}_N + \boldsymbol{K}_N \cdot \boldsymbol{C}_N - \boldsymbol{R}_N(\boldsymbol{C}_1, \ldots, \boldsymbol{C}_N) &= \boldsymbol{0} \end{aligned}\right\} \quad (1\text{-}38)$$

with $\dot{\boldsymbol{C}}_k = \dfrac{d\boldsymbol{C}_k}{dt} \quad (k = 1, \ldots, N)$.

The nonlinear matrix systems (1-37) are discretized in time t by using implicit time-stepping techniques. Considering $\boldsymbol{C}_k$ within the time interval $(t_n, t_n + \Delta t_n)$, where the subscript n denotes the time plane and Δt_n is a variable time step length, the implicit approximation of (1-37) yields

$$\left(\frac{\boldsymbol{S}_k(\boldsymbol{C})}{\theta \Delta t_n} + \boldsymbol{K}_k\right) \cdot \boldsymbol{C}_k^{n+1} = \boldsymbol{S}_k(\boldsymbol{C}) \cdot \left[\frac{\boldsymbol{C}_k^n}{\theta \Delta t_n} + \left(\frac{1}{\theta} - 1\right) \dot{\boldsymbol{C}}_k^{\,n}\right] \quad (1\text{-}39)$$

$$+ \boldsymbol{R}_k^{n+1}(\boldsymbol{C}) \qquad (k = 1, \ldots, N)$$

where n+1 identifies the new time solution and $\theta \in (\frac{1}{2}, 1)$ is a weighting factor used for the trapezoid rule (TR) of second-order accuracy and the backward Euler (BE) schemes of first-order accuracy in time t.

The system is nonlinear due to the dependence on $\boldsymbol{C} = \{\boldsymbol{C}_1, \boldsymbol{C}_2, \boldsymbol{C}_3, \ldots, \boldsymbol{C}_N\}$ and can be appropriately linearized by using the following adaptive predictor-corrector time-stepping strategy:

(Step 0 - Initialization) Computation of the initial acceleration vectors $\dot{\boldsymbol{C}}_k^{\,0}$ for $n = 0$ (once per k-species equation)

$$\boldsymbol{S}_k(\boldsymbol{C}^0) \cdot \dot{\boldsymbol{C}}_k^{\,0} = -\boldsymbol{K}_k \cdot \boldsymbol{C}_k^0 + \boldsymbol{R}_k(\boldsymbol{C}^0) \quad (k = 1, \ldots, N) \quad (1\text{-}40)$$

and guessing of an initial time step Δt_0. The initial systems (1-40) are solved with the initial concentration vector $\boldsymbol{C}^0 = \{\boldsymbol{C}_1^0, \boldsymbol{C}_2^0, \boldsymbol{C}_3^0, \ldots, \boldsymbol{C}_N^0\}$.

(Step 1 - Predictor solutions) Perform explicit predictor solutions for all species k by using the Adams-Bashforth (AB) or the forward Euler (FE) algorithm, respectively:

$$\boldsymbol{C}_k^{n+1,p} = \begin{cases} \boldsymbol{C}_k^n + \dfrac{\Delta t_n}{2}\left[2 + \dfrac{\Delta t_n}{\Delta t_{n-1}}\right] \dot{\boldsymbol{C}}_k^{\,n} - \dfrac{\Delta t_n}{\Delta t_{n-1}} \dot{\boldsymbol{C}}_k^{\,n-1} \\ \boldsymbol{C}_k^n + \Delta t_n \dot{\boldsymbol{C}}_k^{\,n} \qquad (k = 1, \ldots, N) \end{cases} \quad (1\text{-}41)$$

(Step 2 - Corrector solutions) Do corrector solution via the TR or BE schemes (1-39) by applying the predictor solution $\boldsymbol{C}^{n+1,p} = \{\boldsymbol{C}_1^{n+1,p}, \boldsymbol{C}_2^{n+1,p}, \boldsymbol{C}_3^{n+1,p}, \ldots, \boldsymbol{C}_N^{n+1,p}\}$ from (1-41) to linearize the species equations as

$$\left(\frac{\boldsymbol{S}_k(\boldsymbol{C}^{n+1,p})}{\theta\Delta t_n} + \boldsymbol{K}_k\right) \cdot \boldsymbol{C}_k^{n+1} = \boldsymbol{S}_k(\boldsymbol{C}^{n+1,p}) \cdot \left[\frac{\boldsymbol{C}_k^n}{\theta\Delta t_n} + \left(\frac{1}{\theta} - 1\right)\dot{\boldsymbol{C}}_k^{\,n}\right] + \boldsymbol{R}_k^{n+1}(\boldsymbol{C}^{n+1,p}) \quad (k = 1, \ldots, N) \tag{1-42}$$

(Step 3 - Updated time derivatives) Update the new time-derivative vectors by inverting the TR and BE schemes, respectively:

$$\dot{\boldsymbol{C}}_k^{\,n+1} = \begin{cases} \dfrac{2}{\Delta t_n}(\boldsymbol{C}_k^{n+1} - \boldsymbol{C}_k^n) - \dot{\boldsymbol{C}}_k^{\,n} \\ \dfrac{1}{\Delta t_n}(\boldsymbol{C}_k^{n+1} - \boldsymbol{C}_k^n) \quad (k = 1, \ldots, N) \end{cases} \tag{1-43}$$

(Step 4 - Error estimation) Compute the local truncation error for the AB/TR or FE/BE scheme, respectively:

$$\boldsymbol{d}_k^{n+1} = \begin{cases} \dfrac{\boldsymbol{C}_k^{n+1} - \boldsymbol{C}_k^{n+1,p}}{3\left(1 + \dfrac{\Delta t_{n-1}}{\Delta t_n}\right)} \\ \dfrac{1}{2}(\boldsymbol{C}_k^{n+1} - \boldsymbol{C}_k^{n+1,p}) \quad (k = 1, \ldots, N) \end{cases} \tag{1-44}$$

(Step 5 - Prediction of new time step) Predict the potential new k-specific time-step lengths from the error estimates (1-44) for each species k:

$$\Delta t_{n+1,k} = \Delta t_n \left(\frac{\delta}{\left\|\boldsymbol{d}_k^{n+1}\right\|}\right)^{1/\lambda} \quad (k = 1, \ldots, N) \tag{1-45}$$

where λ is 3 for the AB/TR and 2 for the FE/BE scheme, δ is a user-specified error tolerance ($\delta = 10^{-4} - 10^{-3}$ is typical), and $\|.\|$ is a norm to be chosen as the weighted RMS norm or, alternatively, the maximum norm, respectively:

$$\left\|\boldsymbol{d}_k^{n+1}\right\| = \begin{cases} \dfrac{1}{\boldsymbol{C}_k^{\max}}\left[\dfrac{1}{\mathrm{NP}}\left(\sum_{i=1}^{\mathrm{NP}} \left|\boldsymbol{d}_{ki}^{n+1}\right|^2\right)\right]^{1/2} \\ \dfrac{1}{\boldsymbol{C}_k^{\max}}\left(\max_i \left|\boldsymbol{d}_{ki}^{n+1}\right|\right) \quad (k = 1, \ldots, N) \end{cases} \tag{1-46}$$

where $\boldsymbol{C}_k^{\max}$ is the maximum concentration of species k at the time plane n+1, NP is the total number of spatially discretized points (nodes), and $\boldsymbol{d}_{ki}^{n+1}$ denotes the error of species equations k at the node i ($i = 1, \ldots, \mathrm{NP}$).

(Step 6 - Tactic of adaptive time stepping and error control) The following criteria are used to monitor the progress of the nonlinear solution:

1. If

$$\Delta t_{n+1,k} \geq \Delta t_n \tag{1-47a}$$

the solution $\boldsymbol{C}_k^{n+1}$ for the species equation k is accurate within the error bound defined by δ and the increase of the time step is always accepted.

2. If

$$\zeta \Delta t_n \le \Delta t_{n+1,k} \le \Delta t_n \tag{1-47b}$$

where ζ is typically 0.85, the kth solution $\boldsymbol{C}_k^{n+1}$ is accepted but the time step is not changed, i.e., $\Delta t_{n+1,k} = \Delta t_n$.

3. If

$$\Delta t_{n+1,k} < \zeta \Delta t_n \tag{1-47c}$$

the solution $\boldsymbol{C}_k^{n+1}$ cannot be accepted within the required error tolerance δ and has to be rejected. The proposed new time step size (1-45) has to be reduced according to

$$\Delta t_{n+1,k}^{*} = \frac{\Delta t_n^2}{\Delta t_{n+1,k}} \left(\frac{\delta}{\left\| \boldsymbol{d}_k^{n+1} \right\|} \right) \tag{1-47d}$$

and the solution is repeated for the time plane n+1 with $\Delta t_n = \Delta t_{n+1,k}^{*}$.

4. If the criteria (1-47a) and (1-47b) are satisfied by all species equations and the solutions $\boldsymbol{C}_k^{n+1}$ can be accepted for all species k within the required error tolerance δ, the new time step is determined from the minimum of the k-specific time step lengths, *viz.*,

$$\Delta t_{n+1} = \min_k (\Delta t_{n+1,k}) \tag{1-47e}$$

It is important to note that the error tolerance δ is the only user-specified parameter to control the entire nonlinear and transient solution process. The starting-up phase is still influenced by the initial time step Δt_0 which should be kept small. In practice, two further constraints for the time-step size have shown to be useful. Firstly, the time step should not exceed a maximum measure, i.e., $\Delta t_{n+1} \le \Delta t^{\max}$. Secondly, the rate for changing the time-step size $\Xi = \Delta t_{n+1} / \Delta t_n$ can also be limited, e.g., $\Xi \le \Xi^{\max}$ (say, 2 or 3).

The predictor-corrector strategy fully monitors the nonlinear and transient solution process via the time truncation error estimation in which the size of the time step is cheaply and automatically varied in accordance with the overall accuracy requirements. The time step is increased whenever possible and decreased only when necessary. It is evident to note that by monitoring the temporal accuracy requirements, at the same time the solution strategy provides an efficient control of the nonlinearities of the species transport equation system via the predictor solutions. Due to the power of the predictor-corrector strategy any additional iterative feedback within the adapted time steps can be avoided.

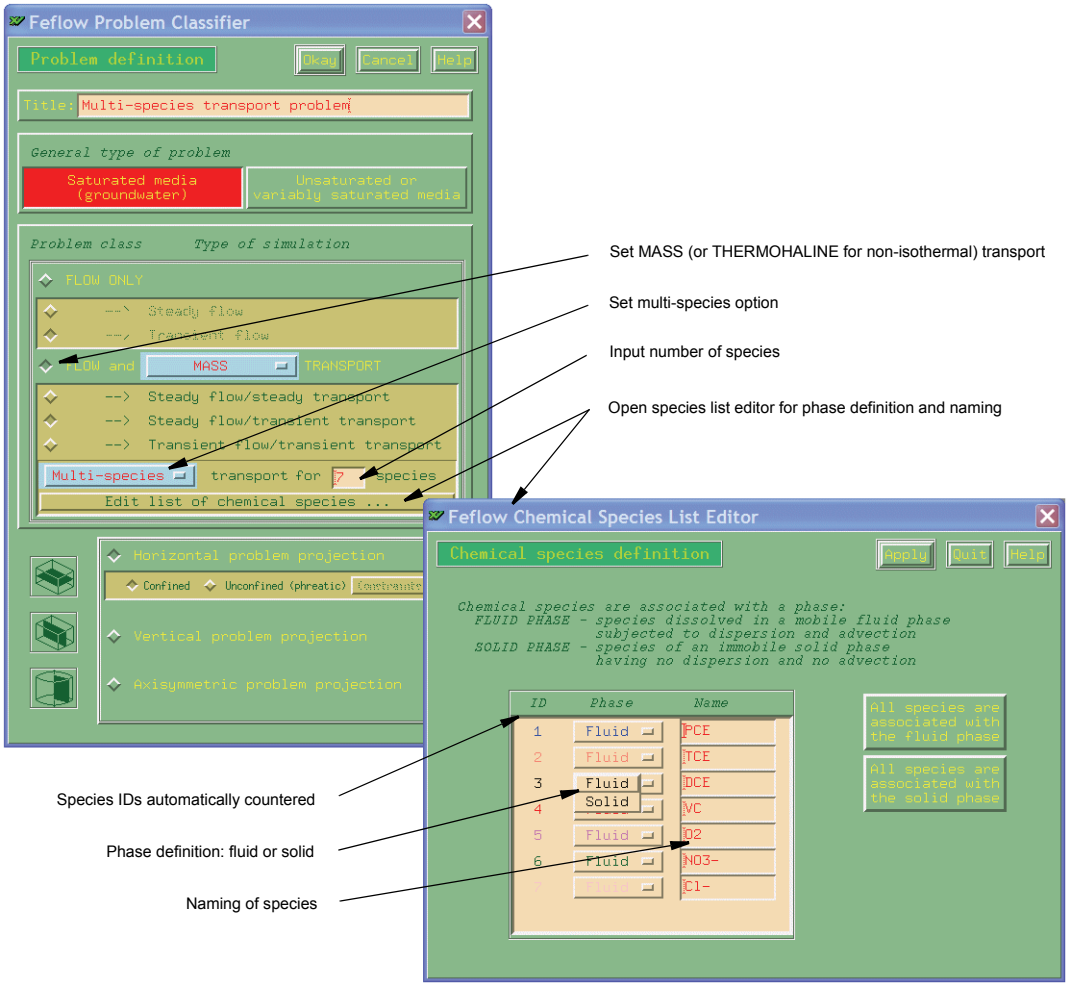

Figure 1.2 FEFLOW's *Problem Classifier* dialog with selected multi-species mass transport, and *Chemical Species List Editor* shown for 7 species.

1.4 Related FEFLOW Dialogs

1.4.1 Multi-species problem class specification

In FEFLOW's *Problem Editor* the *Problem Classifier* dialog allows the introduction of multi-species mass transport as shown in Fig. 1.2. This is possible for the problem classes MASS or THERMOHALINE TRANSPORT, both under saturated or variably saturated conditions. The problem class THERMOHALINE can be used to define a nonisothermal (thermally coupled) multi-species transport problem.

In the dialog the number of species N must be set. This is an arbitrary positive integer (practically, up to a maximum of 10,000 species is possible). The default option ($N = 1$) is single-species transport. Multi-species transport is considered for a number N *greater than unity*. In this case the *Species List Editor* (see Fig. 1.2) can be opened to name the species and to define the phase association. At the same time the species list editor automatically introduces the so-called *species IDs* ($\mathrm{ID} = 1, \ldots, N$), which are used to identify the selected species. (Note that the species ID can be considered as the species indicator $k = 1, \ldots, N$ used in the above theoretical developments). Furthermore, a species concentration $C^{\alpha}_{k=\mathrm{ID}}$ can be associated either with a fluid phase ($\alpha = f$) or with the solid phase ($\alpha = s$), which is related to the governing phase-specific mass transport equations (1-18). In the *mobile* fluid phase f the species are dissolved and subject to dispersion and advection, while species in the *immobile* solid phase s have no dispersion and advection.

1.4.2 Species selector

If multi-species transport is defined a *Species Selector* (Fig. 1.3) appears in proper contexts of data input, evaluation and drawing of data and results. It displays the selected species ID (with the phase association and the name) which applies to all input, evaluation, graphical output and export. The selector is used to switch between the different species IDs.

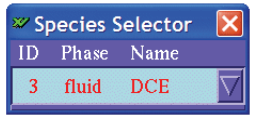

Figure 1.3 FEFLOW's species selector is used to browse through all defined species.

The species selector automatically appears for initial data, boundary data and material data of multi-species mass transport. All input applies to the species ID currently shown by the selector. In the problem editor there are also additional options to copy the problem data for different species IDs (Fig. 1.4).

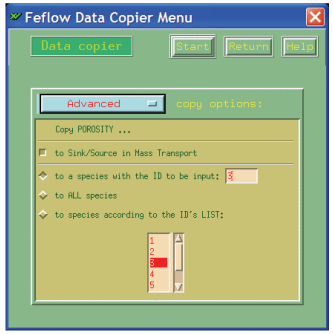

Figure 1.4 Copy of input data for different species.

If the selector is applied a redraw of the underlying data (e.g., boundary conditions, material data, plotted results, diagram curves) is immediately performed.

1.4.3 Multi-species material data

Entering the mass-material menu in FEFLOW's problem editor the material data are related to the selected species ID. If the selected species is associated with a solid phase *s* sorption parameter, molecular diffusion, longitudinal and transverse dispersivities are irrelevant and input is disabled for those parameters. Moreover, for the solid phase the solid volume fraction $\varepsilon_s = 1 - \varepsilon$ is to be entered instead of porosity ε, which must be entered for species associated with the fluid phase *f*, cf. Fig. 1.5.

A new button identified by the Σ symbol launches the *Reaction Kinetics Editor*, where the reaction rates R_k are edited (as thoroughly described in Chapter 1.5). A *Rate* parameter (see Fig. 1.5) appearing in the material menu can be used in the Reaction Kinetics Editor to refer to distributed (or constant) rate coefficients.

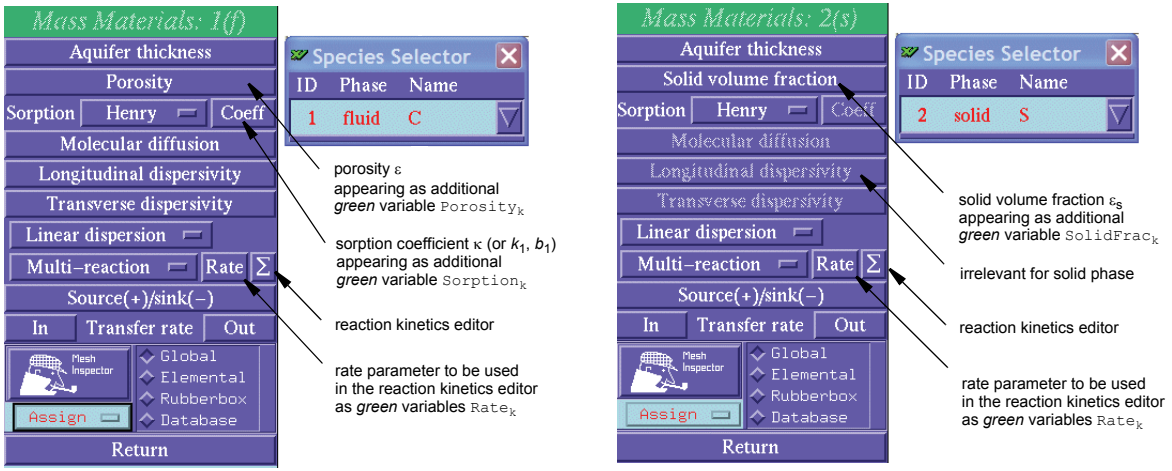

Figure 1.5 Mass-material menus for species of a fluid phase *f* (left) and a solid phase *s* (right).

1.5 Reaction Kinetics Editor

FEFLOW provides a powerful graphical tool for editing the rate expression R_k (1-23). Here, there are two principal classes of reaction expressions that can be applied. First, the kinetics editor includes *precompiled* expressions for which no additional code interpretation is needed. The provided formulae refer to

simplified expressions of the degradation (1-26), Arrhenius (1-28) and Monod (1-31) reaction types for a limited number of reaction terms.

Second (at present available on Windows PC and LINUX platforms), FEFLOW's FEMATHED kinetics editor enables the input of *user-defined* reaction-rate expressions which the user can freely edit in an interactive, graphics-based and flexible manner without any limitations on the algebraic structure of the rate formulae. The user-defined kinetics provides important additional features not available in the precompiled formulae, such as

- freely editable algebraic formulae of arbitrary structure and complexity;
- combination with conditional if-else statements;
- use of porosity (or solid-volume fraction) parameters in the rate expressions;
- use of the saturation variable for unsaturated problems in the rate expressions;
- use of the temperature variable for nonisothermal multi-species transport in the rate expressions.

Rate expressions stemming from user-defined kinetics requires a code *interpreter* at run time. FEFLOW provides such a interpreter with a high computational speed. Practically, when comparing precompiled and user-defined rate expressions for a common number of reaction terms of the formulae, comparable simulation times have been found. Consequently, the user-defined kinetics should be the preferred option providing a maximum of flexibility at a high computational speed.

1.5.1 Precompiled rate expressions

1.5.1.1 Degradation type kinetics

Pushing the Σ button in the material editor (Fig. 1.5) opens the Reaction Kinetics Editor with the default option of a degradation-type kinetics as illustrated in Fig. 1.6.

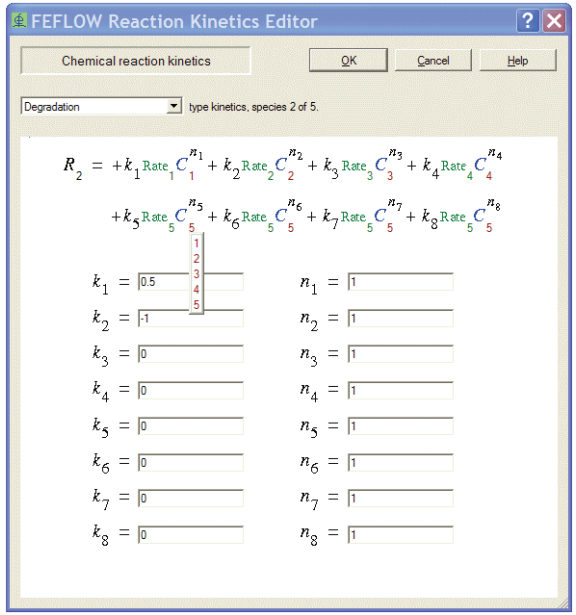

Figure 1.6 FEFLOW's Reaction Kinetics Editor for precompiled rate expression of degradation-type kinetics.

In mathematical terms it represents a reduced variant of the general rate expression (1-26) in the following form:

$$R_k = \sum_{i=1}^{8} k_i \mathrm{Rate}_m (C_m^{\alpha})^{n_i} \qquad \begin{array}{l} \alpha \in (f, s) \\ k = 1, \ldots, N \\ m \in (1, \ldots, N) \end{array} \qquad (1\text{-}48)$$

where k_i are rate constants, Rate_m are rate coefficients, C_m^{α} are the concentrations of species m associated with phase $\alpha \in (f, s)$, and n_i are exponents of the concentrations, where $n_i \geq 0$ is commonly assumed. The rate expression is related to the selected species ID = k (in the example of Fig. 1.6 the ID is 2 and the rate expression is formulated for R_2). The indicator k is the ID set by the species selector (cf. Fig. 1.3). In the symbolism of the formula five different types appear:

- **green** variables (Rate_1, Rate_2, .., Rate_N): These rate coefficients are related to the mass material distributions prescribed in the material editor (see Fig. 1.5) for each species ID. They can be treated also as spatially variable parameters.
- **blue** variables (C_1, C_2, ..., C_N): These are the internal system variables of concentrations of the related species.
- **black** coefficients and exponents (k_1, k_2, ..., k_N; n_1, n_2, ..., n_N): These are editable variables to assign rate factor and rate signs as well as concentration exponents, respectively. They are input in the dialog.
- **red** indices $m \in (1, \ldots, N)$: They are selectable in the dialog and relate the concentration and accompanying variables to a species ID.

The precompiled degradation formula is prepared for eight terms. Commonly, this is sufficient for a wide class of problems (e.g. typical in sequential decay chain reactions). Reaction terms can be suppressed by specifying zero rate factors in the dialog ($k_i = 0$). If more than eight terms are needed the user-defined reaction kinetics (see Section 1.5.2 below) must be used.

1.5.1.2 Arrhenius type kinetics

In contrast to degradation-type kinetics we classify a reaction as an Arrhenius type if products of different species concentration are to be considered. The precompiled rate expression provides for a maximum of four reaction terms as shown in Fig. 1.7. The meaning of the colored variables and coefficients is identical to that described in Section 1.5.1.1.

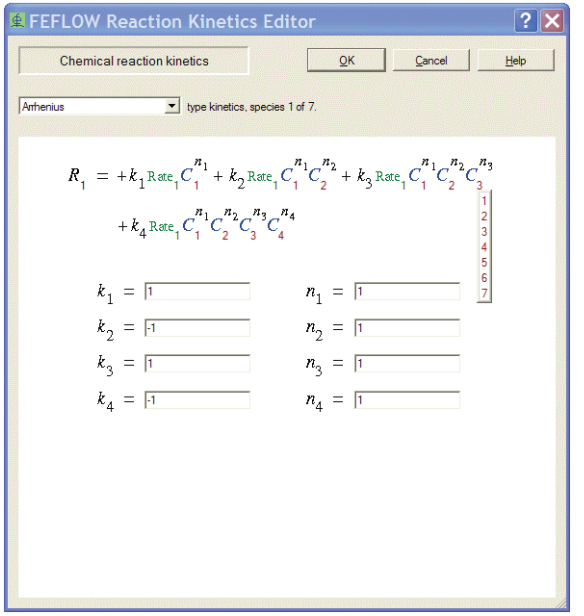

Figure 1.7 FEFLOW's Reaction Kinetics Editor for precompiled rate expression of Arrhenius-type kinetics.

Either in the rate constants k_i or in the rate coefficients Rate_m a factor for porosity (or retardation) must be included, e.g.

$$k_i = \varepsilon \Re_i \bar{k}_i$$

where $\bar{k}_i$ is the intrinsic rate constant. Such type of modification is not necessary if preferring the FEMATHED kinetics editor as discussed in Section 1.5.2 which provides additional variables such as porosity, sorption and others to formulate the reaction rate R_k in a general way.

Note further that precompiled rate expressions are commonly inapplicable for unsaturated conditions because the dependency of R_k on the saturation s_f is not embodied. For unsaturated problems the FEMATHED editor should be used where R_k can also be expressed by the saturation variable.

The same is true for nonisothermal problems. Using FEMATHED the temperature can be incorporated in R_k.

The used Arrhenius reaction type represents a reduced variant of the general form of (1-28) according to:

$$R_k = \sum_{i=1}^{4} k_i \mathrm{Rate}_m (C_m^{\alpha})^{n_1} \prod_{j=2}^{i} (C_m^{\alpha})^{n_j} \qquad \begin{matrix} \alpha \in (f,s) \\ k = 1, \ldots, N \\ m \in (1, \ldots, N) \end{matrix} \quad (1\text{-}49)$$

where k_i are rate constants, Rate_m are rate coefficients, C_m^{α} are the concentrations of species m associated with phase $\alpha \in (f,s)$, and n_j are exponents of the concentrations, where $n_j \geq 0$ is commonly assumed.

1.5.1.3 Monod type kinetics

For the precompiled Monod type kinetics a reduced variant of the general rate law (1-31) has been implemented based on the following expression

$$R_k = \sum_{i=1}^{3} k_i \mathrm{Rate}_m (C_m^{\alpha})^{n_1} \prod_{j=1}^{i} \left(\frac{b_{ij} (C_m^{\alpha})^{n_{j+1}}}{d_{ij} + e_{ij} (C_m^{\alpha})^{n_{j+1}}} \right) \qquad (1\text{-}50)$$

$$\begin{matrix} \alpha \in (f,s) \\ k = 1, \ldots, N \\ m \in (1, \ldots, N) \end{matrix}$$

where $k_i, b_{ij}, d_{ij}, e_{ij}$ are rate constants, Rate_m are rate coefficients, C_m^{α} are the concentrations of species m associated with phase $\alpha \in (f,s)$, and n_j are exponents of the concentrations, where $n_j \geq 0$ is commonly assumed.

This specific Monod reaction formula (1-50) can be edited by the Reaction Kinetics Editor as shown in Fig. 1.8. It consists of three terms for which the colored variables, coefficients and species indicators can be set. If the number of terms is not sufficient or the structure of the provided algebraic formula is unsuitable the user should turn to user-defined reaction kinetics (see Section 1.5.2 below), where more flexibility in the formulation of the Monod type expression is available.

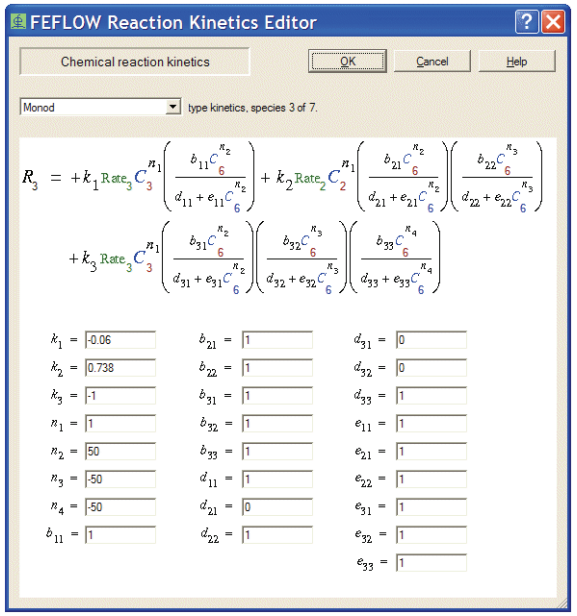

Figure 1.8 FEFLOW's Reaction Kinetics Editor for precompiled rate expression of Monod-type kinetics.

1.5.2 User-defined rate expressions: FEMATHED editor

User-defined type kinetics are accessed via the powerful FEMATHED graphical formula editor that is used to freely design rate expressions and algebraic

relationships for reactions. It can fully replace the precompiled formulae of Section 1.5.1. Moreover, reaction expressions different from the precompiled types and more complex formulae become easy to formulate and apply.

The FEMATHED user-defined kinetics editor appears as the dialog shown in Fig. 1.9. Variables and coefficients are identified by different colors:

- **green** variables ($Rate_1$, $Rate_2$, .., $Rate_N$; $Porosity_1$, $Porosity_2$, ..., $Porosity_N$ or $SolidFrac_1$, $SolidFrac_2$, ..., $SolidFrac_N$; and $Sorption_1$, $Sorption_2$, ..., $Sorption_N$): They represent rate coefficients, values of porosity (or solid fraction for solid phase species), and sorption coefficients (κ for Henry, k_1 for Freundlich, and b_1 for Langmuir adsorption isotherms) that are related to the mass material data input in the material editor (see Fig. 1.5) for each species ID (= k). The green variables can be selected from a list in the editor or by a direct key input. They can be spatially variable.
- **blue** variables (C_1, C_2, ..., C_N and additionally Saturation for unsaturated problems as well as Temperature for thermohaline transport): These are the internal system variables of concentrations of the related species, the saturation and temperature, which can be freely used in the formula design of the rate expression. The blue variables can be selected from a list in the toolbar of the editor (Fig. 1.9).
- Other coefficients, constants and exponents can be arbitrarily introduced in the formulae by using the editor. Once completely defined they appear in **black** color in the formula expression, otherwise variables, coefficients or constants appear in **red** if syntactically erroneous or incompletely assigned.

The major elements of FEMATHED are illustrated in Fig. 1.9. The editor supports standard word-processing shortcuts and key accelerations such as *Control-C* for copy, *Control-X* for cut or *Control-V* for paste of expression parts or characters. All input may be entered by keyboard. For instance, the concentration variable C_3 for species 3 can be selected from the list of blue variables available on the toolbar. Alternatively, entering the key sequence C *Down* 3 automatically retrieves and sets the variable. Any number of auxiliary variables and parentheses can be used to modify the formula. Moreover, *if-else* statements can be introduced in the formula (cf. Fig. 1.9). Arithmetic and logical operations can be used and combined in a practically arbitrary manner. The edited rate formulae for the species are automatically stored in the fem-dataset of the problem. A separate file-access interface exists directly in the FEMATHED editor to save and load the formula expression in XML format. This can be useful to exchange formulae for different species equations or to save variants of rate expressions in a separate database.

An additional feature of FEMATHED is the testing of formulae by activating the built-in code interpreter. Pressing the right mouse button invokes a context menu that includes the option *Tools for experienced users*. Using this option the edited formula can be tested by entering numerical values for the blue and green variables and activating the interpreter (see Fig. 1.10). Note that this option is intended for testing the built-in interpreter outside a simulation run. During the problem simulation the blue and green variables are internally generated when solving the species mass

transport equations and remain hidden from the user.

During the start-up phase of a simulation with user-defined reaction expressions the built-in code interpreter performs a number of checks with regard to the symbolical correctness and completeness of the edited rate formulae. If any check fails the simulation is rejected, the user is alerted and FEMATHED must be used to remove the error or conflict in the formulae.

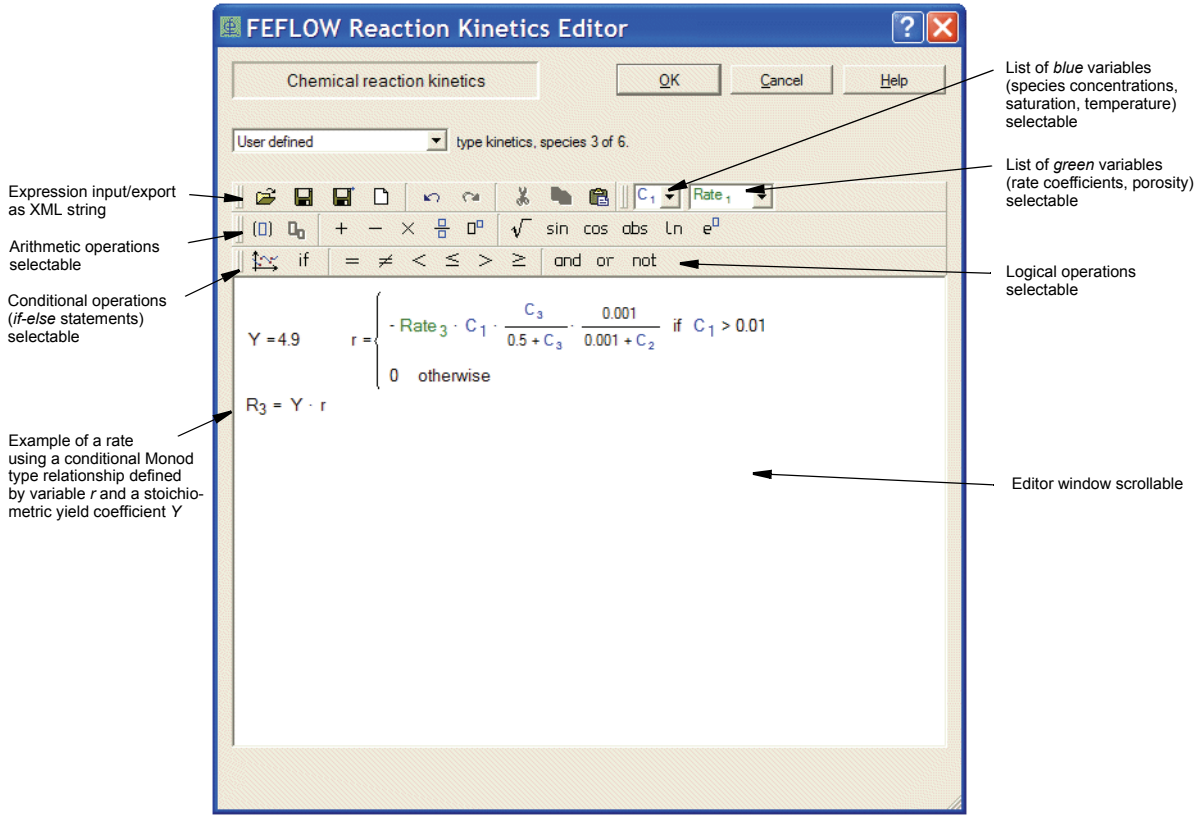

Figure 1.9 FEFLOW's Reaction Kinetics Editor FEMATHED with user-defined kinetics.

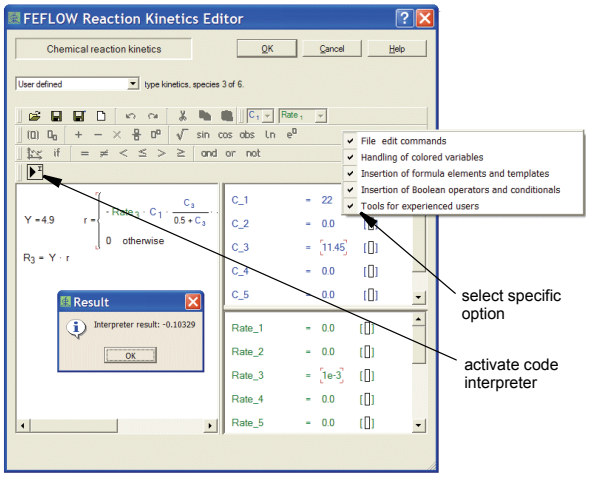

Figure 1.10 FEMATHED editor with testing the built-in code interpreter.

1.6 Mass Material Data of Multi-Species Transport

The following tables relate the mass material data available in FEFLOW in the context of multi-species transport conditions to the theoretical framework developed above. The species *k* corresponds to the ID shown by the species selector. The material data differ depending on the phase association of the selected species *k*.

Table 1.1 Material conditions for 3D, vertical or axisymmetric mass transport of species *k* at fluid phase *f*

Item	Symbol	Unit	Default	Equations
Porosity	ε	1	0.3	1-9, 1-18
Henry sorption:				
Sorption coefficient	κ	1	0	1-17
Freundlich sorption:				
Sorption coefficient	b_1	$(mg/l)^{1-b_2}$	0	1-17
Sorption exponent	b_2	1	0	1-17
Langmuir sorption:				

Table 1.1 Material conditions for 3D, vertical or axisymmetric mass transport of species *k* at fluid phase *f* (continued)

Item	Symbol	Unit	Default	Equations
Sorption coefficient (numerator)	k_1	1	0	1-17
Sorption coefficient (denominator)	k_2	l/mg	0	1-17
Molecular diffusion	D_{d_k}	$10^{-9} m^2 s^{-1}$	1	1-19
Longitudinal dispersivity	β_L	m	5	1-19
Transverse dispersivity	β_T	m	0.5	1-19
Rate	Rate_k	$10^{-4} s^{-1}$	0	1-48, 1-49, 1-50
Σ *(Reaction kinetics editor)*	R_k	$gm^{-3} d^{-1}$	0	1-23, 1-48, 1-49, 1-50 and others
Source(+)/sink(-)	$\overline{Q}_k$	$gm^{-3} d^{-1}$	0	1-15, 1-18
In-transfer rate	$\Phi_{C_k}^{in}$	md^{-1}	0	see FEFLOW Reference Manual[5]
Out-transfer rate	$\Phi_{C_k}^{out}$	md^{-1}	0	see FEFLOW Reference Manual[5]

Table 1.2 Material conditions for 2D horizontal mass transport of species *k* at fluid phase *f*

Item	Symbol	Unit	Default	Equations
Aquifer thickness (only relevant confined conditions)	B	m	1.0	1-22
Porosity	ε	1	0.3	1-9, 1-18
Henry sorption:				
Sorption coefficient	κ	1	0	1-17
Freundlich sorption:				

Table 1.2 Material conditions for 2D horizontal mass transport of species *k* at fluid phase *f* (continued)

Item	Symbol	Unit	Default	Equations
Sorption coefficient	b_1	$(mg/l)^{1-b_2}$	0	1-17
Sorption exponent	b_2	1	0	1-17
Langmuir sorption:				
Sorption coefficient (numerator)	k_1	1	0	1-17
Sorption coefficient (denominator)	k_2	l/mg	0	1-17
Molecular diffusion	D_{d_k}	$10^{-9} m^2 s^{-1}$	1	1-19
Longitudinal dispersivity	β_L	m	5	1-19
Transverse dispersivity	β_T	m	0.5	1-19
Rate	Rate_k	$10^{-4} s^{-1}$	0	1-48, 1-49, 1-50
Σ (Reaction kinetics editor)	R_k	$gm^{-3}d^{-1}$	0	1-23, 1-48, 1-49, 1-50 and others
Source(+)/sink(-)	$\widehat{Q}_k$	$gm^{-2}d^{-1}$	0	1-15, 1-18
In-transfer rate	$\overline{\Phi}_C^{in}$	md^{-1} a)	0	see FEFLOW Reference Manual[5]
Out-transfer rate	$\overline{\Phi}_C^{out}$	md^{-1} b)	0	see FEFLOW Reference Manual[5]

a) For confined conditions and for unconfined conditions at simultaneous application of integral $\int\otimes$ boundary conditions of 3rd kind the unit for the 'In-transfer rate' is: m^2d^{-1}

b) For confined conditions and for unconfined conditions at simultaneous application of integral $\int\otimes$ boundary conditions of 3rd kind the unit for the 'Out-transfer rate' is: m^2d^{-1}

Table 1.3 Material conditions for 3D, vertical or axisymmetric mass transport of species *k* at solid phase *s*

Item	Symbol	Unit	Default	Equations
Solid volume fraction	ε_s	1	0.3	1-9, 1-18
Rate	Rate_k	$10^{-4}s^{-1}$	0	1-48, 1-49, 1-50
$\sum$ (Reaction kinetics editor)	R_k	$gm^{-3}d^{-1}$	0	1-23, 1-48, 1-49, 1-50 and others
Source(+)/sink(-)	$\overline{Q}_k^s$	$gm^{-3}d^{-1}$	0	1-15, 1-18
In-transfer rate	$\Phi_{C_k}^{in}$	md^{-1}	0	see FEFLOW Reference Manual[5]
Out-transfer rate	$\Phi_{C_k}^{out}$	md^{-1}	0	see FEFLOW Reference Manual[5]

Table 1.4 Material conditions for 2D horizontal mass transport of species *k* at solid phase *s*

Item	Symbol	Unit	Default	Equations
Aquifer thickness (only relevant to confined conditions)	B	m	1.0	1-22
Solid volume fraction	ε_s	1	0.3	1-9, 1-18
Rate	Rate_k	$10^{-4}s^{-1}$	0	1-48, 1-49, 1-50
$\sum$ (Reaction kinetics editor)	R_k	$gm^{-3}d^{-1}$	0	1-23, 1-48, 1-49, 1-50 and others
Source(+)/sink(-)	$\widehat{Q}_k^s$	$gm^{-2}d^{-1}$	0	1-15, 1-18
In-transfer rate	$\overline{\Phi}_C^{in}$	md^{-1} a)	0	see FEFLOW Reference Manual[5]
Out-transfer rate	$\overline{\Phi}_C^{out}$	md^{-1} b)	0	see FEFLOW Reference Manual[5]

a) For confined conditions and for unconfined conditions at simultaneous application of integral $\int\otimes$ boundary conditions of 3rd kind the unit for the 'In-transfer rate' is: $m^2 d^{-1}$
b) For confined conditions and for unconfined conditions at simultaneous application of integral $\int\otimes$ boundary conditions of 3rd kind the unit for the 'Out-transfer rate' is: $m^2 d^{-1}$

1.7 Note to Variable-Density Flow and Multi-Species Transport

1.7.1 Multi-species density relation

The fluid density ρ^f is composed of a number of miscible chemical species k with a partial fluid density ρ_k^f (mass of species k per unit volume of fluid), so that

$$\rho^f = \sum_k \rho_k^f \tag{1-51}$$

holds for the mixture[10], where ρ_k^f stands for all species present in the fluid. Moreover, the fluid density ρ^f can be influenced by the temperature T (e.g., density decreases when temperature increases) and by the fluid pressure p^f (density increases when pressure increases due to compressibility). In a formal manner, ρ^f is to be regarded as a dependent thermodynamic variable for which a constitutive relationship, or *equation of state* (EOS), holds

$$\rho^f = \rho^f(p^f, \rho_k^f, T) \tag{1-52}$$

The partial fluid density ρ_k^f appears here as species-related density, which is nothing more than the mass concentration C_k^f

$$C_k^f \equiv \rho_k^f \tag{1-53}$$

The EOS (1-52) is developed as follows (cf.[1,5,10])

$$d\rho^f = \left.\frac{\partial \rho^f}{\partial p^f}\right|_{C_k^f, T} dp^f + \sum_k \left.\frac{\partial \rho^f}{\partial C_k^f}\right|_{p^f, T} dC_k^f + \left.\frac{\partial \rho^f}{\partial T}\right|_{p^f, C_k^f} dT \tag{1-54}$$

$$= \underbrace{\left(\frac{1}{\rho^f}\frac{\partial \rho^f}{\partial p^f}\right)}_{\gamma} \rho^f dp^f + \sum_k \underbrace{\left(\frac{1}{\rho^f}\frac{\partial \rho^f}{\partial C_k^f}\right)}_{\alpha_k} \rho^f dC_k^f + \underbrace{\left(\frac{1}{\rho^f}\frac{\partial \rho^f}{\partial T}\right)}_{-\beta} \rho^f dT$$

where γ is the fluid *compressibility*, and α_k and β are the volumetric species and thermal *expansion coefficient*, respectively. If we assume that γ, α_k and β are constant, the integration of (1-54) immediately leads to the EOS for the density in the common form[1]

$$\rho^f = \rho_0^f e^{\gamma(p^f - p_0^f) + \sum_k \alpha_k (C_k^f - C_{k0}^f) - \beta(T - T_0)} \tag{1-55}$$

where suitable reference values appear for the density $\rho_0^f = \rho^f_{p_0^f, C_{k0}^f, T_0}$ at reference pressure p_0^f, reference concentration C_{k0}^f and reference temperature T_0.

The EOS for the fluid density (1-55) is often linearly approximated by

$$\rho^f = \rho_0^f \left[1 + \gamma(p^f - p_0^f) + \sum_k \alpha_k (C_k^f - C_{k0}^f) - \beta(T - T_0) \right] \quad (1\text{-}56)$$

where γ, α_k and β are considered constant[1,10].

1.7.2 Option settings

To handle variable-density problems for multi-species transport FEFLOW differs two principal options:

- Multiple species-dependent density ratio
- Constant solutal density ratio (default)

which will be explained further below. These options can be set in the *Specific option settings* dialog as shown in Fig. 1.11.

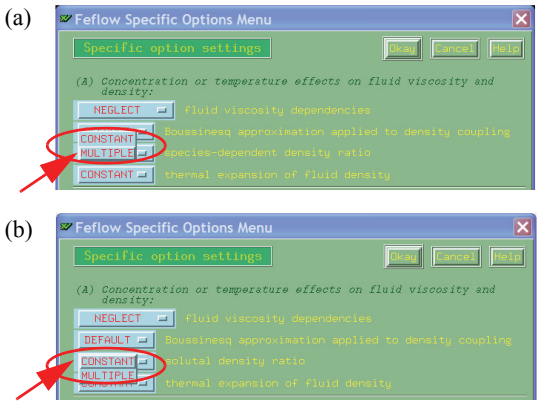

Figure 1.11 Setting of (a) multiple and (b) constant density ratio.

1.7.3 Multiple species-dependent density ratio

In FEFLOW, the dimensionless *fluid density difference ratio*[5] $\bar{\alpha}$ is used, which is defined for a multi-species problem as

$$\bar{\alpha}_k = \alpha_k (C_{ks}^f - C_{k0}^f) \quad (1\text{-}57)$$

where C_{ks}^f is the maximum concentration and C_{k0}^f is the reference concentration of species k. The species-related maximum and reference concentrations are to be input in the specific reference dialog as seen in Fig. 1.12. This has to be done for each species k.

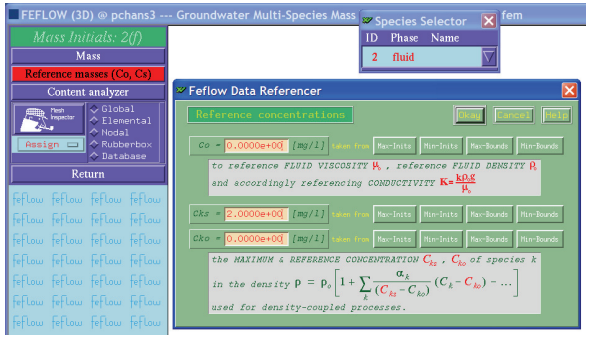

Figure 1.12 Input of maximum and reference concentration for selected species k.

With the multiple species-dependent density ratio $\bar{\alpha}_k$ the following relationship for the fluid density expansion in multi-species applications results and is implemented in FEFLOW, *viz.*,

$$\rho^f = \rho_0^f \left[1 + \bar{\gamma}(h^f - h_0^f) + \sum_k \frac{\bar{\alpha}_k}{(C_{ks}^f - C_{k0}^f)} (C_k^f - C_{k0}^f) - \beta(T - T_0) \right] \quad (1\text{-}58)$$

Note that the hydraulic head h is used in (1-58) for which a specific fluid compressibility $\bar{\gamma} = \gamma \rho_0^f g$ is given (g = gravitational acceleration).

If the multiple density ratio option is set the required multiple density ratio $\bar{\alpha}_k$ has to be input for each species k in the flow material menu. The species selector appears and the multiple density ratio $\bar{\alpha}_k$ is related to the selected species as shown in Fig. 1.13.

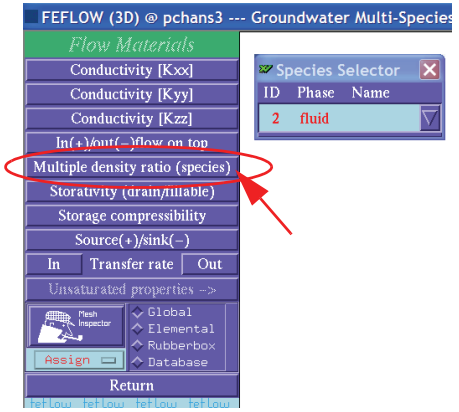

Figure 1.13 Input of multiple density ratio $\bar{\alpha}_k$ for selected species k.

1.7.4 Constant solutal density ratio

Frequently, it can be assumed that the expansion of the fluid density with respect to a concentration increase is the same for all species k, so that

$$\bar{\alpha} \approx \bar{\alpha}_k = \bar{\alpha}_1 = \bar{\alpha}_2 = \ldots = \bar{\alpha}_N \quad (k = 1, \ldots, N) \quad (1\text{-}59)$$

where $\bar{\alpha}$ represents an overall *constant solutal density ratio*. In FEFLOW, the constant $\bar{\alpha}$ is defined as[5]

$$\begin{aligned} \bar{\alpha} &= \alpha(C_s^f - C_o^f) \\ \bar{\alpha} &= [\rho^f(C_s^f) - \rho_0^f] / \rho_0^f \end{aligned} \quad (1\text{-}60)$$

with

$$\rho^f(C_s^f) \approx \rho_0^f + \omega C_s^f \quad (1\text{-}61)$$

where ω is a constant density factor, often approximated by a value of 0.7 for water, and C_s^f is the overall maximum concentration given by

$$C_s^f = \sum_k C_k^{\max} \quad (1\text{-}62)$$

where $C_k^{\max}$ is the maximum concentration of species k. In (1-60), C_o^f represents an overall reference concentration that corresponds to the reference density ρ_0^f. It may be determined by

$$C_o^f = \min_k (C_k^f) \quad (1\text{-}63)$$

Using (1-60) and (1-59) in (1-58), the following modified relationship for the fluid density expansion results and is applied in FEFLOW for the constant density ratio option

$$\rho^f = \rho_0^f \left[1 + \bar{\gamma}(h^f - h_0^f) + \frac{\bar{\alpha}}{(C_s^f - C_o^f)} \sum_k (C_k^f - C_0^f) - \beta(T - T_0) \right] \quad (1\text{-}64)$$

where $\bar{\alpha}$, C_s^f, C_0^f, $\bar{\gamma}$, β, T_0 represent input parameters to be set in the material data menu and the reference data dialog.

1.7.5 Viscosity relations for multi-species transport problems

Generally, in multi-species transport problems the constitutive relationship for the dynamic viscosity of fluid μ^f is developed as a function of the species concentration C_k^f and the temperature T, *viz.*,

$$\mu^f = \mu^f(C_k^f, T) \quad (1\text{-}65)$$

FEFLOW provides in the *Specific option settings* dialog two options to specify the empirical relationship for μ^f in dependence on the variables C_k^f and T:

- Standard
- User-defined

as exhibited in Fig. 1.14.

In the *standard* case (Fig. 1.14a) μ^f is developed as a function of the overall fluid concentration C^f and the temperature T according to

$$\mu^f = \mu^f(C^f, T) \quad (1\text{-}66)$$

where the overall fluid concentration C^f is defined as

$$C^f = \sum_k C_k^f \quad (1\text{-}67)$$

with summation over all dissolved species k in the fluid phase. The empirical relationship (1-66) is given in detail in FEFLOW's *Reference manual*[5] (cf. Fig. 1.14a)

(a)

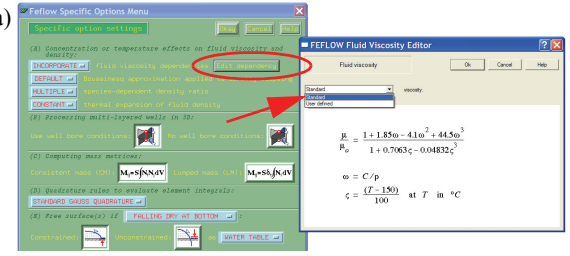

(b)

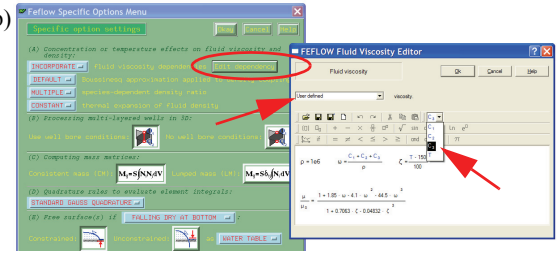

Figure 1.14 Setting of (a) standard and (b) user-defined viscosity relationship.

Alternatively, in the case of a *user-defined* fluid viscosity the FEMATHED viscosity editor is available (see Fig. 1.14b) to specify arbitrary formulae for μ^f of (1-65) in dependence on each species concentrations C_k^f and temperature T without restrictions. For exam-

ple, the fluid viscosity should be developed for two species according to

$$\mu^f = \mu_0^f + \sum_k \frac{\partial \mu^f}{\partial C_k^f}(C_k^f - C_0^f) \qquad (1\text{-}68)$$

where $\partial\mu^f/\partial C_k^f$ are constant coefficients of viscosity variability for each species, and μ_0^f is the reference fluid viscosity at the reference species concentration C_0^f. With the FEMATHED viscosity editor such a user-defined relation can simply input as displayed in Fig. 1.15.

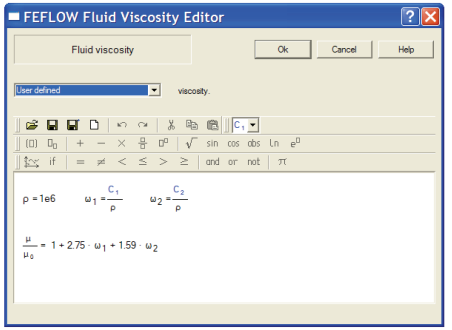

Figure 1.15 Example of a two-species viscosity relationship by using the FEMATHED viscosity editor.

1.8 Examples

1.8.1 Serial-parallel reactions and comparison to the analytical solution by Sun *et al.*

1.8.1.1 Statement of the 1D problem

Sun *et al.*[20] present analytical solutions for one-dimensional (1D) multi-species transport problems with serial and parallel reaction kinetics. As an example, the following reaction network is considered (Fig. 1.16) consisting of five species ($N = 5$). The species B has three daughter species C_1, C_2, C_3.

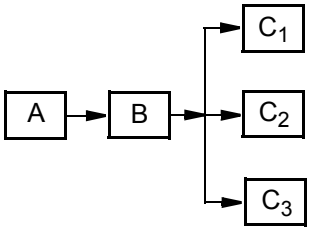

Figure 1.16 Serial-parallel reaction network by Sun *et al.*[2]

The reaction network of Fig. 1.16 can be decomposed into three serial reaction chains: $A \rightarrow B \rightarrow C_1$, $A \rightarrow B \rightarrow C_2$ and $A \rightarrow B \rightarrow C_3$. Accordingly, the following system of transport equations is considered:

$$\left.\begin{aligned}
\frac{\partial C_A}{\partial t} - D\frac{\partial^2 C_A}{\partial x^2} + v\frac{\partial C_A}{\partial x} &= -k_A C_A \\
\frac{\partial C_B}{\partial t} - D\frac{\partial^2 C_B}{\partial x^2} + v\frac{\partial C_B}{\partial x} &= y_B k_A C_A - k_B C_B \\
\frac{\partial C_{C_1}}{\partial t} - D\frac{\partial^2 C_{C_1}}{\partial x^2} + v\frac{\partial C_{C_1}}{\partial x} &= y_{C_1} k_B C_B - k_{C_1} C_{C_1} \\
\frac{\partial C_{C_2}}{\partial t} - D\frac{\partial^2 C_{C_2}}{\partial x^2} + v\frac{\partial C_{C_2}}{\partial x} &= y_{C_2} k_B C_B - k_{C_2} C_{C_2} \\
\frac{\partial C_{C_3}}{\partial t} - D\frac{\partial^2 C_{C_3}}{\partial x^2} + v\frac{\partial C_{C_3}}{\partial x} &= y_{C_3} k_B C_B - k_{C_3} C_{C_3}
\end{aligned}\right\} \qquad (1\text{-}69)$$

The right-hand sides of (1-69) represent the reaction rates $R_A, R_B, R_{C_1}, R_{C_2}, R_{C_3}$. In (1-69) $D = \alpha v$ is a constant dispersion coefficient (α represents dispersivity), x is the one-dimensional coordinate, v is a constant pore velocity, k_k $(k = A, B, C_1, C_2, C_3)$ are first-order rate constants, and y_k are corresponding stoichiometric yields. All species are diluted chemicals in a mobile fluid phase. The transport parameters assumed for this problem are shown in Tab. 1.5. There is no need to specify the porosity ε.

Table 1.5 Problem parameters used

Parameter	Symbol	Value
Length of column, *m*	L	40.0
Dispersivity coefficient, *m*	α	10.0
Pore velocity, md^{-1}	v	0.4
Rate constant of *A*, d^{-1}	k_A	0.2
Rate constant of *B*, d^{-1}	k_B	0.1
Rate constant of C_1, d^{-1}	k_{C_1}	0.02
Rate constant of C_2, d^{-1}	k_{C_2}	0.02
Rate constant of C_3, d^{-1}	k_{C_3}	0.02
Stoichiometric yield of $A \rightarrow B$	y_B	0.5
Stoichiometric yield of $B \rightarrow C_1$	y_{C_1}	0.3
Stoichiometric yield of $B \rightarrow C_2$	y_{C_2}	0.2
Stoichiometric yield of $B \rightarrow C_3$	y_{C_3}	0.1

The following initial and boundary conditions are used:

$$C_k(x, 0) = 0 \qquad (k = A, B, C_1, C_2, C_3) \qquad x \geq 0 \quad \text{(1-70a)}$$

$$\begin{aligned} C_A(0, t) &= 1.0 && && t > 0 \\ C_k(0, t) &= 0 && (k = B, C_1, C_2, C_3) && t > 0 \\ C_k(\infty, t) &= 0 && (k = A, B, C_1, C_2, C_3) && t > 0 \end{aligned} \quad \text{(1-70b)}$$

1.8.1.2 Analytical solution

The equation system (1-69) can be written for species *k*

$$L(C_k) = y_k k_{k-1} C_{k-1} - k_k C_k \quad \text{(1-71)}$$

where $L(.)$ represents the differential operator. Sun *et al.*[20] introduce the auxiliary variable a_k as

$$a_k = C_k + \sum_{j=1}^{k-1} \prod_{i=j}^{k-1} \frac{y_{i+1} k_i}{k_i - k_k} C_j \qquad \forall k = 2, 3, \ldots, N \quad \text{(1-72)}$$

Substituting (1-72) in (1-71) yields the reactive transport equations in terms of a_k, *viz.*,

$$L(a_k) = -k_k a_k \qquad \forall k = 2, 3, \ldots, N \quad \text{(1-73)}$$

Note that for $k = 1$ the transport equation (1-73) in terms of the first auxiliary variable is identical to the original equation (1-71) since $a_k = C_k$. The substituted equations (1-73) can be easily solved by the basic analytical formula

$$a_k(x, t) = \frac{a_{ko}}{2} \exp\left(\frac{vx}{2D}\right) \left[\exp(-\psi_k x) \operatorname{erfc} \frac{x - t\sqrt{v^2 + 4k_k D}}{2\sqrt{Dt}} + \exp(\psi_k x) \operatorname{erfc} \frac{x + t\sqrt{v^2 + 4k_k D}}{2\sqrt{Dt}} \right] \quad \text{(1-74)}$$

where

$$\psi_k = \sqrt{\frac{v^2}{4D^2} + \frac{k_k}{D}}$$
$$\operatorname{erfc}(\xi) = 1 - \operatorname{erf}(\xi) = \frac{2}{\sqrt{\pi}} \int_{\xi}^{\infty} \exp(-\tau^2) d\tau \qquad (1\text{-}75)$$

and a_{ko} is the initial condition in terms of the auxiliary variable and ξ is a dummy variable.

The solutions of all concentrations C_k in the real untransformed domain can be determined by a successive substitution process using (1-72) in a reverse way

$$C_k = a_k - \sum_{j=1}^{k-1} \prod_{i=j}^{k-1} \frac{y_{i+1} k_i}{k_i - k_k} C_j \qquad \forall k = 2, 3, \ldots, N \qquad (1\text{-}76)$$

where a_k is the solution from (1-74).

1.8.1.3 Numerical analysis

Using FEFLOW for the above 5-species transport problem the column is discretized with a spatial increment of $\Delta x = 0.133333$ m. Because the infinite boundary conditions in (1-70b) cannot be applied in a numerical context we extend the column up to 80 m (instead of $L = 40$ m) and use a Neumann-type boundary condition at the outlet boundary section as

$$-D \frac{\partial C_k(2L, t)}{\partial x} = 0 \quad (k = A, B, C_1, C_2, C_3) \quad t > 0 \qquad (1\text{-}77)$$

Accordingly, the double domain is discretized by 600 quadrilateral bi-linear finite elements. The AB/TR predictor-corrector adaptive time-marching scheme is applied, where the RMS error tolerance (1-45) corresponds to $\delta = 10^{-4}$. The initial time step is $\Delta t_o = 10^{-3}$ d.

The reaction kinetics for the present problem is of a degradation type. We employ both the precompiled rate expressions and the user-defined rate formulae by using FEMATHED, where the rates R_k are specified simply as follows:

$$\left.\begin{aligned} R_1 &= -\mathrm{Rate}_1 \cdot C_1 \\ R_2 &= 0.5 \cdot \mathrm{Rate}_1 \cdot C_1 - \mathrm{Rate}_2 \cdot C_2 \\ R_3 &= 0.3 \cdot \mathrm{Rate}_2 \cdot C_2 - \mathrm{Rate}_3 \cdot C_3 \\ R_4 &= 0.2 \cdot \mathrm{Rate}_2 \cdot C_2 - \mathrm{Rate}_4 \cdot C_4 \\ R_5 &= 0.1 \cdot \mathrm{Rate}_2 \cdot C_2 - \mathrm{Rate}_5 \cdot C_5 \end{aligned}\right\} \qquad (1\text{-}78)$$

In (1-78) the parameters Rate_k represent the reaction constants k_k of Tab. 1.5. The used species IDs are linked to the species names and phases as summarized in Tab. 1.6.

1.8.1.4 Results

A comparison of the FEFLOW results with the analytical solutions gives perfect agreements as exhibited in Fig. 1.17. The FEFLOW simulation takes 72 time steps of variable length. Comparing simulation performance between the FEMATHED-interpreted and the precompiled formula options for this problem we found practically the same CPU times. Note that the precompiled degradation formula always executes eight terms (cf. Fig. 1.6) while the FEMATHED code interpreter does not need to consider any extra terms.

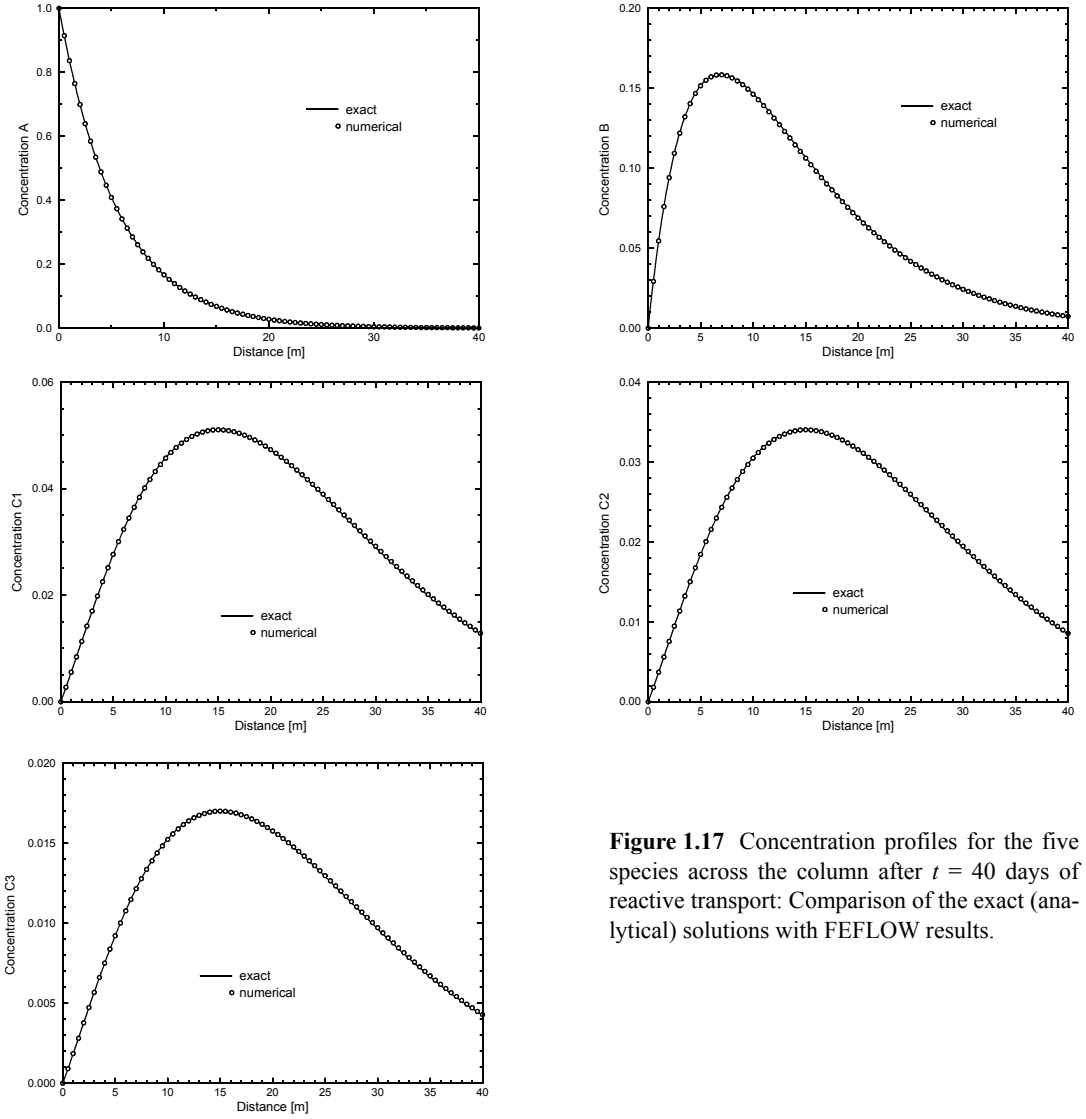

Figure 1.17 Concentration profiles for the five species across the column after t = 40 days of reactive transport: Comparison of the exact (analytical) solutions with FEFLOW results.

Table 1.6 Species IDs for Sun *et al.*'s problem

ID (= k)	Phase	Name
1	fluid	A
2	fluid	B
3	fluid	C_1
4	fluid	C_2
5	fluid	C_3

1.8.1.5 3D multi-species transport with first-order degradation reaction kinetics

Sun *et al.*[21] have extended their analytical approach to 3D problems for homogeneous parameters and steady-state flow regimes. The solutions are demonstrated for a four-species transport in a 3D aquifer of $100\ \text{m} \times 41\ \text{m} \times 25\ \text{m}$. For the finite-element analysis the domain is discretized by 440,000 hexahedral tri-linear elements consisting of 462,825 nodes as shown in Fig. 1.18.

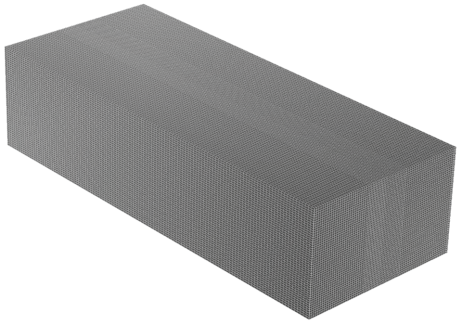

Figure 1.18 Discretized 3D aquifer used in FEFLOW.

First-order reaction rates for the sequential reaction kinetics $C_1 \rightarrow C_2 \rightarrow C_3 \rightarrow C_4$ are given as follows

$$\left.\begin{aligned} R_1 &= -k_1 C_1 \\ R_2 &= k_1 C_1 - k_2 C_2 \\ R_3 &= k_2 C_2 - k_3 C_3 \\ R_4 &= k_3 C_3 - k_4 C_4 \end{aligned}\right\} \qquad (1\text{-}79)$$

where k_k $(k = 1, 2, 3, 4)$ are rate constants, which are listed together with the remaining parameters in Tab. 1.7. All species are considered mobile in the fluid phase; porosity ε does not play a role.

Table 1.7 Problem parameters for the 3D problem

Parameter	Symbol	Value
Length, m	L	100.0
Width, m		41.0
Thickness, m	B	25.0
Longitudinal dispersivity, m	β_L	1.5
Transverse dispersivity, m	β_T	0.3
Pore velocity, md^{-1}	v	0.2
Rate constant of C_1, d^{-1}	k_1	0.05
Rate constant of C_2, d^{-1}	k_2	0.02
Rate constant of C_3, d^{-1}	k_3	0.01
Rate constant of C_4, d^{-1}	k_4	0.005

Boundary and initial conditions are the same as those

used in the 1D example (Section 1.8.1.1). The obtained results are shown in Figs. 1.19 and 1.20. The concentration contours reveal differences between the analytical and numerical solutions. In the finite-element analysis the aquifer is finite and natural Neumann-type boundary conditions (zero concentration gradients) are applied at the outer border faces of the discretized domain. Unlike, in the analytical solution the aquifer domain is considered semi-infinite. Furthermore, Sun *et al.*[21] used an alternative dispersion model, where different transverse dispersivities in the horizontal and vertical directions are applied. In the FEFLOW simulations the isotropic Bear-Scheidegger dispersion model (1-19) is preferred with only one transverse dispersion parameter (Tab. 1.7).

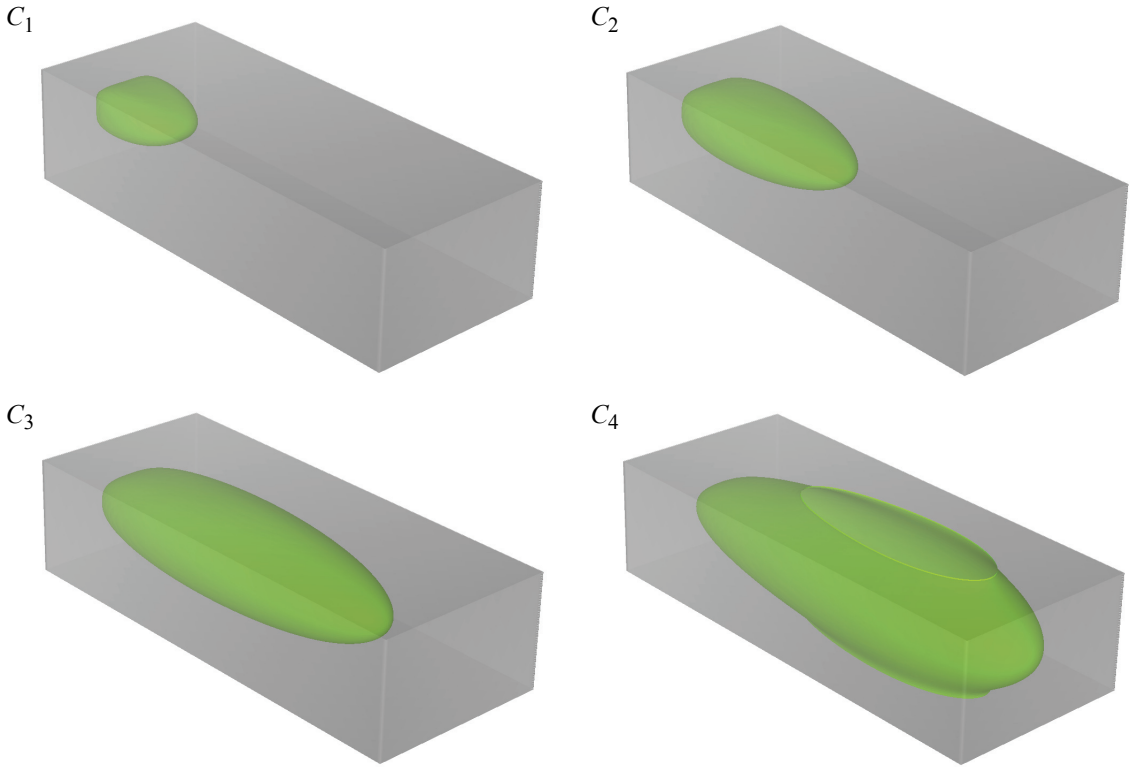

Figure 1.19 FEFLOW results of the three-dimensional 0.01 isosurface concentration for the four species C_1, C_2, C_3 and C_4 after $t = 400$ days**.**

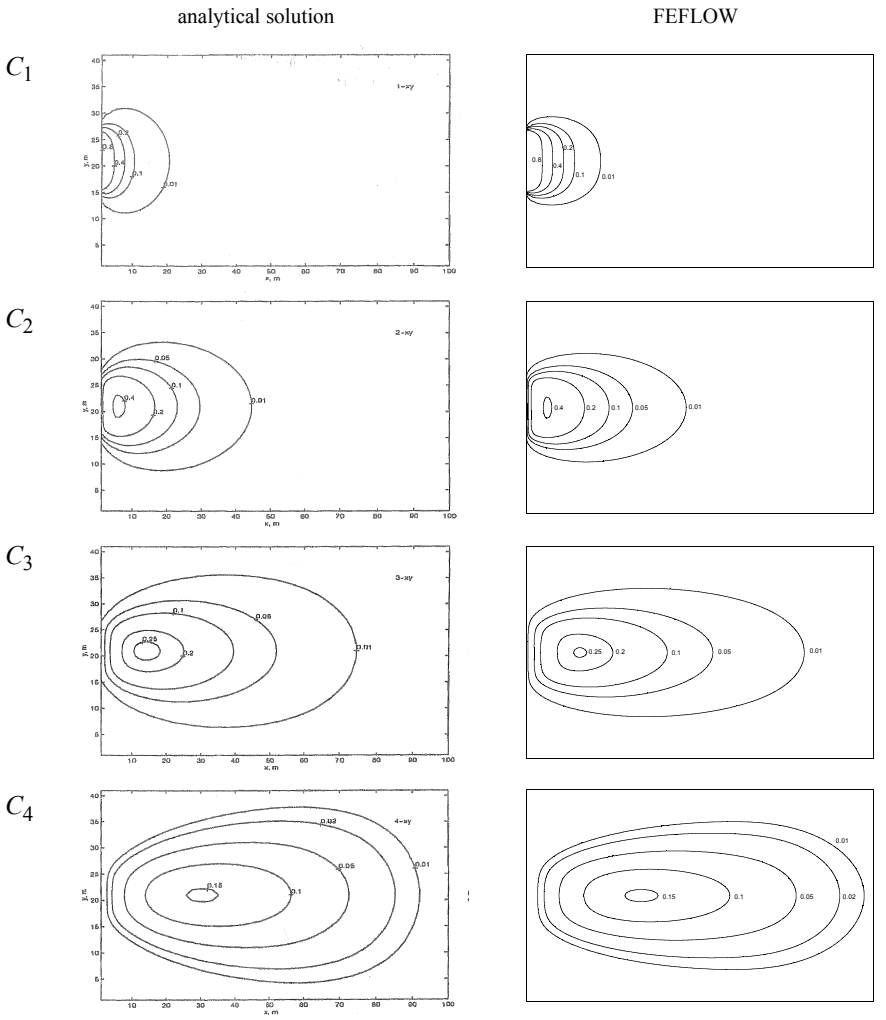

Figure 1.20 Comparison of Sun *et al.*[21]'s analytical solution (left) with FEFLOW results (right): Concentration contours of the four species C_1, C_2, C_3 and C_4 in the *xy*-plane at z = 13 m and t = 400 days**.**

1.8.2 Rate-limited desorption and decay: Comparison to Fry *et al.*'s analytical solution

1.8.2.1 Statement of the 1D problem

Fry *et al.*[11] studied rate-limited desorption and first-order decay on the feasibility of in situ bioremediation of contaminated groundwater by using analytical solutions. The conceptual model is shown in Fig. 1.21.

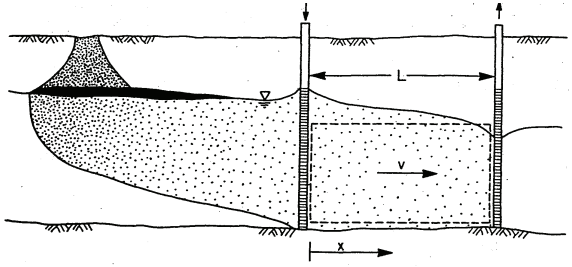

Figure 1.21 Conceptual model of reacting contaminant transport in groundwater by Fry *et al.*[11].

A remedial pump-and-treat scheme is considered assuming conditions of one-dimensional, steady-state groundwater flow through a homogeneous and isotropic aquifer. The modeled portion of the aquifer is bounded by injection and extraction wells (see control volume drawn in Fig. 1.21).

The study concerns a method of restoration of a contaminated aquifer domain, where organic compounds are degraded by indigenous or introduced microorganisms. Degradation of the contaminant is represented by a first-order decay, where the rate of degradation is a function of the contaminant concentration in the aqueous (fluid) phase. Desorption is described using first-order kinetics, where the rate of mass transfer of contaminant from the solid phase to the aqueous phase depends on the concentration gradient between the two phases and a single rate coefficient. The following 1D two-species transport equations are considered (written in the present notation), which is a *one-site kinetic model*[15,25] with linear kinetic sorption and decay in the aqueous phase:

$$\left.\begin{aligned} \varepsilon\frac{\partial C}{\partial t}+\varepsilon_s\frac{\partial S}{\partial t}+q\frac{\partial C}{\partial x}-D\frac{\partial^2 C}{\partial x^2} &= -\varepsilon\vartheta C \\ \varepsilon_s\frac{\partial S}{\partial t} &= \varepsilon_s\alpha(\rho^s K_d C-S) \end{aligned}\right\} \quad (1\text{-}80)$$

or

$$\left.\begin{aligned} \varepsilon\frac{\partial C}{\partial t}+q\frac{\partial C}{\partial x}-D\frac{\partial^2 C}{\partial x^2} &= R_c \\ \varepsilon_s\frac{\partial S}{\partial t} &= R_s \end{aligned}\right\} \quad (1\text{-}81a)$$

with

$$\left.\begin{aligned} R_c &= -(\varepsilon\vartheta+\varepsilon_s\rho^s\alpha K_d)C+\varepsilon_s\alpha S \\ R_s &= \varepsilon_s\alpha(\rho^s K_d C-S) \end{aligned}\right\} \quad (1\text{-}81b)$$

where

C = aqueous concentration (at fluid phase);
S = sorbed concentration (at solid phase);
D = $\beta_L q$, hydrodynamic dispersion coefficient;
q = εv, Darcy velocity;
v = pore velocity;

t = time;
x = distance;
ε = porosity;
ε_s = $(1-\varepsilon)$, solid volume fraction;
ρ^s = solid density;
K_d = equilibrium distribution coefficient;
α = first-order desorption rate constant;
β_L = longitudinal dispersivity;
ϑ = first-order decay rate constant;

The aquifer is initially contaminated and concentrations C and S are uniform throughout the control volume. Furthermore, the sorbed and aqueous phases are initially in linear equilibrium as described with the distribution coefficient K_d. These initial conditions are stated as

$$\left.\begin{aligned} C(x,0) &= C_o \qquad 0 \le x \le L \\ S(x,0) &= S_o \qquad 0 \le x \le L \\ S_o &= \rho^s K_d C_o \end{aligned}\right\} \tag{1-82}$$

where C_o is the aqueous concentration at $t = 0$, S_o is the sorbed concentration at $t = 0$, and L is the length of the control volume (Fig. 1.21).

At the control-volume inlet $(x = 0)$ the contaminant flux due to advection and dispersion is zero for all times. At the control-volume exit $(x = L)$ the concentrations are uniform with distance. Accordingly, the following boundary conditions hold:

$$\left.\begin{aligned} -D\frac{\partial C}{\partial x}(0,t) + qC(0,t) &= 0 \qquad t > 0 \\ \frac{\partial C}{\partial x}(L,t) &= 0 \qquad t > 0 \end{aligned}\right\} \tag{1-83}$$

A test case is considered for which the used parameters are listed in Tab. 1.8.

Table 1.8 Problem parameters used

Parameter	Symbol	Value
Length of domain, *m*	L	10.0
Longitudinal dispersivity, *m*	β_L	1.0
Darcy velocity, md^{-1}	q	0.04
Equilibrium distribution coefficient, cm^3g^{-1}	K_d	0.68
Solid density, $g\ cm^{-3}$	ρ^s	2.67
Porosity	ε	0.4
Solid volume fraction	ε_s	0.6
Desorption rate constant, d^{-1}	α	0.01
Decay rate constant, d^{-1}	ϑ	0.1

1.8.2.2 Numerical analysis

Fry *et al.*'s two-species bioremediation problem as stated above is simulated by FEFLOW. The 1D domain of length $L = 10$ m is discretized by 300 quadrilateral bi-linear finite elements, i.e., the spatial increment is $\Delta x = 0.03333$ m. The AB/TR predictor-corrector adaptive time marching scheme is applied, where the maximum error tolerance (1-46) corresponds to $\delta = 10^{-4}$. The initial time step is $\Delta t_o = 10^{-5}$ d. Additionally, a maximum time step length of 0.5 d and a rate for changing the time-step size Ξ of 2 have proven useful

for the present problem simulation. Due to the boundary conditions (1-83) the *divergence form*[7] of the governing transport equations has to be used, which allows the input of the total (advective plus dispersive) mass flux at a boundary.

The reaction kinetics for the present problem is of a degradation type. We prefer the FEMATHED input for the rates (1-81b), which are specified as follows (note that species ID 1 represents the aqueous species with concentration $C \equiv C_1$ and species ID 2 represents the sorbed species with concentration $S \equiv C_2$):

$$R_1 = -(\text{Porosity}_1 \cdot \text{Rate}_1 + \text{Rate}_2 \cdot Rb \cdot Kd) \cdot C_1 + \text{Rate}_2 \cdot \text{SolidFrac}_2 \cdot C_2 \qquad \text{(1-84a)}$$
$$Rb = \text{SolidFrac}_2 \cdot 2.67 \qquad Kd = 0.68$$

$$R_2 = \text{SolidFrac}_2 \cdot \text{Rate}_2 \cdot (Rs \cdot Kd \cdot C_1 - C_2) \qquad \text{(1-84b)}$$
$$Rs = 2.67 \qquad Kd = 0.68$$

The parameters in (1-84a) and (1-84b) are related to the notation used in (1-81b) as follows: $R_1 \equiv R_c$, $R_2 \equiv R_s$, $\text{Porosity}_1 \equiv \varepsilon$, $\text{Rate}_1 \equiv \vartheta$, $\text{Rate}_2 \equiv \alpha$, $Rs \equiv \rho^s$, $Rb \equiv \varepsilon_s \rho^s$, $Kd \equiv K_d$, and $\text{SolidFrac}_2 \equiv \varepsilon_s$. The species IDs are linked to the species names and phases as summarized in Tab. 1.9.

Table 1.9 Species IDs for Fry *et al.*'s problem

ID (= k)	Phase	Name
1	fluid	C
2	solid	S

1.8.2.3 Results

The FEFLOW results for the problem are compared with the analytical solutions which are presented by Fry *et al.*[11]. As shown in Fig. 1.22 very good agreement with the analytical results is obtained. The FEFLOW simulation takes 2039 time steps. With respect to the computational performances we also tested the precompiled formulae for the degradation-type rate against the preferred FEMATHED formulation. Again we found the same CPU times in both simulations, illustrating the power of the FEMATHED code interpreter.

1.8.3 Two-site equilibrium/kinetic sorption with degradation: Comparison to STANMOD analytical solutions

1.8.3.1 Problem formulation

The two-site sorption concept presumes that sorption or exchange sites in soils can be classified into two fractions: one fraction (Type-1) on which sorption is assumed to be instantaneous, and another fraction (Type-2) on which sorption is considered to be time-dependent. The resulting two-site kinetic model interacts with a solid phase composed of such different constituents as soil minerals, organic matter and various oxides. Studies in transport of pesticides indicate that the two-site kinetic model may well be suitable[25].

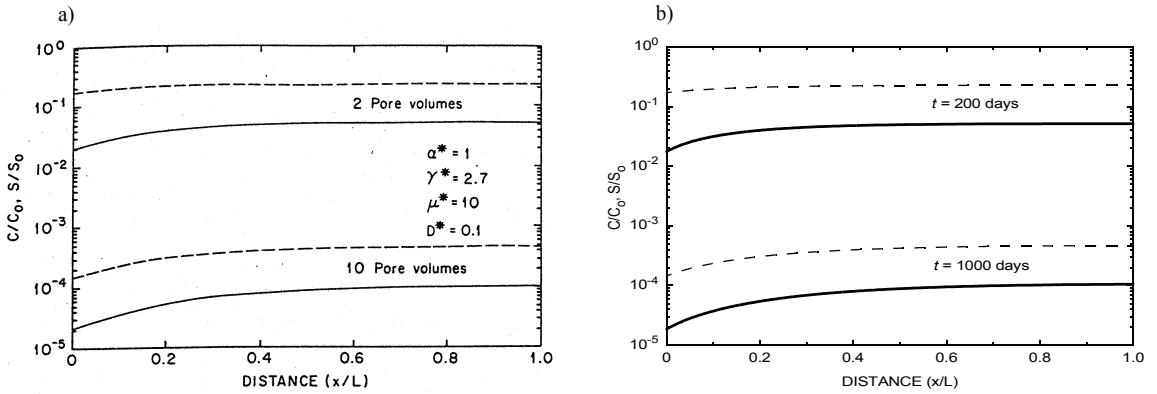

Figure 1.22 Aqueous (C/C_o, solid lines) and sorbed (S/S_o, dashed lines) concentrations versus distance x at times t = 200 days and t = 1000 days: a) Fry *et al.*'s[11] analytical solution (pore volumes = tv/L), b) FEFLOW results.

The derivation proceeds in the same fashion as for the one-site sorption model. We introduce two different sorbed concentrations S_1 and S_2, where the first is for Type-1 at equilibrium sites and the second is for Type-2 at kinetic sites. Because Type-1 sites are always at equilibrium, sorption onto these sites is given by an adsorption function similar to Eq. (1-13), *viz.*,

$$S_1 = f\chi C \tag{1-85}$$

where C is the aqueous concentration at fluid phase, f is the fraction of exchange sites assumed to be at equilibrium and χ is a sorption function. The kinetic part S_2 is subjected to a kinetic relationship in a form

$$S_2 \rightarrow (1-f)\chi C \tag{1-86}$$

By using the equilibrium sorption (1-85) the Type-1 concentration S_1 can be eliminated (expressed by C) from the 3-species basic equations and only 2 species (namely C and S_2) have to be solved. Assuming a linear degradation for all species C, S_1 and S_2, as well as a Henry-type sorption for S_1, we found the following 2-species model equations for a *two-site kinetic sorption*[22,25] with degradation written in the present notation:

$$\left.\begin{aligned} \varepsilon_f \Re_m \frac{\partial C}{\partial t} + \boldsymbol{q}\cdot\nabla C - \nabla\cdot(\boldsymbol{D}\cdot\nabla C) &= R_c \\ \varepsilon_s \frac{\partial S_2}{\partial t} &= R_s \end{aligned}\right\} \tag{1-87a}$$

with

$$\left.\begin{aligned} R_c &= -\left[\alpha\varepsilon_s\frac{(1-f)}{f}\kappa + \varepsilon_s\kappa\mu_{s_1} + \varepsilon_f\mu_f\right]C + \alpha\varepsilon_s S_2 \\ R_s &= \alpha\varepsilon_s\frac{(1-f)}{f}\kappa C - \varepsilon_s(\alpha+\mu_{s_2})S_2 \end{aligned}\right\} \quad (1\text{-}87b)$$

and[8]

$$\left.\begin{aligned} \Re_m &= 1 + \frac{1-\varepsilon}{\varepsilon}\kappa \\ \kappa &= f\,\rho^s K_d \end{aligned}\right\} \quad (1\text{-}87c)$$

where

C = aqueous concentration (at fluid phase f);
S_1 = Type-1 sorbed concentration (at solid phase s);
S_2 = Type-2 sorbed concentration (at solid phase s);
$\boldsymbol{D}$ = hydrodynamic dispersion;
$\boldsymbol{q}$ = $\varepsilon_f\boldsymbol{v}$, Darcy velocity;
$\boldsymbol{v}$ = pore velocity;
t = time;
ε_f = $s_f\varepsilon$, fluid volume fraction;
ε_s = $(1-\varepsilon)$, solid volume fraction;
ε = porosity;
s_f = saturation;
ρ^s = solid density;
K_d = equilibrium distribution coefficient;
f = fraction of exchange sites;
$\Re_m$ = retardation factor;
α = first-order kinetic rate coefficient;
κ = $f\,\rho^s K_d$, Henry adsorption coefficient;
μ_{s_1} = decay coefficient of sorbed species S_1;
μ_{s_2} = decay coefficient of sorbed species S_2;
μ_f = decay coefficient of diluted species C;

Note that the two-site adsorption model (1-87b) reduces to the one-site fully kinetic adsorption model comparable to (1-81b) if $f \to 0$, where the $(1-f)\kappa/f$ terms in (1-87b) have to be replaced by $(1-f)\rho^s K_d$.

1.8.3.2 Statement of a 1D test case

We solve the above two-site kinetic sorption equations for a 1D domain (column) of length L, for which analytical solutions are available[18,22,25]. To compare to analytical solutions the following dimensionless parameters are to be defined:

$$\begin{aligned} \beta &= \frac{\Re_m}{\Re} \qquad \Re = 1 + \left(\frac{1-\varepsilon}{\varepsilon}\right)\frac{\kappa}{f} \\ \omega &= \alpha(1-\beta)\Re\frac{L}{v} \qquad P = \frac{qL}{\|\boldsymbol{D}\|} \end{aligned} \quad (1\text{-}88)$$

where $v = \|\boldsymbol{v}\|$ is the constant 1D pore velocity. With given parameters $\Re$, β and ω the model parameters κ, f and α can be specified as

$$\left.\begin{aligned} \kappa &= \frac{\varepsilon\beta(\Re-1)-(1-\beta)\varepsilon}{1-\varepsilon} \\ f &= \frac{\kappa(1-\varepsilon)}{(\Re-1)\varepsilon} \\ \alpha &= \frac{\omega}{(1-\beta)\Re\frac{v}{L}} \end{aligned}\right\} \quad (1\text{-}89)$$

Note that α is only defined if $\beta < 1$. Equations (1-87a) with (1-87b) are solved for an initially solute-free col-

umn subject to a pulse-type input boundary condition. The initial and boundary conditions are stated as

$$\left.\begin{aligned} C(x,0) &= 0 \qquad 0 \le x \le L \\ S_2(x,0) &= 0 \qquad 0 \le x \le L \end{aligned}\right\} \tag{1-90}$$

and

$$\begin{aligned} -D\frac{\partial C}{\partial x}(0,t) + qC(0,t) &= \begin{cases} qC_o & 0 < t \le t_o \\ 0 & t \ge t_o \end{cases} \\ \frac{\partial C}{\partial x}(L,t) &= 0 \qquad t > 0 \end{aligned} \tag{1-91}$$

where C_o is the input concentration, $D = \|\boldsymbol{D}\| = \beta_L q$ is the dispersion coefficient, $q = \varepsilon_f v = \varepsilon_f \|\boldsymbol{v}\|$ is the Darcy flux and t_o is the time duration of the applied solute pulse.

We consider the 1D column for steady-state flow (q = const) and saturated conditions ($\varepsilon_f = \varepsilon$). Furthermore, we assume that all decay coefficients are the same, i.e., $\mu_f = \mu_{s_1} = \mu_{s_2} = \mu$. Accordingly, a dimensionless decay parameter ψ is defined as

$$\psi = \mu L / v \tag{1-92}$$

The test case is considered for the dimensionless parameters as

$$\left.\begin{aligned} \beta &= 0.5 \\ \Re &= 2.5 \\ \omega &= 0.5 \\ P &= 4.7 \\ \psi &= 0;\ 0.1;\ 0.3;\ 0.6;\ 1.0 \end{aligned}\right\} \tag{1-93}$$

In accordance with (1-93) and in using (1-89) the complete dataset is listed in Tab. 1.10.

Table 1.10 Problem parameters used

Parameter	Symbol	Value
Length of domain, *m*	L	10.0
Pulse duration, *d*	t_o	300
Input concentration, $mg\,l^{-1}$	C_o	1.0
Longitudinal dispersivity, *m*	β_L	2.128
Pore velocity, md^{-1}	v	0.1
Darcy velocity, md^{-1}	q	0.04
Porosity	ε	0.4
Solid volume fraction	ε_s	0.6
Henry coefficient	κ	0.16667
Fraction of exchange site	f	0.16667
Kinetic rate coefficient, d^{-1}	α	0.004
Decay rate coefficients, d^{-1}	μ	0; 0.001; 0.003; 0.006; 0.01

1.8.3.3 Numerical analysis

The two-site equilibrium/kinetic problem as stated above is simulated by FEFLOW. The 1D domain of length L = 10 m is discretized by 300 quadrilateral bilinear finite elements, i.e., the spatial increment is Δx = 0.03333 m. The AB/TR predictor-corrector adaptive time marching scheme is applied, where the RMS error tolerance (1-46) corresponds to $\delta = 10^{-4}$. The

initial time step is $\Delta t_o = 10^{-5}$ d. The final simulation time is 800d. Due to the boundary conditions (1-91) the *divergence form*[7] of the governing transport equations has to be used, which allows the input of the total (advective plus dispersive) mass flux at a boundary.

To model the reaction kinetics we prefer the FEMATHED input for the rates (1-87b), which are specified as follows (note that species ID 1 represents the aqueous species with concentration $C \equiv C_1$ and species ID 2 represents the sorbed species with concentration $S_2 \equiv C_2$):

$$\begin{aligned} R_1 &= -(\mathrm{Rate}_2 \cdot \mathrm{SolidFrac}_2 \cdot g \cdot K \\ &+ \mathrm{SolidFrac}_2 \cdot K \cdot \mathrm{Rate}_1 + \mathrm{Porosity}_1 \cdot \mathrm{Rate}_1) \cdot C_1 \\ &+ \mathrm{Rate}_2 \cdot \mathrm{SolidFrac}_2 \cdot C_2 \\ f &= 0.16667 \quad g = (1-f)/f \quad K = \mathrm{Sorption}_1 \end{aligned} \tag{1-94a}$$

$$\begin{aligned} R_2 &= \mathrm{Rate}_2 \cdot \mathrm{SolidFrac}_2 \cdot g \cdot K \cdot C_1 \\ &- \mathrm{SolidFrac}_2 \cdot (\mathrm{Rate}_2 + \mathrm{Rate}_1) \cdot C_2 \\ f &= 0.16667 \quad g = (1-f)/f \quad K = \mathrm{Sorption}_1 \end{aligned} \tag{1-94b}$$

The parameters in (1-94a) and (1-94b) are related to the notation used in (1-87b) as follows: $R_1 \equiv R_c$, $R_2 \equiv R_s$, $\mathrm{Porosity}_1 \equiv \varepsilon$, $\mathrm{Rate}_1 \equiv \mu$, $\mathrm{Rate}_2 \equiv \alpha$, $\mathrm{Sorption}_1 \equiv \kappa$, and $\mathrm{SolidFrac}_2 \equiv \varepsilon_s$. The species IDs are linked to the species names and phases as summarized in Tab. 1.11.

Table 1.11 Species IDs for two-site sorption problem

ID (= k)	Phase	Name
1	fluid	C
2	solid	S_2

1.8.3.4 Results

The FEFLOW results for the problem are compared with the analytical solutions which are evaluated by using the STANMOD package[18]. We simulate the breakthrough characteristics for C and S_2 measured at the effluent boundary at $x = L$ for different decay parameters ψ. The plots are related to dimensionless aqueous and sorbed concentrations C^* and S_2^*, respectively, defined as

$$\left.\begin{aligned} C^* &= \frac{C}{C_o} \\ S_2^* &= \frac{S_2}{\frac{1-f}{f}\kappa C_o} \end{aligned}\right\} \tag{1-95}$$

Figure 1.23 reveals a good agreement with the analytical solutions.

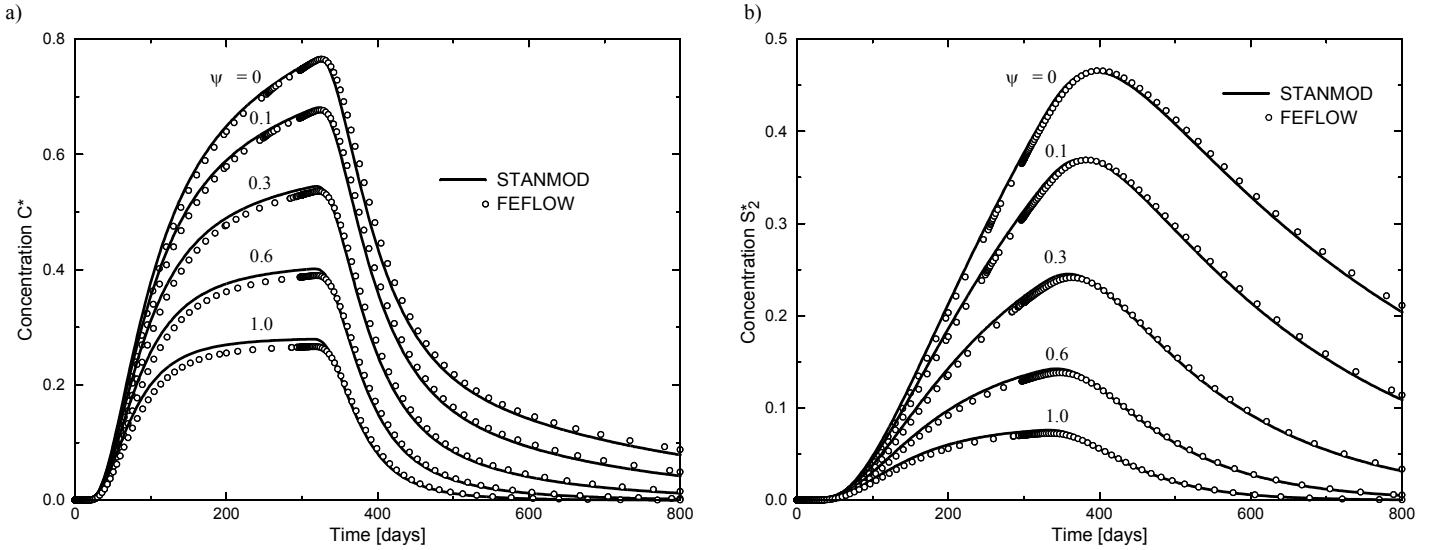

Figure 1.23 FEFLOW results versus STANMOD solutions[18] for effluent breakthrough history of a) aqueous C^* and b) sorbed S_2^* concentrations for different decay parameters ψ at $P = 4.7$, $\beta = 0.5$, $\omega = 0.5$, $\Re = 2.5$ and $t_o = 300$ d.

1.9 Sequential and Non-sequential Chlorinated Solvents Degradation under Variable Aerobic-Anaerobic Conditions

1.9.1 Introduction

In contrast to nonsequential (aerobic) degradation of chlorinated solvents, sequential dehalogenation is performed by anaerobic bacteria that cannot work under aerobic conditions. Both mechanisms can occur in the same contaminant plume depending on oxygen and nitrate concentrations. Monitoring the chloride released during the dehalogenation can be useful to locate the areas where dehalogenation occurs and to estimate degradation rates. This example simulation issues from a benchmark within the MACAOH (Modélisation de l'atténuation des composés organo-chlorés dans les aquifères) project of the French Environment and Energy Management Agency (ADEME) with various university and private partners, namely, BURGEAP, IFARE, IFP, IMFS, and IMFT. The project focuses on chlorinated solvents, specifically PCE (perchloroethylene), TCE (trichloroethylene), DCE (cis- and trans-1,2-dichloroethylene) and VC (vinyl chloride). The aim of the benchmark was to evaluate the state of the art in the numerical simulation of the natu-

ral degradation of chlorinated solvents in aquifers in France. The results of this project will be published in 2006.

1.9.2 Conceptual problem

A mixture of PCE and TCE is injected continuously in an initially uncontaminated 1D domain containing dissolved oxygen, nitrate, and chloride. The initial aerobic conditions do not allow the degradation of PCE by anaerobic bacteria, but a slow complete mineralization of TCE is considered. Daughter products of TCE during the mineralization (H_2O and CO_2) are not simulated, except chloride ions. The oxygen concentration decreases as a consequence of the aerobic bacteria respiration. This behavior continues as long as the concentration of oxygen remains above a critical level. The reactions take place only in the fluid phase. Reaction and sorption with the solid phase are neglected.

Wiedemeier *et al.*[24] explain that anaerobic bacteria cannot work at oxygen concentrations greater than 0.5 mg l^{-1}. When no more oxygen remains in water, aerobic bacteria use nitrate. After Wiedemeier *et al.*[24], anaerobic bacteria can start the sequential reductive dechlorination of chlorinated solvents under nitrate concentrations smaller than 1 mg l^{-1}.

In the MACAOH benchmark, it was assumed that the sequential degradation starts in the presence of nitrate as soon as the oxygen concentration reaches zero. Thus, once oxygen reaches sufficiently low concentration anywhere in the domain, the following reductive sequential degradation of chlorinated solvents starts

$$\mathrm{PCE} \xrightarrow{H^+, 2e^-} \mathrm{TCE} + \mathrm{Cl}^- \xrightarrow{H^+, 2e^-} \mathrm{DCE} + \mathrm{Cl}^- \xrightarrow{H^+, 2e^-} \mathrm{VC} + \mathrm{Cl}^- \tag{1-96}$$

The concentration of nitrate is supposed to decrease independently of other species, as soon as the oxygen concentration reaches zero, following a simple first-order degradation law.

1.9.3 Equations of mass transport with sequential and non-sequential reaction

The one-dimensional equation of transport for the homogeneous reaction of nonretarded parent and daughter species can be written as

$$\begin{aligned} \varepsilon\frac{\partial C_k}{\partial t} - D\frac{\partial^2 C_k}{\partial x^2} + q\frac{\partial C_k}{\partial x} &= \varepsilon(\delta_k k_k^{\mathrm{anae}} C_k - (1-\delta_k) k_k^{\mathrm{ae}} C_k) \\ \varepsilon\frac{\partial C_j}{\partial t} - D\frac{\partial^2 C_j}{\partial x^2} + q\frac{\partial C_j}{\partial x} &= \varepsilon(\delta_j k_j^{\mathrm{anae}} C_j - \delta_i a_{k,j} k_k^{\mathrm{anae}} C_k - (1-\delta_j) k_j^{\mathrm{ae}} C_j) \end{aligned} \tag{1-97}$$

where ε denotes porosity, k the parent species (PCE to DCE), j the daughter product (TCE to VC), C_k and C_j the concentration of species k and j, t the time, q the Darcy velocity, D the mechanical dispersion ($D = \beta_L q$ with β_L as the longitudinal dispersivity), k_k^{ae}, k_j^{ae}, k_k^{anae} and k_j^{anae} the first order decay constants of species k and j under aerobic and anaerobic conditions, respectively, $a_{k,j}$ the stoichiometric yield for the degradation of species k to produce species j, δ_k and δ_j functions equal to 0 for degradation in aerobic conditions and equal to 1 for degradation in anaerobic conditions.

1.9.4 Reaction rates

Chlorinated solvents

The reaction rates appear on the right-hand sides of (1-97). Under aerobic conditions, there is no sequential degradation and the reaction rates $R^{ae}_{PCE,TCE,DCE,VC}$ of chlorinated solvents in aerobic conditions simplify to

$$\left.\begin{aligned} R^{ae}_{PCE} &= 0 \\ R^{ae}_{TCE} &= -\varepsilon(k^{ae}_{TCE} C_{TCE}) \\ R^{ae}_{DCE} &= 0 \\ R^{ae}_{VC} &= 0 \end{aligned}\right\} \qquad (1\text{-}98)$$

Under anaerobic conditions, the sequential degradation from PCE to VC lead to reaction rates $R^{anae}_{PCE,TCE,DCE,VC}$ defined as follows

$$\left.\begin{aligned} R^{anae}_{PCE} &= -\varepsilon(k^{anae}_{PCE} C_{PCE}) \\ R^{anae}_{TCE} &= -\varepsilon(k^{anae}_{TCE} C_{TCE} - a_{PCE,TCE} k^{anae}_{PCE} C_{PCE}) \\ R^{anae}_{DCE} &= -\varepsilon(k^{anae}_{DCE} C_{DCE} - a_{TCE,DCE} k^{anae}_{TCE} C_{TCE}) \\ R^{anae}_{VC} &= -\varepsilon(k^{anae}_{VC} C_{VC} - a_{DCE,VC} k^{anae}_{DCE} C_{DCE}) \end{aligned}\right\} \qquad (1\text{-}99)$$

Except for PCE that has no parent species, all reaction rates are made of an independent degradation term and of a production term dependent on the degradation of the parent species. Note that because FEFLOW can handle simultaneously homogeneous and heterogeneous reactions for the same species, users have to include the porosity 'manually' in the definition of the reaction rates for a homogeneous reaction.

Oxygen

Aerobic bacteria do not use oxygen in definite proportions during their respiration. The oxygen consumption was arbitrarily defined in the benchmark as follows

$$\frac{\partial C_{O_2}}{\partial t} = 4.5\frac{\partial C_{TCE}}{\partial t} + 4\frac{\partial C_{DCE}}{\partial t} + 3.5\frac{\partial C_{VC}}{\partial t} \qquad (1\text{-}100)$$

From the conceptual model, the terms in DCE and VC are superfluous because they are not present in the system at the initial state and because TCE does not degrade into those compounds in aerobic conditions. Thus in this example simulation there cannot be DCE or VC under aerobic conditions and it follows from (1-100) that

$$R^{ae}_{O_2} = 4.5R^{ae}_{TCE} + 4R^{ae}_{DCE} + 3.5R^{ae}_{VC} \qquad (1\text{-}101)$$

By definition there is no oxygen in anaerobic conditions, so

$$R^{anae}_{O_2} = 0 \qquad (1\text{-}102)$$

Chloride

Chloride is released into the groundwater during the dehalogenation of chlorinated solvents. The relation

$$\frac{\partial C_{Cl^-}}{\partial t} = -1.068\frac{\partial C_{TCE}}{\partial t} - 0.712\frac{\partial C_{DCE}}{\partial t} - 0.552\frac{\partial C_{VC}}{\partial t} \qquad (1\text{-}103)$$

is assumed under aerobic conditions, i.e., in terms of reaction rates

$$R^{ae}_{Cl^-} = -1.068R^{ae}_{TCE} - 0.712R^{ae}_{DCE} - 0.552R^{ae}_{VC} \qquad (1\text{-}104)$$

For reductive dechlorination, different dechlorination kinetics is assumed, *viz.*,

$$\frac{\partial C_{Cl^-}}{\partial t} = -0.208\frac{\partial C_{PCE}}{\partial t} - 0.262\frac{\partial C_{TCE}}{\partial t} - 0.356\frac{\partial C_{DCE}}{\partial t} - 0.552\frac{\partial C_{VC}}{\partial t} \quad (1\text{-}105)$$

and

$$R^{anae}_{Cl^-} = -0.208R^{anae}_{PCE} - 0.262R^{anae}_{TCE} - 0.356R^{anae}_{DCE} - 0.552R^{anae}_{VC} \quad (1\text{-}106)$$

Nitrate

Nitrate is supposed to degrade at a given independent rate if the oxygen concentration is zero, which leads to the following reaction rates

$$\begin{aligned} R^{ae}_{NO3^-} &= 0 \\ R^{anae}_{NO3^-} &= -\varepsilon(k^{anae}_{NO3^-} C_{NO3^-}) \end{aligned} \quad (1\text{-}107)$$

1.9.5 Numerical model

One-dimensional steady flow and transient transport are supposed. The species simulated are PCE, TCE, DCE, VC, oxygen, nitrate, and chloride. The aquifer length is 250 m, Darcy velocity of water 0.4 m d^{-1}. For all species, porosity ε is 0.4, longitudinal dispersivity β_L is 1 m, and retardation factor $\Re_k$ is 1. Steady Dirichlet transport boundaries of 3 mg l^{-1} for PCE, 5 mg l^{-1} for TCE, 0 mg l^{-1} for DCE and VC, 10 mg l^{-1} for oxygen, 20 mg l^{-1} for nitrate, and 15 mg l^{-1} for chloride, are applied at $x = 0$. Initial conditions are uniform, are equal to the boundary condition for oxygen, nitrate and chloride, and to zero for all chlorinated solvents. The first order decay rates and stoichiometric coefficients are given in Tab. 1.12.

Table 1.12 First order decay rates and stoichiometric coefficients

Species k	k_k^{anae}	k_k^{ae}	Unit	$a_{k,j}$	Unit
PCE	0.03	0	d^{-1}	aimless	
TCE	0.09	0.009	d^{-1}	$a_{PCE,TCE} = 0.792$	-
DCE	0.009	0.15	d^{-1}	$a_{TCE,DCE} = 0.738$	-
VC	0	0.24	d^{-1}	$a_{DCE,VC} = 0.644$	-
oxygen	0	0	d^{-1}	undefined	
nitrate	0.1	0	d^{-1}	undefined	
chloride	0	0	d^{-1}	undefined	

FEFLOW's FEMATHED Reaction Kinetics Editor allows to easily define complex reaction rates. Particularly useful here is the 'if otherwise' construct to switch between aerobic and anaerobic behavior. It allows the combination of aerobic and anaerobic reaction rates in one composite reaction rate R_k for each species k. The reaction rates are entered in FEFLOW as listed in Tab. 1.13.

Another 'if otherwise' construct is used to stop the consumption of oxygen at an arbitrary residual concentration of 0.05 mg l^{-1}. If the oxygen consumption was not bounded by the user, the oxygen concentration would continue to decrease and would lead to negative

concentrations. In contrast, the degradation of nitrate does not need to be bounded because it is a simple first-order reaction that can only lead to positive concentrations.

Table 1.13 Reaction rates as defined in FEFLOW

Reaction rate R_k	Comment
$R_{PCE} = \begin{cases} -\varepsilon(k_{PCE}^{anae} C_{PCE}) & \text{if} \quad C_{O_2} < 0.1 \\ 0 & \text{otherwise} \end{cases}$	$k_{PCE}^{ae} = 0$
$R_{TCE} = \begin{cases} -\varepsilon(k_{TCE}^{anae} C_{TCE} - a_{PCE,TCE} k_{PCE}^{anae} C_{PCE}) & \text{if} \quad C_{O_2} < 0.1 \\ -\varepsilon\left(\frac{k_{TCE}^{anae}}{10} C_{TCE}\right) & \text{otherwise} \end{cases}$	
$R_{DCE} = \begin{cases} -\varepsilon(k_{DCE}^{anae} C_{DCE} - a_{TCE,DCE} k_{TCE}^{anae} C_{TCE}) & \text{if} \quad C_{O_2} < 0.1 \\ -\varepsilon(k_{DCE}^{anae} \frac{0.150}{0.009}) & \text{otherwise} \end{cases}$	degradation is supposed under aerobic conditions
$R_{VC} = \begin{cases} -\varepsilon(0 - a_{DCE,VC} k_{DCE}^{anae} C_{DCE}) & \text{if} \quad C_{O_2} < 0.1 \\ -\varepsilon(k_{VC}^{ae} C_{VC}) & \text{otherwise} \end{cases}$	no VC decay in anaerobic conditions ($k_{VC}^{anae} = 0$) but decay supposed under aerobic conditions
$R_{O_2} = \begin{cases} \varepsilon\left(-4.5 \frac{k_{TCE}^{anae}}{10} C_{TCE} - 4.0 \frac{0.15}{0.009} k_{DCE}^{anae} C_{DCE} - 3.5 k_{VC}^{ae} C_{VC}\right) & \text{if} \quad C_{O_2} > 0.05 \\ 0 & \text{otherwise} \end{cases}$	
$R_{NO3^-} = \begin{cases} -\varepsilon(k_{NO3^-}^{anae} C_{NO3^-}) & \text{if} \quad C_{O_2} < 0.1 \\ 0 & \text{otherwise} \end{cases}$	decay of nitrate starts under anaerobic conditions
$R_{Cl^-} = \begin{cases} \varepsilon(0.208 k_{PCE}^{anae} C_{PCE} + 0.262 k_{TCE}^{anae} C_{TCE} + 0.356 k_{DCE}^{anae} C_{DCE}) & \text{if} \quad C_{O_2} < 0.1 \\ \varepsilon(1.068 k_{TCE}^{ae} C_{TCE}) & \text{otherwise} \end{cases}$	neither VC nor DCE under aerobic conditions

FEFLOW accepts only one value of first-order decay rate for one species, but in this example, the decay rates differ in aerobic and anaerobic conditions. It is the reason why it is sometimes necessary to correct the value of the rate in the Reaction Kinetics Editor to match the decay rate for the given conditions. The reference

decay rates are here the rates in anaerobic conditions. It means for example for TCE that the decay rate has to be divided by 10 in the kinetics editor for aerobic conditions. VC is the exception. It is necessary to enter the value $k_{VC}^{ae} \neq 0$ instead of $k_{VC}^{anae} = 0$ in the first order decay rate, to make the decay rate of VC available to the definition of the oxygen consumption.

1.9.6 Simulation results

The problem was solved by FEFLOW for steady flow and transient transport for 365 days in a two-dimensional (pseudo one-dimensional) model as shown in Fig. 1.24, with an automatic forward Euler/backward Euler time-integration scheme without upwind. The maximal time-step increase Ξ is 1.1 and the maximal time step Δt^{max} is limited at 0.5 days to be sure that the Courant number does not exceed 0.5. In order to reproduce as closely as possible the simulation conditions of other numerical codes (finite differences), the mesh is built on the basis of linear quadrilateral elements. Models with 250, 500 and 1000 elements were solved.

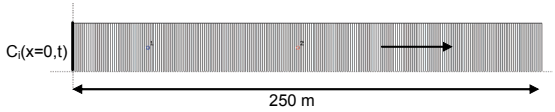

Figure 1.24 Pseudo one-dimensional mesh with 250 linear quadrilateral elements. Vertical exageration 500:1. Identifier 1 and 2 represent observation points.

The computing time for the 250-elements model on a 1.5 GHz Intel Pentium4 processor with 1.25 GByte RAM is about 13 min.

The computation time is a function of the number of species simulated, because the transport problem has to be solved for each species (here $N = 7$ species) at each time step. Figure 1.25 shows the evolution of the time steps during the computation. While the solution proceeds relatively fast at the beginning, the speed of computation decreases drastically once the sequential degradation starts. The sudden decrease in time step length at about 233 days corresponds exactly to the time at which VC reaches the outlet leading to a strong concentration gradient at the outlet for this species.

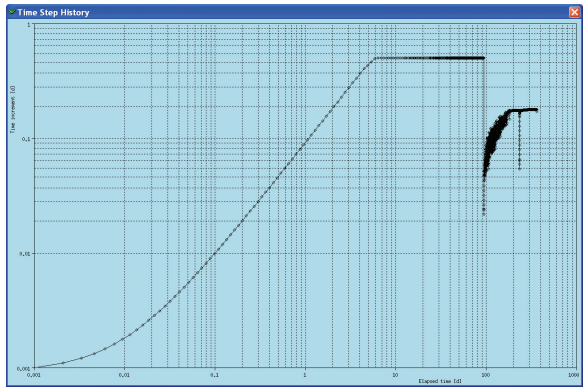

Figure 1.25 Time steps Δt_n as a function of computation time for 250 elements.

The simulation results of the 250-elements model are shown in Figs. 1.26, 1.27, and 1.28.

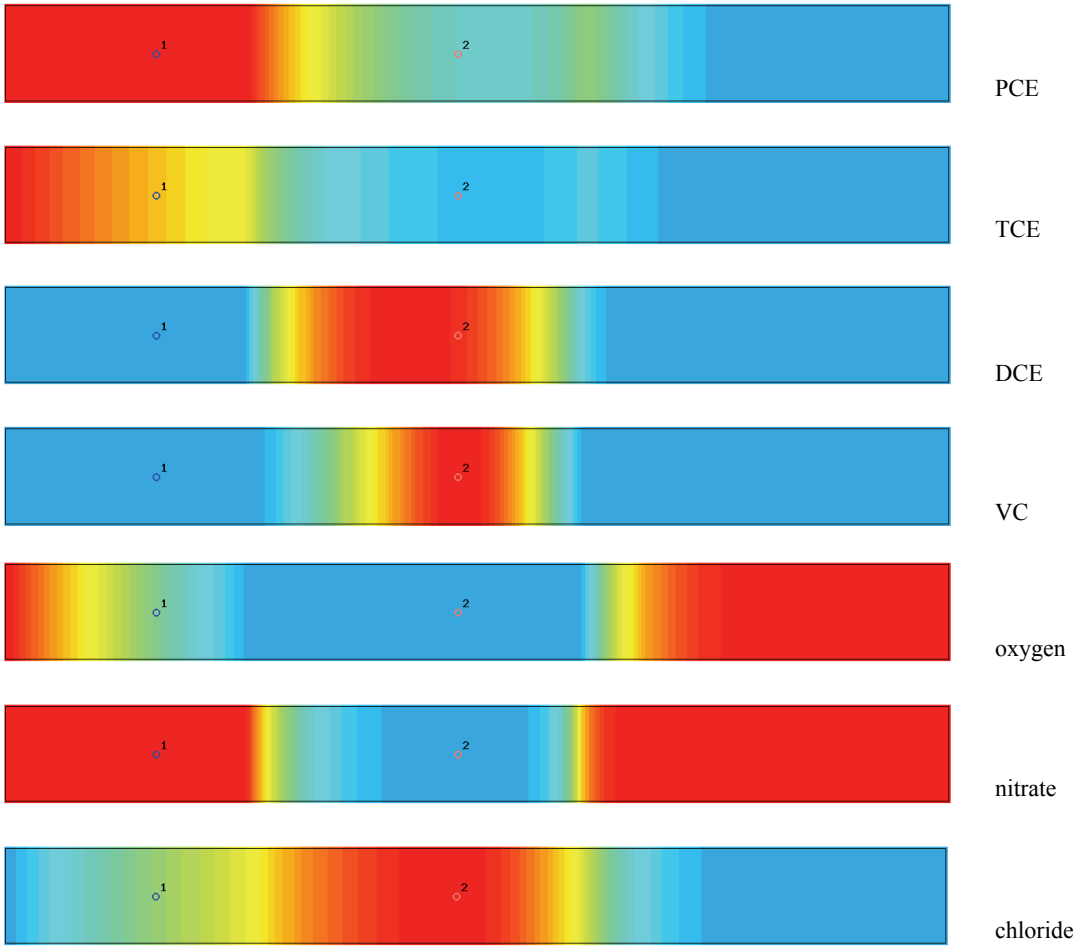

Figure 1.26 Concentration fringes for all species *k* at 150 days. Darcy velocity = 0.4 m d^{-1}, adsorption = 0.

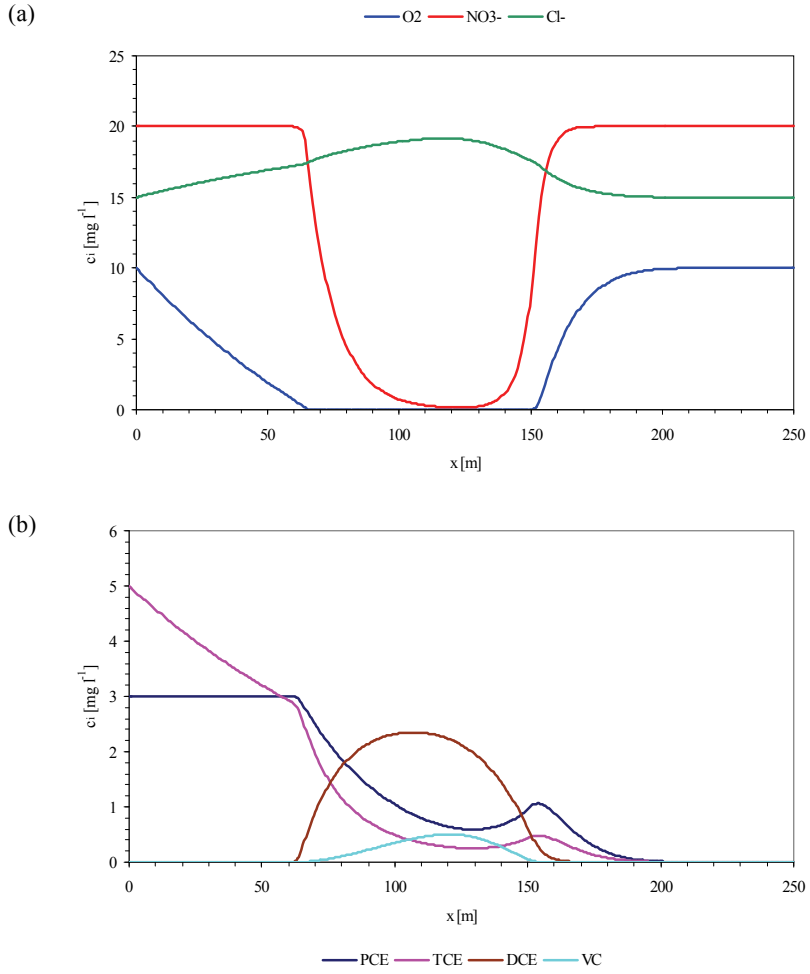

Figure 1.27 Concentration profiles along the *x*-axis at 150 days, for (a) oxygen, nitrate, chloride, and (b) chlorinated solvents. Darcy velocity = 0.4 m d^{-1}, adsorption = 0.

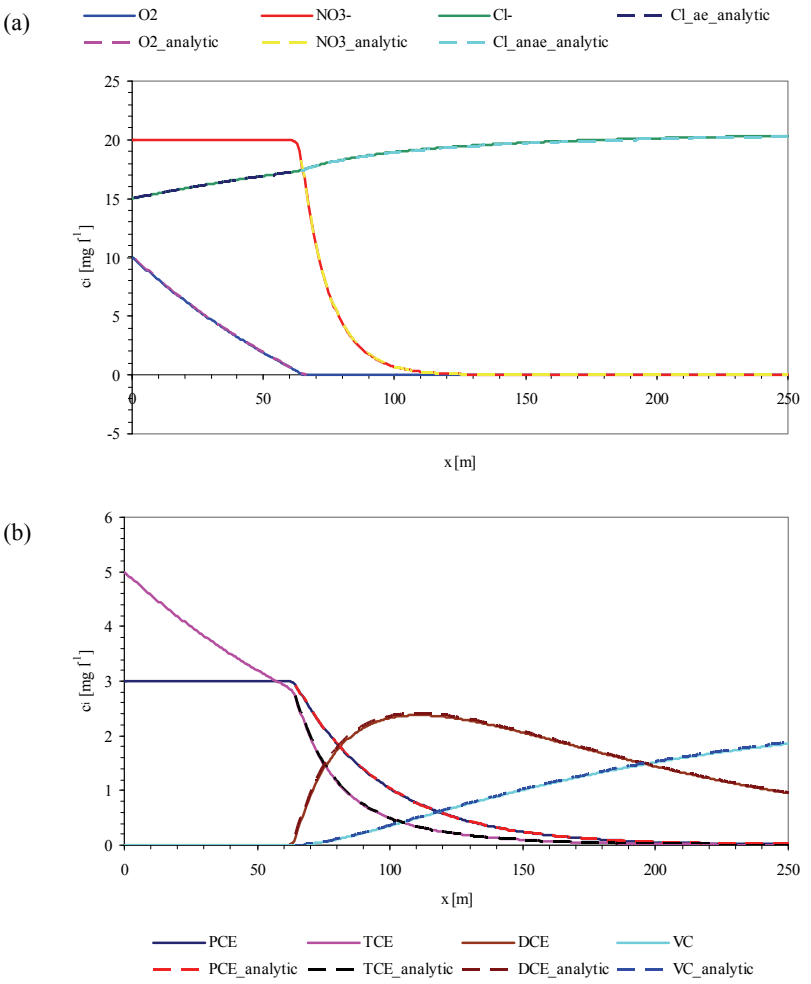

Figure 1.28 Concentration profiles along the *x*-axis at steady state (365 days), for (a) oxygen, nitrate, chloride, and (b) PCE, TCE, DCE, and VC. Darcy velocity = 0.4 m d^{-1}, adsorption = 0. Dashed lines represent analytical solutions.

Simulation results (a) show the extent of the aerobic zone versus the anaerobic zone. At 150 days, steady state is reached from x = 0 to x = 65 m for all species. Two separate aerobic zones appear from x = 0 to 65 m and from x = 165 m to the outlet. Anaerobic conditions are found between these two zones, allowing the degradation of nitrate and the sequential degradation of PCE into TCE, DCE and VC. Under aerobic conditions, the fast increase in chloride is a result of the complete mineralization kinetics of TCE. After 365 days, the anaerobic zone extends from x = 65 m to the outlet. The sequential degradation of chlorinated solvents leads to an accumulation of VC. The analytical solutions are obtained for each species, for the aerobic domain first, then for the anaerobic domain, by applying the decoupling solution of Sun *et al*.[21] to Bear's one-dimensional transport and reaction analytical solution. No method was found to solve the problem analytically in transient state, because the solution must include a switching term between aerobic and anaerobic rates of reactions as a function of the oxygen concentrations, which are varying in space and in time. On the other hand, steady state offers by definition a stable space and time limit between aerobic and anaerobic conditions. Thus, it is possible to solve first the aerobic domain, and to take the concentrations calculated at the end of the domain as boundary conditions for the calculations in the anaerobic domain. To avoid the development of a solution for parallel reactions, the contributions of each chlorinated solvent to the production of chloride under anaerobic conditions are solved separately and added to the chloride concentration obtained at steady state at the end of the aerobic zone. The results given by FEFLOW for all species are quasi identical to the analytical solutions. A participant of the benchmark obtained quasi identical results on PHAST (USGS) and on a self-made code named VisualRFlow. A participant using RT3D had serious dispersion problems. Another participant developed his own code and got a much narrower anaerobic zone. All these codes use finite differences. FEFLOW as the only finite-element code used in this benchmark has proven a versatile and user-friendly simulation system that allows the definition of multi-species and multi-reaction transport problems of arbitrary complexity.

1.9.7 Acknowledgements

D. Etcheverry and Y. Rossier, the authors of the Chapter 1.9, wish to thank the French Environment and Energy Management Agency (ADEME) for financial support (Décision d'attribution d'une aide financière no. 0472C0004). The ADEME and its partners for the MACAOH project (BURGEAP, IFARE, IFP, IMFS, and IMFT) are thanked for allowing publication of these numerical results.

1.10 Summary and Conclusions

In this paper, the details for the multi-species transport in FEFLOW are reported. FEFLOW can be used to simulate any type of reaction kinetics with an arbitrary number of mobile or immobile species in 2D and 3D applications. Multi-species transport is also available for unsaturated problems, variable-density and nonisothermal problems.

The paper describes the basic theory of the multi-species transport. Reaction models are formulated for degradation, Arrhenius and Monod kinetics. The

numerical approach for solving the resulting nonlinear equation systems in the present finite-element context is thoroughly described. FEFLOW provides powerful adaptive predictor-corrector schemes with fully automatic time marching.

The reaction-kinetics editor FEMATHED represents a new and powerful formula editor for an interactive and graphical input of the required rate expressions at any level of complexity. The formulae can be combined with if-else statements. There is no need for an additional compiling and linking of the kinetics expressions. A sophisticated built-in code interpreter is available in FEFLOW which has been shown to be as fast as precompiled formulae. FEFLOW provides precompiled rate expressions for degradation, Arrhenius and Monod kinetics.

To illustrate and benchmark FEFLOW's multi-species transport functionality, a number of reactive transport example problems are posed and solved. The first example presents reactive chain applications in 1D and 3D, typical for radionuclide decay. The second example presents a comprehensive kinetic model for analyzing rate-limited contaminant one-site kinetic sorption reactions, typical for in-situ bioremediation problems. Comparisons to analytical solutions reveal very good agreements with the numerical FEFLOW results. The third example is focussed on a two-site equilibrium/kinetic sorption process combined with linear degradation suitable for pesticide transport. For this type of problems good agreements with the STANMOD analytical solutions are shown. The fourth example concerns more complex sequential and non-sequential chlorinated solvents degradation under variable aerobic-anaerobic conditions. This simulation issues from a benchmark within the MACAOH project of the French Environment and Energy Management Agency with some university and private partners.

FEFLOW's multi-species transport option is useful for analyzing different and complex chemical reaction problems in the subsurface. Radionuclide transport and biochemical processes in natural attenuation of contaminants are typical applications. Predictions from the simulations can be used for screening remediation alternatives and environmental risks.

Notation

Roman letters

A	variable	rate constant;
a	ML^{-3}	transformed concentration variable;
$a_{k,j}$	1	stoichiometric yield;
B	L	aquifer thickness;
B	variable	rate constant;
b	variable	rate constant;
b_1	$(ML^{-3})^{1-b_2}$	Freundlich sorption coefficient;
b_2	1	Freundlich sorption exponent;
C	ML^{-3}	concentration;
C_s	ML^{-3}	overall maximum concentration;
$\boldsymbol{C}$	ML^{-3}	nodal concentration vector;
$\boldsymbol{D}$	L^2T^{-1}	tensor of hydrodynamic dispersion;
$\overline{\boldsymbol{D}}$	L^3T^{-1}	depth-integrated dispersion tensor;
D_d	L^2T^{-1}	coefficient of molecular diffusion;
D	variable	rate constant;
$\boldsymbol{d}$	1	error vector;
d	variable	rate constant;

E	variable	rate constant;
e	variable	rate constant;
g	LT^{-2}	gravitational acceleration;
h	L	hydraulic head;
$\boldsymbol{I}$	1	unit tensor;
$\boldsymbol{K}$	T^{-1}	nodal conductance matrix;
K_d	L^3M^{-1}	equilibrium distribution coefficient;
k	T^{-1}	rate constant;
k_1	1	Langmuir 1st sorption coefficient;
k_2	L^3M^{-1}	Langmuir 2nd sorption coefficient;
L	L	length;
N		total number of chemical species;
$N°$		number of reactants;
N_r		number of reactions;
n	1	concentration exponent;
p	$ML^{-1}T^{-2}$	pressure;
Q	$ML^{-3}T^{-1}$	nonreactive production term;
$\overline{Q}$	$ML^{-3}T^{-1}$	bulk nonreactive production term;
$\widehat{Q}$	$ML^{-2}T^{-1}$	depth-integrated bulk nonreactive production term;
$\boldsymbol{q}$	LT^{-1}	Darcy velocity vector;
$\bar{\boldsymbol{q}}$	L^2T^{-1}	depth-integrated Darcy flux;
R	$ML^{-3}T^{-1}$	bulk rate of chemical reaction;
$\boldsymbol{R}$	$ML^{-3}T^{-1}$	nodal bulk rate vector;
$\underline{\mathfrak{R}}$	1	retardation factor;
$\mathfrak{R}$	L	depth-integrated retardation factor;
r	$ML^{-3}T^{-1}$	rate of reaction;
S	ML^{-3}	sorbed concentration;
$\boldsymbol{S}$	1	nodal storage matrix;
s	1	saturation;
T	Θ	temperature;
t	T	time;
$\boldsymbol{v}$	LT^{-1}	pore velocity vector;
x	L	spatial coordinate;
y	1	stoichiometric yield;

Greek letters

α	L^3M^{-1}	solutal expansion coefficient;
α	T^{-1}	desorption rate constant;
$\bar{\alpha}$	1	fluid density difference ratio;
β	Θ^{-1}	thermal expansion constant;
β_L, β_T	L	longitudinal and transverse dispersivity, respectively;
γ	$M^{-1}LT^2$	fluid compressibility;
$\bar{\gamma}$	L^{-1}	specific fluid compressibility;
Δt	T	temporal increment;
Δx	L	spatial increment;
δ	1	error tolerance;
ε	1	porosity, void space;
ε_α	1	volume fraction of α -phase;
ε_s	1	solid volume fraction;
ϑ	T^{-1}	decay rate constant;
κ	1	Henry sorption coefficient;
κ_k	variable	bulk rate constant of species k;
μ	$ML^{-1}T^{-1}$	dynamic viscosity;
ρ	ML^{-3}	density;
Ξ	1	rate for changing time step size;
ν_{kr}	1	stoichiometric number;
χ	1	adsorption function;
ω	1	density factor;
∇	L^{-1}	Nabla (vector) operator;

Subscripts

α	phase indicator;
b	bulk;
f	fluid phase;

het	heterogeneous;
hom	homogeneous;
i	species index;
j	species index;
k	species indicator;
m	species index;
n	time plane or species index;
o	initial value;
r	reaction;
s	solid phase;

Superscripts

ae	aerobic;
anae	anaerobic;
α	phase indicator;
f	fluid phase;
n	time plane;
max	maximum value;
p	predictor value;
s	solid phase;

Abbreviations

AB	Adams-Bashforth;
AB/TR	Adams-Bashforth/trapezoid rule scheme;
BE	backward Euler;
BTEX	bezene-toluene-xylene mixture;
DCE	cis- and trans-1,2-dichloroethylene;
EOS	equation of state:
FE	forward Euler;
FE/BE	forward Euler/backward Euler scheme;
ID	identifier of species;
LMA	law of mass action;
MACAOH	Modélisation de l'atténuation des composés organo-chlorés dans les aquifères;
PCE	perchloroethylene;
RMS	root-mean square;
SIA	sequential interactive approach;
TCE	trichloroethylene;
TR	trapezoid rule;
VC	vinyl chloride;

References

1. Bear, J. and Bachmat, Y. *Introduction to modeling of transport phenomena in porous media*. Kluwer Acad. Press, Dordrecht, 1991.
2. Clement, T.P. *RT3D - A modular computer code for simulating reactive multi-species transport in 3-dimensional groundwater systems*. Documentation. Version 1.0, Pacific Northwest National Laboratory, Richland, Washington 99352, 1997.
3. Clement, T.P., Sun, Y., Hooker, B.S. and Petersen, J.N. Modeling multi-species reactive transport in groundwater aquifers. *Groundwater Monitoring & Remediation Journal* **18** (1998)2, 79-92.
4. Diersch, H.-J.G., *Modeling and numerical simulation of geohydrodynamic transport processes* (in German). Reprint, WASY Ltd. Berlin, 1991.
5. Diersch, H.-J.G. Interactive, graphics-based finite-element simulation system FEFLOW for modeling groundwater flow, contaminant mass and heat transport processes. Release 5.2, *Reference Manual*, WASY Ltd., Berlin, 2005.
6. Diersch, H.-J.G. On the primary variable switching technique for simulating unsaturated-saturated flows. *FEFLOW White Papers Vol. I*, Chapter 1, WASY Ltd. 2002, Berlin, pp. 9-66.
7. Diersch, H.-J.G. About the difference between the convective form and the divergence form of the transport equation. *FEFLOW White Papers Vol. I*, Chapter 6, WASY Ltd. 2002, Berlin, pp. 119-129.

8. Diersch, H.-J.G. Chemical reactions. *FEFLOW White Papers Vol. I*, Chapter 10, WASY Ltd. 2002, Berlin, pp. 191-206.
9. Diersch, H.-J.G. Coupled groundwater flow and transport: Thermohaline and 3D convection systems. *FEFLOW White Papers Vol. I*, Chapter 17, WASY Ltd. 2002, Berlin, pp. 307-349.
10. Diersch, H.-J.G. and Kolditz, O. Variable-density flow and transport in porous media: approaches and challenges. *Adv. Water Resour.* **25** (2002), 899-944.
11. Fry, V.A., Istok, J.D., and Guenther, R.B. An analytical solution to the solute transport equation with rate-limited desorption and decay. *Water Res. Resour.* **29** (1993)9, 3201-3208.
12. Garcia-Talavera, M. Laedermann, J.P., Decombaz, M., Daza, M.J. and Quintana, B. Coincidence summing corrections for the natural decay series in γ-ray spectrometry. *J. Radiation and Isotopes* **54** (2001), 769-776.
13. Kanney, J.F., Miller, C.T. and Kelley, C.T. Convergence of iterative split-operator approaches for approximating nonlinear reactive transport problems. *Adv. Water Resour.* **26** (2003)3, 247-261.
14. Lichtner, P.C., Continuum formulation of multicomponent-multiphase reactive transport. In: *Reactive transport in porous media*, ed. by Lichtner *et al.*, Reviews in Mineralogy, Vol. 34, Mineralogical Soc. Am., Washington DC, 1996, pp. 1-81.
15. Lindstrom, F.T., Pulsed dispersion of trace chemical concentrations in a saturated sorbing porous medium. *Water Res. Resour.* **12** (1976), 229-238.
16. Nguyen, V.V., Gray, W.G., Pinder, G.F., Botha, J.F. and Crerar, D.A. A theoretical investigation on the transport of chemicals in reactive porous media. *Water Res. Resour.* **18** (1982)4, 1149-1156.
17. Rifai, S.H., Newell, C.J. Miller, R., Taffinder, S. and Rounsaville, M. Simulation of natural attenuation with multiple electron acceptors. *Bioremedation* **3** (1995)1, 53-58.
18. STANMOD (STudio of ANalytical MODels): Computer software for evaluating solute transport in porous media using analytical solutions of convection-dispersion equation. *http://www.ars.usda.gov/services/software/software.htm*.
19. Stumm, W. and Morgan, J.J. *Aquatic chemistry.* Wiley-Interscience, New York, 1981.
20. Sun, Y., Petersen, J.N., Clement, T.P. and Skeen, R.S., Development of analytical solutions for multispecies transport with serial and parallel reactions. *Water Res. Resour.* **35** (1999)1, 185-190.
21. Sun, Y., Petersen, J.N. and Clement, T.P. Analytical solutions for multiple species reactive transport in multiple dimensions. *Journal of Contaminant Hydrology* **35** (1999), 429-440.
22. Toride, N., Leij, F.J. and van Genuchten, M.Th. The CXTFIT code for estimating transport parameters from laboratory or field tracer experiments. Vers. 2.1, US. Salinity Lab. Riverside, Cal., Research Report No. 137, 1999.
23. Wiedemeier, T.H., Swanson, M.A., Wilson, J.T., Kampbell, D.H., Miller, R.N. and Hansen, J. Approximation of biodegradation rate constants for monoaromatic hydrocarbons (BTEX) in groundwater. *Groundwater Monitoring & Remediation Journal* **16** (1996)3, 186-194.
24. Wiedemeier, T.H., Swanson, M.A., Moutoux, D.E., Kinzie Gordon E., Wilson, J.T., Wilson B.H., Kampbell, D.H., Haas, P.E., Miller, R.N., Hansen, J.E. and Chapelle, F.H. Technical protocol for evaluating natural attenuation of chlorinated solvents in ground water. EPA/600/R-98/128. U.S. Environmental protection agency, 1998.
25. van Genuchten, M.Th. and Wagenet, R.J. Two-site/two-region models for pesticide transport and degradation: Theoretical development and analytical solutions. *Soil Sci. Soc. Am. J.* **53** (1989)5, 1303-1310.

Parameter estimation of transient flow problems with PEST in FEFLOW

2

Jan Christian Kaiser

ITUPH Institut für Theoretische Umweltphysik, Munich, Germany

2.1 Introduction

The integration of the PEST package for parameter estimation (Doherty *et al.*[6]) into the FEFLOW simulator[4] was accomplished in FEFLOW's version 4.8 for stationary flow processes. The coupling has been realized via FEFLOW's interface manager (see Gründler[8]) using the method of direct implementation. The PEST module has access to FEFLOW's address space and is called within its graphical user interface. Data exchange is facilitated during run time with callback functions. A description of the PEST-FEFLOW coupling is given in Kaiser[11].

In FEFLOW's version 5.2 the range of applicability of parameter estimation with PEST has been extended to transient flow problems. The extension required only minor changes in the PEST graphical user menu for observations, since the time-dependent observation curves are treated as power functions, for which FEFLOW provides a comprehensive data management.

From a theoretical point of view the analysis of transient simulation models, which produce predictions for observable physical quantities, will profit from the application of concepts and methods of data assimilation. In this analysis technique observed information (i.e. measured gauge curves of hydraulic heads) is used to improve the model state (i.e. FEFLOW's material parameters) and to enhance the predictive power of the model. Two basic approaches to data assimilation are known (Bouttier and Courtier[1]):

- *Sequential assimilation*, which considers only observations from the past until the time of analysis. This is the case for models of meteorological weather forecast or flood forecast models in real-time applications.
- *Retrospective assimilation*, where observations from any conceivable time range can be used for model calibration and validation. Groundwater models are typically treated with this approach.

Both approaches can use the observed information either intermittently or continuously in time. In the intermittent mode, observations are grouped in time intervals, which are much smaller than the total simulation time but much larger than the time scales of the underlying physical processes. Usually, this mode is

technically convenient. In the continuous mode observations over the whole simulation time of the model are considered to improve the model state, which is physically more realistic.

Most subsurface flow models are conveniently treated with retrospective data assimilation in the continuous mode. To make use of the PEST algorithm to minimize the objective function, the model parameters must be constant in time. The general data assimilation concept includes time dependent model parameters as well. However, in this case the Kalman filter technique should be used for the parameter update. This technique is mathematically equivalent to the minimization of the objective function†) (Bouttier and Courtier[1]).

In the present implementation complete use of the observed information is made by considering measurements at each observation point i of the model and at each time step t_j. Measured hydraulic heads $o_i(t_j)$ can be compared with model predictions $M_i(t_j, \boldsymbol{p})$ by using the callback function `OnTimeStepConstraint()` of the interface manager. This functions ensures, that the hydraulic head is calculated for the whole finite element grid at a prescribed time step irrespectively of the selected algorithm for time stepping. The vector $\boldsymbol{p}$ contains the time-constant material parameters of FEFLOW, which are updated in the estimation process.

Now the objective function $J(\boldsymbol{p})$ can be constructed with the residual vectors $\boldsymbol{o}_i(t) - \boldsymbol{M}_i(t, \boldsymbol{p})$ and the covariance matrix $\boldsymbol{R}_i^{-1}$ of the measurement errors

$$J(\boldsymbol{p}) = \sum_{i=1}^{n} (\boldsymbol{o}_i(t) - \boldsymbol{M}_i(t, \boldsymbol{p}))^T \boldsymbol{R}_i^{-1} (\boldsymbol{o}_i(t) - \boldsymbol{M}_i(t, \boldsymbol{p})) \quad (2\text{-}1)$$

by summing over all n observation points. The vector

$$\boldsymbol{o}_i(t) = \begin{pmatrix} o_i(t_1) \\ \dots \\ o_i(t_m) \end{pmatrix} \quad (2\text{-}2)$$

contains the recorded measurements of the hydraulic head for m time steps of the gauge curve pertaining to observation point i. For the vector $\boldsymbol{M}_i(t, \boldsymbol{p})$ an analogous expression is valid. Measurement errors are modeled here in a simplified way. They are treated as uncorrelated and identical for a given observation point. After normalization they are represented as weights of the gauge curves. Note, that for each observation point an individual sequence of time steps exists, which may or may not differ from the sequences of other observation points. The set of FEFLOW material parameters $\boldsymbol{p}_{\min}$ minimizes the objective function $J(\boldsymbol{p})$ and can be considered as the optimal parameter set of the parameter estimation problem. A full description of the mathematical framework of PEST and of the algorithms to minimize the objective function is given in Doherty *et al.*[6].

In the following section four simple test examples are presented to demonstrate the reliability of the implementation of PEST in FEFLOW for transient flow problems. The examples cover both confined and unconfined aquifers with measured and synthetically generated observation data. In Theis' well problem for

†) called 4D variational assimilation (4D VAR) in Bouttier and Courtier[1].

an unconfined aquifer synthetically generated gauge curves are used to retrieve the material parameters of a FEFLOW benchmark problem. The pump tests of Breyell and Wichita have been conducted in a confined and an unconfined aquifer. They were analyzed already by Langguth and Voigt[12] with graphical evaluation methods. Here they have been reanalyzed with PEST in FEFLOW to compare the results of both approaches. Finally, a generic floodwave problem has been set up to assess the results of a parameter estimation, which is influenced by the consequences of non-uniqueness.

2.2 Test Examples

2.2.1 Theis' well problem

Theis' problem of the lowering of a water table by a pumping well is a famous benchmark problem for numerical algorithms since it possesses an analytical solution couched in the well-known well function (Theis[14]). The complete solution of the governing partial differential equation of second order

$$\frac{S}{T}\frac{\partial h}{\partial t} - \frac{\partial^2 h}{\partial r^2} - \frac{1}{r}\frac{\partial h}{\partial r} = 0 \qquad (2\text{-}3)$$

for a confined aquifer in a radial symmetric geometry with the boundary conditions of a constant flux q into a pumping well of infinitely small radius and a constant head h_o at the outer fringe, which is very far away from the well, has been derived by Theis by exploiting the analogy to a heat conduction problem (Carslaw and Jaeger[2]). The initial condition $h_o(0, r)$ is a constant head of zero at $t = 0$ in the whole plane, except at the wellbore where $h(0, r_b) = -0.01\,\mathrm{m}$. All symbols are explained in Tab. 2.1.

The time stepping algorithms of the FEFLOW groundwater simulator have been successfully tested against the Theis benchmark (Diersch[5]) on the finite element grid of Fig. 2.1. Here the same grid with the same values for the simulation parameters (Tab. 2.1) is used to test the implementation of the PEST algorithm for the estimation of parameters in transient flow problems. The simulation was done with automatically controlled time steps based on the first order (FE/BE) predictor-corrector techniques.

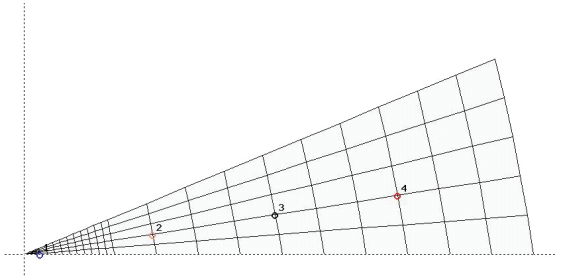

Figure 2.1 FEFLOW grid with PEST observation points for Theis' well problem.

The coordinates of the observation points on the FEFLOW grid are given in Tab. 2.2. At these points the drawdown of the Theis problem has been recorded. For PEST 15 time steps at each observation point have been selected with an approximately constant distance on a logarithmic scale (Fig. 2.3). The PEST estimation problem has been set up in one zone which comprised all nodes of the FEFLOW grid. The transmissivity T and the storage coefficient S have been estimated

simultaneously using the initial values of 10^{-4} m^2s^{-1} and 10^{-3}, respectively. The optimization control parameters of PEST have been left at their default values.

Table 2.1 Simulation parameters for Theis' well problem

Name	Symbol	Unit	Value
wellbore radius	r_b	m	0.3048
flow initial	$h(0, r)$	m	0
flow initial at wellbore	$h(0, r_b)$	m	-0.01
well pumping rate	$q = \frac{Q}{2\pi r_b}$	m^2d^{-1}	638.75425
fixed head at outer boundary	$h(t, 304.8\,\mathrm{m})$	m	0
transmissivity	T	m^2s^{-1}	$9.2903 \cdot 10^{-4}$
storage coefficient	S	-	0.001
storage compressibility	S_o	-	0

Table 2.2 Coordinates and distance from the pumping well of the observation points for Theis' well problem

Observation point no.	Coordinates		Distance
	x[m]	y[m]	r[m]
1	9.64	0	9.64
2	76.98	12.16	77.93
3	150.28	23.75	152.15
4	223.57	35.33	226.34

The course of the PEST objective function during the optimization is shown in Fig. 2.2. With the starting values for T and S the objective function reaches some 10^4 for in total 60 time steps from 4 observation points. After 26 model runs it has been minimized to $2.5 \cdot 10^{-6}$ by passing through 10 orders of magnitude. The model runs no. 27-39 are used by PEST to verify that a minimum of the objective function has been actually reached.

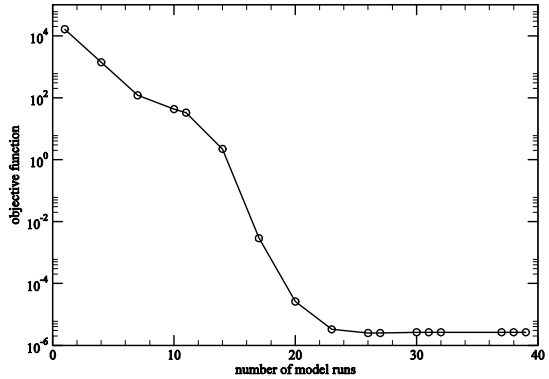

Figure 2.2 Minimization of the PEST objective function for Theis' well problem.

The estimated values from PEST are $9.2902 \cdot 10^{-4}$ m^2s^{-1} and $1.0002 \cdot 10^{-4}$ for T and S, respectively. For both parameters PEST produced highly accurate point estimates which deviate only in the fifth digit from the true values of Tab. 2.1. The correlation coefficient for T and S is -0.57 and indicates a relatively weak correlation favouring an effective parameter estimation. Figure 2.3 exhibits a perfect agreement of 'measured' and

predicted hydraulic heads at the observation points which should have been expected with the highly precise point estimates from PEST. This figure also demonstrates that after some 0.1 d the hydraulic head becomes constant at all observation points owing to a simulation system of finite extent. On the other hand, with growing distance from the pumping well, the begin of the drawdown is delayed. Therefore, the information from observation point 4 alone is not sufficient to estimate the material parameters, because of the short drawdown phase. However, with the drawdown curve of observation point 1 alone a very precise parameter estimation is always possible.

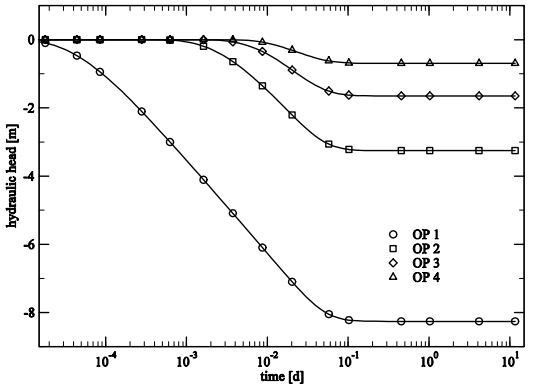

Figure 2.3 Comparison of measured (symbols) and predicted (full lines) hydraulic heads for the four observation points (OP) of Theis' well problem.

2.2.2 Breyell pump test

The pump test of the Breyell waterworks (Langguth and Voigt[12]) has been evaluated on the basis of the analytical results of Theis[14]. The test has been conducted in a confined aquifer in the Lower Rhine region near the city of Krefeld. The sequence of geological layers has been subdivided in an upper unconfined aquifer which is separated by a layer of very impermeable clay from the lower unconfined aquifer. During the test the pumping rate was held constant at $Q = 2.67 \cdot 10^{-2}$ m^3s^{-1}. The drawdown has been observed at three gauges: gauge 11b at a distance of 7.4 m, gauge 3b at a distance of 23 m and gauge 6b at a distance of 139.6 m from the well. The recorded drawdown curves, copied from Langguth and Voigt[12], are given in the Tables 2.3, 2.4 and 2.5. For gauge 11b also the rerise has been recorded after the pump was stopped at $t = 0.1690$ d. The measured values are shown in Tab. 2.6. All measured curves for the Breyell pump test are depicted in Fig. 2.5.

Table 2.3 Measured drawdown at gauge 11b with $r = 7.40$ m for the Breyell pump test

Time [10^{-4} d]	Drawdown [m]
1.968	0.30
2.431	0.40
3.125	0.50
4.051	0.70
6.134	0.93

Table 2.3 Measured drawdown at gauge 11b with r = 7.40 m for the Breyell pump test (continued)

Time [10^{-4} d]	Drawdown [m]
9.838	1.03
19.44	1.20
25.46	1.28
32.52	1.35
38.19	1.40
52.08	1.47
62.50	1.50
83.33	1.56
125.0	1.64
166.7	1.71
243.1	1.79
347.2	1.86
451.4	1.90
625.0	1.99
960.6	2.07
1690	2.18

Table 2.4 Measured drawdown at gauge 3b with r = 23 m for the Breyell pump test

Time [10^{-4} d]	Drawdown [m]
1.389	0.05
2.083	0.10
2.546	0.15
4.167	0.25
6.250	0.35
9.375	0.45
14.12	0.55
26.16	0.70
40.04	0.80
50.23	0.85
63.54	0.90
79.75	0.95
99.65	1.00
125.0	1.05
164.4	1.11
208.3	1.15
250.0	1.20
319.4	1.25
402.8	1.30
506.9	1.35

Table 2.4 Measured drawdown at gauge 3b with r = 23 m for the Breyell pump test (continued)

Time [10^{-4} d]	Drawdown [m]
611.1	1.39
937.5	1.48
1342	1.55
1638	1.58

Table 2.5 Measured drawdown at gauge 6b with r = 139.60 m for the Breyell pump test

Time [10^{-4} d]	Drawdown [m]
27.78	0.14
41.67	0.20
69.44	0.25
90.28	0.29
131.9	0.35
173.6	0.40
236.1	0.45
319.4	0.50
451.4	0.55

Table 2.5 Measured drawdown at gauge 6b with r = 139.60 m for the Breyell pump test (continued)

Time [10^{-4} d]	Drawdown [m]
555.6	0.59
746.5	0.65
1001	0.71
1325	0.76
1609	0.80

Table 2.6 Measured rerise at gauge 11b after the pump stop at t = 0.169 d

Time [10^{-4} d]	Drawdown [m]
1690	2.18
1709	1.03
1716	0.95
1721	0.90
1727	0.85
1763	0.69
1775	0.65
1806	0.59
1830	0.55

Table 2.6 Measured rerise at gauge 11b after the pump stop at $t = 0.169$ d (continued)

Time [10^{-4} d]	Drawdown [m]
1873	0.47
1898	0.44
2002	0.35
2072	0.30
2148	0.26
2225	0.23
2396	0.17
2697	0.09

Langguth and Voigt[12] have given estimates for the transmissivity T and the storage compressibility S using graphical evaluation methods of Theis[14], and Cooper and Jacob[3], respectively. Theis' method is based on the graphical matching of a modified well function with scaled curves of the recorded drawdown. Cooper and Jacob[3] use the exponential behavior of the drawdown which dominates the process asymptotically for sufficiently large times. A detailed description of both methods is not the subject of this paper, it is given in Langguth and Voigt[12]. All estimates for T and S are summarized in Tab. 2.7. The averages over all estimates are $97 \cdot 10^{-4}$ m^2s^{-1} for T and $3.7 \cdot 10^{-4}$ for S. The corresponding maximal relative deviations are 24 % for T and -43 % for S. Hence, the storage compressibility S shows a larger variability and can only be estimated with less precision.

Table 2.7 Summary of estimates for the transmissivity *T* and the storage compressibility *S* of the Breyell pump test from Langguth and Voigt[12]

Gauges used for estimation	Transmissivity T [10^{-4} m^2s^{-1}]	Storage compressibility S [10^{-4}]
Theis' superposition method		
11b & 3b & 6b together	110	2.4
Time-drawdown-method (Cooper and Jacob[3])		
6b alone	120	2.1
3b alone	94	4.6
11b alone	89	3.7
Distance-drawdown-method (Cooper and Jacob[3])		
11b & 3b & 6b together	90	4.8

Table 2.7 Summary of estimates for the transmissivity *T* and the storage compressibility *S* of the Breyell pump test from Langguth and Voigt[12] (continued)

Gauges used for estimation	Transmissivity T $[10^{-4}\ m^2s^{-1}]$	Storage compressibility S $[10^{-4}]$
Distance-time-drawdown-method (Cooper and Jacob[3])		
11b & 3b & 6b together	89	4.6
Rerise method (Jacob[9])		
11b alone	84	n.a.

In FEFLOW the pump test is modeled in a 2D problem for confined aquifers on a mesh with 2138 3-noded triangles. The outline of the mesh consists of a circle segment with an opening angle of 30° and a radius of 1500 m. The mesh is based on two superelements. The first superelement covers the zone near the well up to the radius of 150 m with a higher spatial resolution of the finite elements. This zone is shown in Fig. 2.4 together with the location of the pumping well and the three gauges 6b, 3b, and 11b, respectively. The pumping well is modeled with a boundary condition of the 4th kind at the tip of the circle segment. On the outer boundary a constant head of 0 m is prescribed with a boundary condition of the 1st kind. The initial head on all nodes was set to zero.

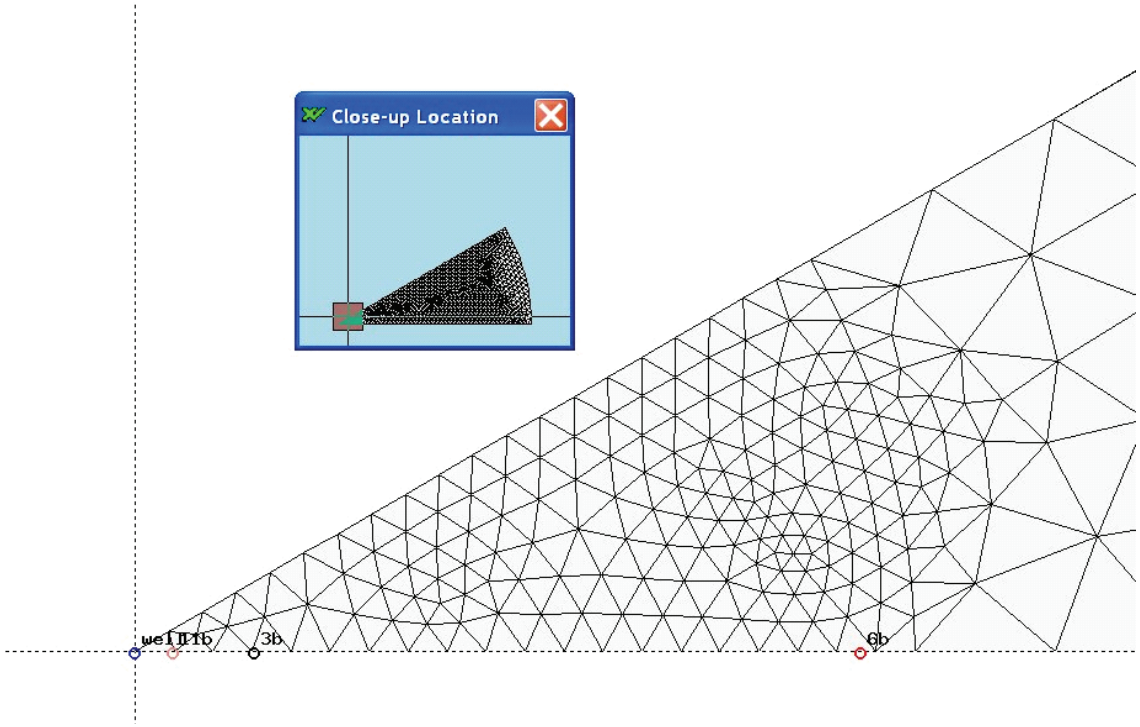

Figure 2.4 Finite element grid near the pumping well at the tip with gauges 11b at r = 7.40 m, 3b at r = 23.00 m and 6b at r = 139.60 m.

With PEST the transmissivity T and the storage compressibility S have been estimated simultaneously in one zone which covered the whole mesh. The initial values were chosen to be 10^{-4} m^2s^{-1} and $4 \cdot 10^{-4}$, respectively. The control parameters for the optimization process have been left at their default values. Also the correlation structure of the two estimated parameters has been calculated. To allow for a direct comparison with the results from Langguth and Voigt[12] a series of estimation runs has been conducted. Firstly, the drawdown curves were used separately to produce the parameter estimates. Then the drawdown curves of the Tables 2.3 to 2.5 have been used together in one estimation run. Also the rerise curve of Tab. 2.6 was used in a separate run. Finally, a PEST problem has been set up using all recorded 75 observation points from the Tables 2.3 to 2.6.

Table 2.8 contains the point estimates of the six PEST estimation runs for the transmissivity T and the storage compressibility S. Owing to the narrow width of the objective function near the minimum, the 95 % confidence intervals (CI) are mostly around one digit. Only for the PEST run using gauge 6b alone, which has the largest distance from the pumping well, the CI were notably larger. In this run, which needed 73 model calls to converge, the correlation coefficient between T and S is almost one. In all other PEST runs the correlation coefficient is negative and around 30 model calls were necessary. The absolute value is minimal if the time steps for the rerise in gauge 11b is included in the estimation. Small correlation coefficients favour the stability of the optimization process.

The point estimates for T exhibit a similar variability as those from Langguth and Voigt[12] in Tab. 2.7. The estimates of T decrease with decreasing distance from the pumping well. Langguth and Voigt[12] observe the same trend. The PEST estimates for S differ by some factor of four whereas in Langguth and Voigt[12] the spread is markedly lower. For both T and S the averages over all estimates agree well with PEST point estimates of the last line of Tab. 2.8 which were obtained by using all information of the 75 measured time steps in one estimation run.

In Fig. 2.5 the curves of the measured and predicted drawdown are compared. To calculate the predicted drawdown the point estimates of the last line of Tab. 2.8 were used. The agreement is very good except for the late phase of the rerise in gauge 11b. During the pump test the pore structure of the aquifer may change so that drawdown and rerise cannot be described with one pair of constant parameter values for T and S. However, in general, with PEST in FEFLOW the results for the Breyell pump test of Langguth and Voigt[12] have been fully confirmed.

Table 2.8 Parameter estimates and statistical information of the PEST estimation runs for the Breyell pump test

Gauges used for estimation	Transmissivity T [10^{-4} m^2s^{-1}]	Storage compressibility S [10^{-4}]	Objective function J	Number of observation points N_{obs}	$\sqrt{J}/N_{obs}$	Correlation coefficient
6b alone	117	2.35	$1.7 \cdot 10^{-3}$	14	$3.0 \cdot 10^{-3}$	0.99
3b alone	90.7	5.12	$1.9 \cdot 10^{-2}$	24	$5.7 \cdot 10^{-3}$	-0.78
11b alone	79.8	7.91	$2.0 \cdot 10^{-1}$	21	$2.1 \cdot 10^{-2}$	-0.82
6b & 3b & 11b	88.2	5.03	$3.7 \cdot 10^{-1}$	59	$1.0 \cdot 10^{-2}$	-0.77
11b rerise only	96.8	1.81	$2.5 \cdot 10^{-2}$	17	$9.3 \cdot 10^{-3}$	-0.65
all observation points	92.0	4.31	$4.7 \cdot 10^{-1}$	75	$9.2 \cdot 10^{-3}$	-0.55

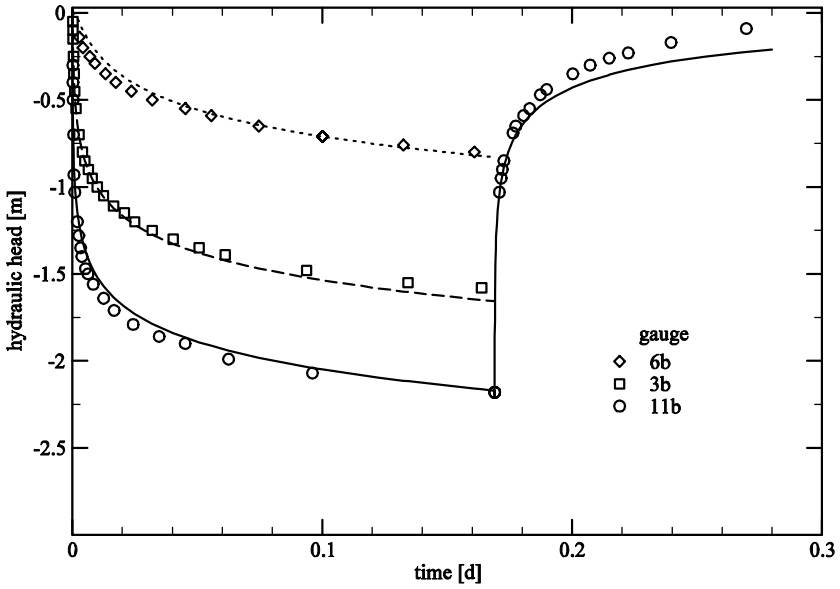

Figure 2.5 Measured (symbols) and predicted (lines) drawdown for the gauges 6b (diamonds, dotted line), 3b (squares, broken line) and 11b (circles, full line) of the Breyell pump test.

2.2.3 Wichita pump test

The Wichita pump test (Langguth and Voigt[12]) has been conducted in an unconfined aquifer. If the assumption of Dupuit (1863) is valid, the well formulas of Theis[14] can also be applied to aquifers with free water tables with sufficient accuracy. In practical applications the maximal drawdown must be small (i.e. < 15 % of the original water-filled height of the aquifer). However, this is not the case for the Wichita pump test with a water-filled height of 8.20 m and a maximal drawdown of 1.80 m at a gauge with a distance of 15.00 m from the pumping well. This value was recorded after 18 d when the well was operated at an average pumping rate of $Q = 6.31 \cdot 10^{-2}\ m^3s^{-1}$. Values for in total six gauges, which have been arranged in two rows in the north and the south of the pumping well, are given in Tab. 2.9. Langguth and Voigt[12] have evaluated the pump test with a graphical method of

Cooper and Jacob[3]. To account for the deviation from Dupuit's assumption they corrected the recorded drawdown s and used a lower drawdown $s' = s - s^2/2B$ instead, where B denotes the original water-filled height of the aquifer (Jacob[10]).

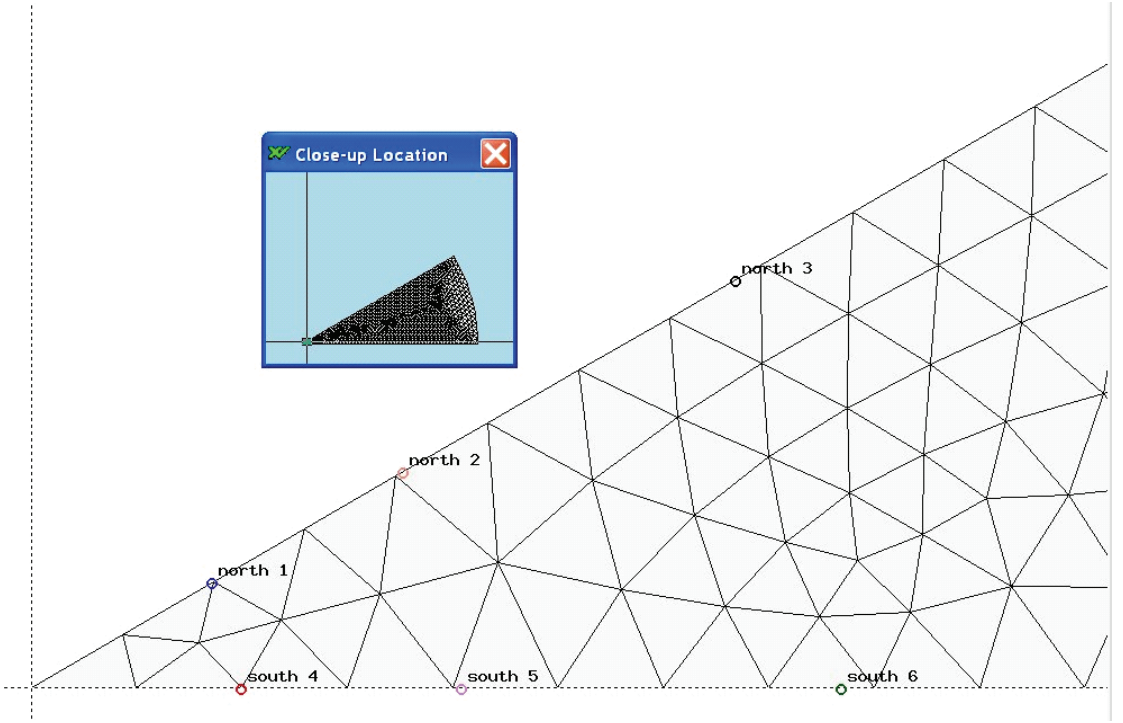

Figure 2.6 Finite element grid for the Wichita pump test with the location of the northern gauges 1-3 and the southern gauges 4-6.

For the simulation of the pump test with PEST in FEFLOW the same circle segment as for the Breyell pump test was used with a radius of 1500 m and an opening angle of 30°. A cut of the grid near the tip with the location of the six gauges of Tab. 2.9 is shown in Fig. 2.6. Owing to the radial symmetry the results depend only on the distance between the gauge and the pumping well at the tip. The pumping well was modeled with a well boundary condition of the 4th kind. At the outer radius a constant head boundary condition of 0 m has been prescribed. The problem has been set up in 2d with an unconfined aquifer of -8.20 m bottom elevation. The initial head at all nodes has been set to zero. The final simulation time was 20 d.

Table 2.9 Distance to pumping well and observed drawdown at t = 18 d for the 6 gauges of the Wichita pump test

Gauge no.	Distance to pumping well [m]	Drawdown [m]
northern row		
1	15.00	1.80
2	30.70	1.40
3	57.70	1.04
southern row		
4	14.95	1.67
5	30.60	1.31
6	57.90	0.97

For PEST the six gauges of Tab. 2.9 were used as observation points. The definition of the time-dependent power functions in FEFLOW requires at least two time steps, but at the gauges measurements had been taken only at one time step of 18 d. Therefore, to obtain six valid power functions to each time step the initial hydraulic head 0 m at t = 0 was added. Note, that with this measure no additional information has been introduced into the estimation problem, because the initial condition is already known without a need to run the model. It does not depend on changes of the model parameter. The two material parameters hydraulic conductivity and storage compressibility have been estimated simultaneously with the start values of 10^{-2} ms^{-1} and 0.2, respectively.

The minimum of the objective function at 0.016 was reached in 7 optimization iterations after 35 model runs. In Tab. 2.10 the PEST point estimates are compared with the results of the graphical evaluation method of Langguth and Voigt[12]. For the hydraulic conductivity the point estimate of PEST lies close to the estimate of the graphical evaluation method using the corrected drawdown. The PEST estimate of the storage compressibility overestimates value from the method with the corrected drawdown by some ten percent. The agreement of the estimates for both material parameters from PEST is better with the estimates from the method using the corrected drawdown. This agreement justifies the application of this method from hindsight.

The very large 95 % CI of the PEST point estimates for the storage compressibility indicate a broad minimum of the objective function. The estimated material parameters show a large negative correlation of almost -99 %. Both observations indicate that the Wichita pump test poses a more difficult estimation problem than the Breyell pump test.

In Fig. 2.7 the predicted drawdown curves for the three northern gauges are shown. Those for the southern gauges have been omitted because they are almost identical within the drawing accuracy. The predicted curves pass between measured points of the northern and southern gauges which is an indication of the plausibility of the estimation result.

Table 2.10 Estimates for the flow parameters of the Wichita pump test

Parameter		Graphical evaluation (Langguth and Voigt[12])		PEST in FEFLOW (95 % confidence intervals in brackets)
Name	Unit	with measured drawdown	with corrected drawdown	
conductivity	[10^{-4} ms^{-1}]	23	28	27 (15;47)
storage compressibility	[-]	0.44	0.30	0.34 (0.05;24)

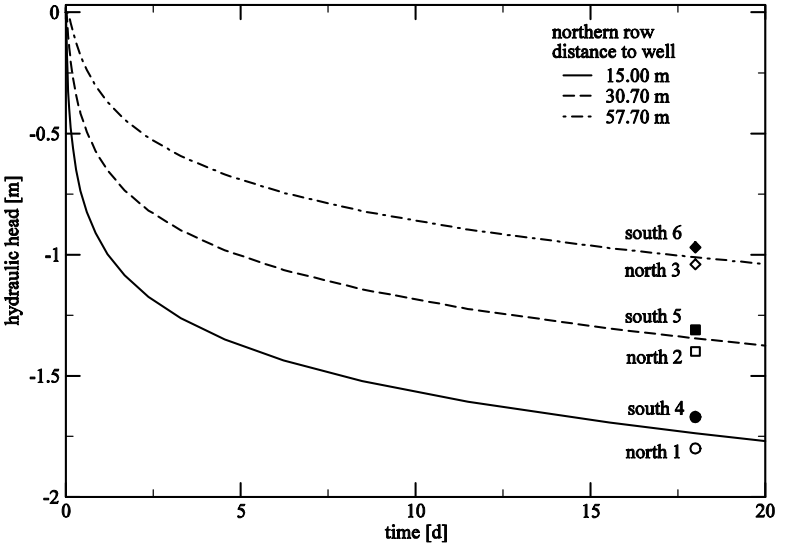

Figure 2.7 Measured observation points at t = 18 d for both the northern row (open symbols) and the southern row (full symbols) of gauges, predicted gauge curves only for the northern row.

2.2.4 Floodwave problem

In this example a passing floodwave in a river is used to estimate the hydraulic properties of the river bed and the connected aquifer from the response of the hydraulic head. In FEFLOW a (quasi-) 1D problem has been set up for an unconfined aquifer of 10 m thickness on a finite element grid of 100 m length, using 100 4-noded quadrilateral mesh elements as shown in Fig. 2.8. At the right edge a time-dependent boundary condition of the 3rd kind has been applied. The floodwave is modeled by a linear rise of the water table in the river of 3 m during one day, followed by a subsequent drop to the initial value on the next day. It is shown in Fig. 2.9. At the left edge a no-flow boundary condition is applied.

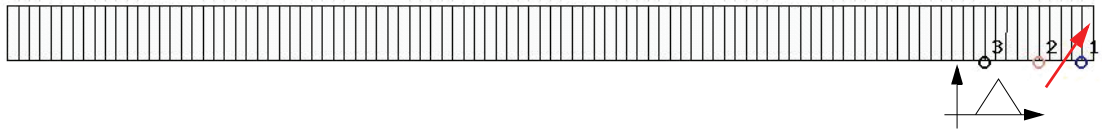

Figure 2.8 Finite element grid for the floodwave problem with the location of the observation points 1 (at 1 m), 2 (at 5 m) and 3 (at 10 m); both shape and position of the time-dependent floodwave boundary condition of the 3rd kind are indicated.

The observed gauge curves at the observation points 1 at 1 m, 2 at 5 m and 3 at 10 m distance from the right edge were calculated with the values of 10^{-5} ms^{-1}, 5 d^{-1} and 0.2 for the three material parameters conductivity, transfer coefficient and storativity. They are shown in Fig. 2.9 for the first ten days of the simulation. The actual simulation time was 50 d where for each observation point 59 time steps have been recorded. Here to the transfer coefficients for inflow and outflow identical values were always assigned. The initial head was set to zero at all nodes. With growing distance from the river boundary, the maximum of the hydraulic head appears with a certain delay and the response to the floodwave becomes broader and weaker.

With PEST the conductivity, the transfer coefficient and the storativity have been estimated separately and in various combinations as indicated in Tab. 2.11. Note, that the stationary estimation problem (for a confined aquifer) is ill-posed since only a head boundary is prescribed. Now the conductivity is only defined up to an integration constant and cannot be estimated (Sun[13], Kaiser[11]). However, in a transient problem the conductivity alone can be estimated with a relative error of one percent (Tab. 2.11). In the estimation run for the transfer coefficient alone the point estimate exceeds the true value by more than ten percent. Moreover, the true value is not included in the 95 % CI of the point estimate. If the conductivity and the transfer coefficient are estimated together the accuracy of the point estimate for the conductivity remains unchanged. But for the transfer coefficient the relative error is reduced to three percent. When the conductivity and the storativity are estimated together, both point estimates fall signifi-

cantly below the true values. When all three material parameters are estimated the results become even worse. Obviously, for this combination of parameters there exists an issue with uniqueness.

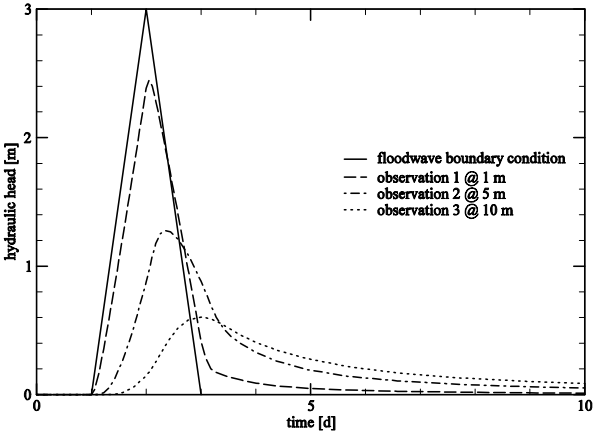

Figure 2.9 Hydraulic head curves at the right floodwave boundary and at the observation points 1, 2 and 3 with distances of 1 m, 5 m and 10 m.

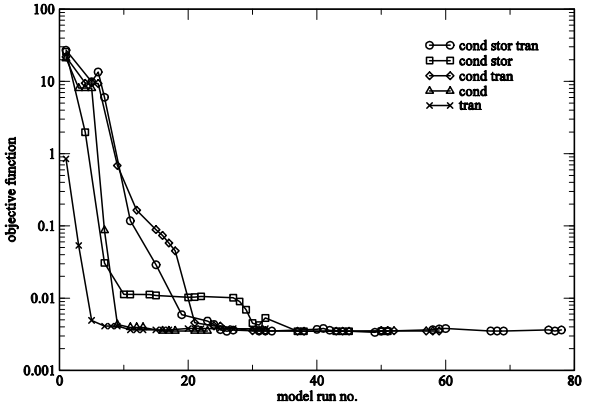

Figure 2.10 Objective functions for the PEST optimization runs to estimate the transfer coefficient alone (crosses), the conductivity alone (triangles), the transfer coefficient and conductivity together (diamonds), the conductivity and storativity together (squares), and all three parameters conductivity, storativity and transfer coefficient together (circles).

Table 2.11 Input parameter and parameter estimates of PEST in FEFLOW for the floodwave problem, 95 % CI in brackets

	Conductivity [10^{-5} m s^{-1}]	Transfer coefficient [d^{-1}]	Storativity [-]	Objective function [10^{-3} m^2]
input values	1.0	5.0	0.2	n.a.
parameter estimates				
conductivity	1.01 (1.00;1.02)	5.0 fixed	0.2 fixed	3.37
transfer coefficient	1.0 fixed	5.61 (5.55;5.66)	0.2 fixed	3.49
conductivity & transfer coefficient	1.01 (1.00;1.02)	5.16 (4.89;5.44)	0.2 fixed	3.48
conductivity & storativity	0.754 (0.737;0.771)	5.0 fixed	0.149 (0.147;0.151)	3.51
all 3 parameters	0.481 (0.467;0.496)	2.49 (2.25;2.75)	0.095 (0.092;0.098)	3.63

2.3 Concluding Remarks

The ability of the PEST software package to estimate material parameters of FEFLOW flow problems has been tested with four simple examples.

For Theis' analytical problem the transmissivity and the storage coefficient have been estimated with excellent precision.

In the Breyell pump test for a confined aquifer recorded drawdown data has been used to determine the transmissivity and the storage compressibility with various graphical evaluation methods based on Theis' analytical solution (Langguth and Voigt[12]). Owing to the simplification of the real hydrogeological setting, which produces unknown systematic errors, the predicted parameter values show a higher variability. This variability is reflected in the point estimates from both the PEST optimization process and the graphical evaluation methods in a similar way. The agreement of the estimated parameter values is better for the transmissivity than for the storage compressibility. Both estimation methods produced parameter estimates with sufficient accuracy.

The Wichita pump test has been conducted in an unconfined aquifer and has been evaluated by Langguth and Voigt[12] using the same approach as for an confined aquifer with and without corrected drawdown. With PEST it could be shown that the evaluation with the corrected drawdown produced a more accurate result. In this example the use of the graphical method has been pushed to the limit of applicability, whereas with PEST the Wichita pump test has been evaluated straight forwardly.

The numerical floodwave problem for the estimation of three material parameters showed that there was no unique set of parameters to reproduce the measured curves of the hydraulic head. Although the deviations from the true parameters are not excessive this example demonstrated that the estimation of material parameters with PEST does not automatically lead to reliable results.

References

1. Bouttier, F. and Courtier P. Data assimilation concepts and methods, Meteorological Training Course Lecture Series, *Lecture Notes of the European Centre for Meteorological Weather Forecast* (ECMWF), 2002.
2. Carslaw, H.S. and Jaeger, J.C. *Conduction of heat in solids*. 2nd ed. Oxford: University Press, 1959.
3. Cooper, H.H. and Jacob, C.E. A generalized graphical method for evaluating formation constants and summarizing well-field history. *Trans. Am. Geoph. Union* **27** (1946), 526-534.
4. Diersch, H.-J.G. Interactive, graphics-based finite-element simulation system FEFLOW for modeling groundwater flow, contaminant mass and heat transport processes. Release 5.2, *User's Manual*, WASY Ltd., Berlin, 2005.
5. Diersch, H.-J.G. Interactive, graphics-based finite-element simulation system FEFLOW for modeling groundwater flow, contaminant mass and heat transport processes. Release 5.2, *Reference Manual*, WASY Ltd., Berlin, 2005.
6. Doherty, J., Brebber, L. and Whyte, P. PEST - model independent parameter estimation, *User's Manual*, Watermark Computing, Corinda, Australia, 1994.
7. Dupuit J. *Etudes thèoriques et pratiques sur le mouvement des eaux dans les canaux dècouvertes et à travers les terrains permèables*. 2nd edition., Dunod, Paris, 1863.
8. Gründler R. *Interface manager - extensions and programming interface for FEFLOW*, WASY Ltd, Berlin, 2005.
9. Jacob, C.E. The recovery method for determining the coefficient of transmissibility. In: Bentall, R., Methods of determining permeability, transmissibility and drawdown, *Geol. Survey Water-Supply* Paper 1536-I, 283-292, 1963.
10. Jacob, C.E. Determining the permeability of water-table aquifers. In: Bentall, R., Methods of determining permeability, transmissibility and drawdown, *Geol. Survey Water-Supply* Paper 1536-I, 245-271, 1963.
11. Kaiser, J.C. Kopplung von FEFLOW mit dem Programm PEST zur Parameterkalibrierung (Coupling FEFLOW to the program PEST for parameter calibration). In: 3. Fachtagung '*Grafikgestützte Grundwassermodellierung*', Conference proceedings, WASY Ltd, Berlin, Germany, 51-65, 1998.
12. Langguth, H.-R. and Voigt, R. *Hydrogeologische Methoden*. in German, Springer, Berlin, 1980.
13. Sun, N.-Z. *Inverse problems in groundwater modeling*. Kluwer Academics Publishers, Dordrecht, 1994.
14. Theis C.V. The relation between lowering of the piezometric surface and the rate and duration of discharge of a well using groundwater storage. *Trans. Amer. Geophys. Union* **16** (1935), 519-524.

3 Benchmarking variable-density flow and transport in porous media containing an inclined fracture

H.-J. G. Diersch[a] **& F. Cornaton**[b]

[a]*WASY Institute for Water Resources Planning and Systems Research, Berlin, Germany*
[b]*Centre d'Hydrogéologie, Université de Neuchâtel, Switzerland*

3.1 Introduction

The physical basis, modeling strategies and numerical solutions of variable-density flow and transport processes in porous media are thoroughly described and discussed in the recent review papers by Diersch and Kolditz[2] as well as by Simmons *et al.*[8]. These papers are mainly focused on porous media, however, fractured media are not of specific concern. Indeed, there is a lack in studying density effects in fractured media, particularly in single fractures. Laboratory experiments in fractured media have not been carried out. Previous numerical investigations[7] were limited to a regular fracture network consisting of only vertical and horizontal fractures, embedded in a porous matrix. Shikaze *et al.*[7] have shown that density plumes in a fracture network may develop in a highly irregular fashion and are extremely difficult to predict. But, the growth of instabilities in single arbitrarily inclined fractures, located in a low-permeability porous matrix, remained open to be solved.

Recently, Graf and Therrien[5] have presented a numerical study on density-driven solute transport in single fractures of arbitrary inclination embedded in a low-permeable porous matrix. They simulated the problems by using the control volume finite element code FRAC3DVS[9] for 2D schematizations. Their results are well documented and appropriate for model testing. We shall benchmark the 45°-inclined fracture problem against FEFLOW and the research code Ground Water (GW) developed by F. Cornaton[1].

3.2 Variable-density Flow in a Porous Matrix with a 45°-Inclined Fracture

3.2.1 Statement of the 2D problem

The single fracture problem is shown in Fig. 3.1. The inclined fracture is discretized by 1D inclined pipe fracture elements. The left and right boundaries are assumed to be impermeable. The top and bottom boundaries are modeled as open boundaries with a constant hydraulic head h (set to zero). A contaminant source of constant concentration $C = C_s$ overlies groundwater of initial concentration $C = C_o$, where $C_o = 0.0 < C_s = 1.0$.

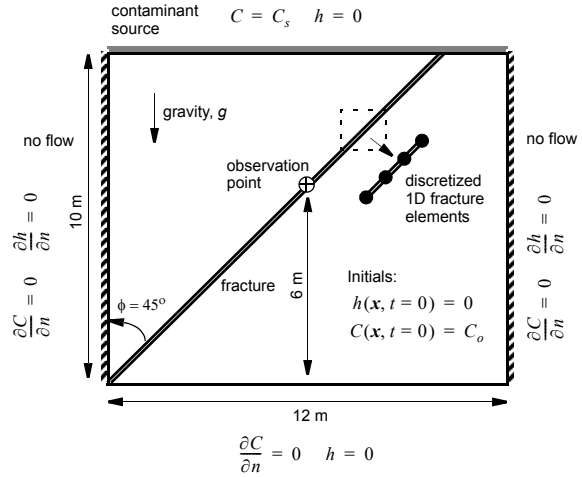

Figure 3.1 Single 45°-inclined fracture in a porous matrix; 2D geometry, boundary and initial conditions.

The simulations cover a time of 20 years. The model parameters are summarized in Table 3.1, where FEFLOW-specific symbolic[3,4] is used. It is assumed that the porous matrix is isotropic and that the entire aquifer is completely saturated. The parameters in FEFLOW units can be found in Table 3.2.

Graf and Therrien[5] tested different fracture slopes ϕ and mesh refinement levels ($l = 1, \ldots, 5$). The present study focusses on the 45°-inclined fracture problem at the highest grid level $l = 5$, consisting of 12,221 nodes and 24,000 triangles as shown in Fig. 3.2. We use two time stepping strategies: (1) in agreement to Graf and Therrien[5] a fully implicit time step marching scheme (combined with a Picard iteration) with a constant time step length of 0.2 yr, (2) alternatively, an adaptive predictor-corrector Adams-Bashforth/trapezoid rule (AB/TR) time stepping[2] with a RMS tolerance error of 10^{-4}. No upwinding is preferred in all simulations.

Table 3.1 Model parameters

Quantity[5]	Value
Width	12 m
Height	10 m
Simulation time	20 yr
Freshwater density, ρ_o	1000 kg m^{-3}
Maximum fluid density, $\rho(C_s)$	1200 kg m^{-3}
Fluid dynamic viscosity, μ_o	$3.545 \cdot 10^{4}$ kg m^{-1} yr^{-1}
Fluid compressibility, α_{fl}	$4.42 \cdot 10^{-25}$ kg^{-1} m yr^{2}
Matrix compressibility, α_m	$2.51 \cdot 10^{-24}$ kg^{-1} m yr^{2}
Gravitational acceleration, g	$9.75 \cdot 10^{15}$ m yr^{-2}
Tortuosity, τ	0.1
Matrix permeability, k	10^{-15} m^2
Matrix porosity, ε	0.35
Matrix longitudinal dispersivity, β_L	0.1 m
Matrix transverse dispersivity, β_T	0.005 m
Fracture dispersivity, β_L	0.1 m
Fracture aperture, b	50 μm
Free-solution molecular diffusion coefficient, D	0.15768 m^2 yr^{-1}

Table 3.2 FEFLOW parameters

Quantity	Value
Density ratio, α	0.2
Bulk compressibility, S_o	$1.743 \cdot 10^{-5}$ m^{-1}
Matrix conductivity, $K = (k\rho_o g)/\mu_o$	$8.7216 \cdot 10^{-9}$ $m\ s^{-1}$
Matrix porosity, ε	0.35
Matrix diffusion coefficient, D_d	$5 \cdot 10^{-10}$ $m^2\ s^{-1}$
Matrix longitudinal dispersivity, β_L	0.1 m
Matrix transverse dispersivity, β_T	0.005 m
Fracture dispersivity, β_L	0.1 m
Fracture area, bB	$5 \cdot 10^{-5}$ m^2
Fracture compressibility, S	$4.4 \cdot 10^{-6}$ m^{-1}
Hydraulic aperture, b_{corr} a)	$5.374 \cdot 10^{-5}$ m
Fracture diffusion coefficient, D	$5 \cdot 10^{-9}$ $m^2\ s^{-1}$

a) Aperture b has to be corrected by the factor $\sqrt{f/f_o} = 1.0747952$ due to a different viscosity magnitude, where $f = \rho g/\mu$ and $f_o = \rho_o g/\mu_o = 7.55 \cdot 10^6\ m^{-1} s^{-1}$, see Appendix D in[4].

The inclined fracture is modeled by 100 1D pipe fracture elements fitted to the edges of the corresponding triangular elements (Fig. 3.3). For the flow in the fracture the Hagen-Poiseuille law is applied. Fluid viscosity is considered independent of the concentration $\mu = \mu_o = \text{const}$.

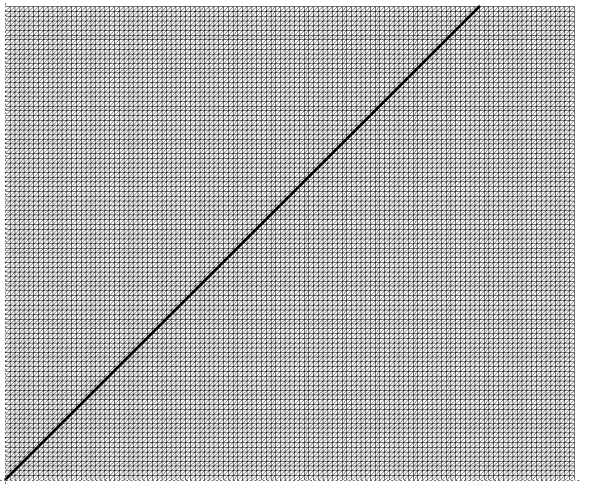

Figure 3.2 2D triangular finite element mesh with 1D pipe fracture elements used for FEFLOW and GW[1] simulations.

3.2.2 Governing equations

The porous medium and fracture flow are transient. Accordingly, the conservation of mass and momentum can be described by the following equations (symbols are summarized below under Notation):

$$\bar{S}\frac{\partial h}{\partial t} + \nabla \cdot \boldsymbol{q} = Q_{\text{EOB}} \tag{3-1}$$

$$\boldsymbol{q} = -\bar{\boldsymbol{K}}(\nabla h + \alpha C^* \boldsymbol{e}) \tag{3-2}$$

with

$$\bar{S} = \begin{cases} S_o & \text{bulk compressibility in the porous matrix} \\ S & \text{compressibility in the fracture} \end{cases} \tag{3-3}$$

and

$$\overline{\boldsymbol{K}} = \begin{cases} \left(K = \dfrac{k\rho_o g}{\mu_o}\right)\boldsymbol{I} & \text{Darcy law in the porous matrix} \\ \dfrac{b_{\text{corr}}^2 \rho_o g}{12\mu_o}\boldsymbol{I} & \text{Hagen-Poiseuille law in the fracture} \end{cases} \tag{3-4}$$

where

$$C^* = \frac{C - C_o}{C_s - C_o} \tag{3-5}$$

corresponds to a normalized solute concentration. Note that in (3-1) the term of Extended Oberbeck-Boussinesq (EOB) approximation Q_{EOB} is included, which is defined as

$$Q_{\text{EOB}} = -\alpha\left(\bar{\varepsilon}\frac{\partial C^*}{\partial t} + \boldsymbol{q}\cdot\nabla C^*\right) \tag{3-6}$$

If the standard Oberbeck-Boussinesq (OB) approximation[2] is applied, which is in agreement to the assumptions done by Graf and Therrien[5] , we have to solve with $Q_{\text{EOB}} \approx 0$.

The solute transport of a conservative tracer in the porous matrix and the fracture is governed by the convection-dispersion equation (solute mass balance) in the following form:

$$\bar{\varepsilon}\frac{\partial C}{\partial t} + \boldsymbol{q}\cdot\nabla C - \nabla\cdot(\boldsymbol{D}\cdot\nabla C) + Q_{\text{EOB}}C = 0 \tag{3-7}$$

with the tensor of hydrodynamic dispersion

$$\boldsymbol{D} = \begin{cases} (\varepsilon D_d + \beta_T\|q\|)\boldsymbol{I} + (\beta_L - \beta_T)\dfrac{\boldsymbol{q}\otimes\boldsymbol{q}}{\|\boldsymbol{q}\|} & \text{porous matrix} \\ D\boldsymbol{I} + \beta_L\dfrac{\boldsymbol{q}\otimes\boldsymbol{q}}{\|\boldsymbol{q}\|} & \text{fracture} \end{cases} \tag{3-8}$$

where

$$\boldsymbol{q} = \bar{\varepsilon}\boldsymbol{v} \tag{3-9}$$

and

$$\bar{\varepsilon} = \begin{cases} \varepsilon & \text{porous matrix} \\ 1 & \text{fracture} \end{cases} \tag{3-10}$$

Note that the term $Q_{\text{EOB}}C$ in the solute transport equation (3-7) is commonly negligible[6] even in the case of using the EOB approximation Q_{EOB} in the flow equation (3-1).

3.2.3 Simulation results

For the 45°-inclined fracture problem the results obtained by Graf and Therrien[5] and by FEFLOW in form of computed concentration distributions as well as velocity fields and pathline patterns at 2, 4 and 10 yr simulation time are shown in Fig. 3.3. It reveals how the solutes migrate from the fracture into the adjoining porous matrix mainly governed by hydrodynamic dispersion and to a small degree by convection.

As a typical feature of the problem two convection cells form above and below the fracture with increasing extent in time. Both cells move downward in time. Note that the cell above the fracture moves faster downward than the lower cell. Both convection cells remain separated by the high-conductive fracture, therefore, acts as a barrier to convection.

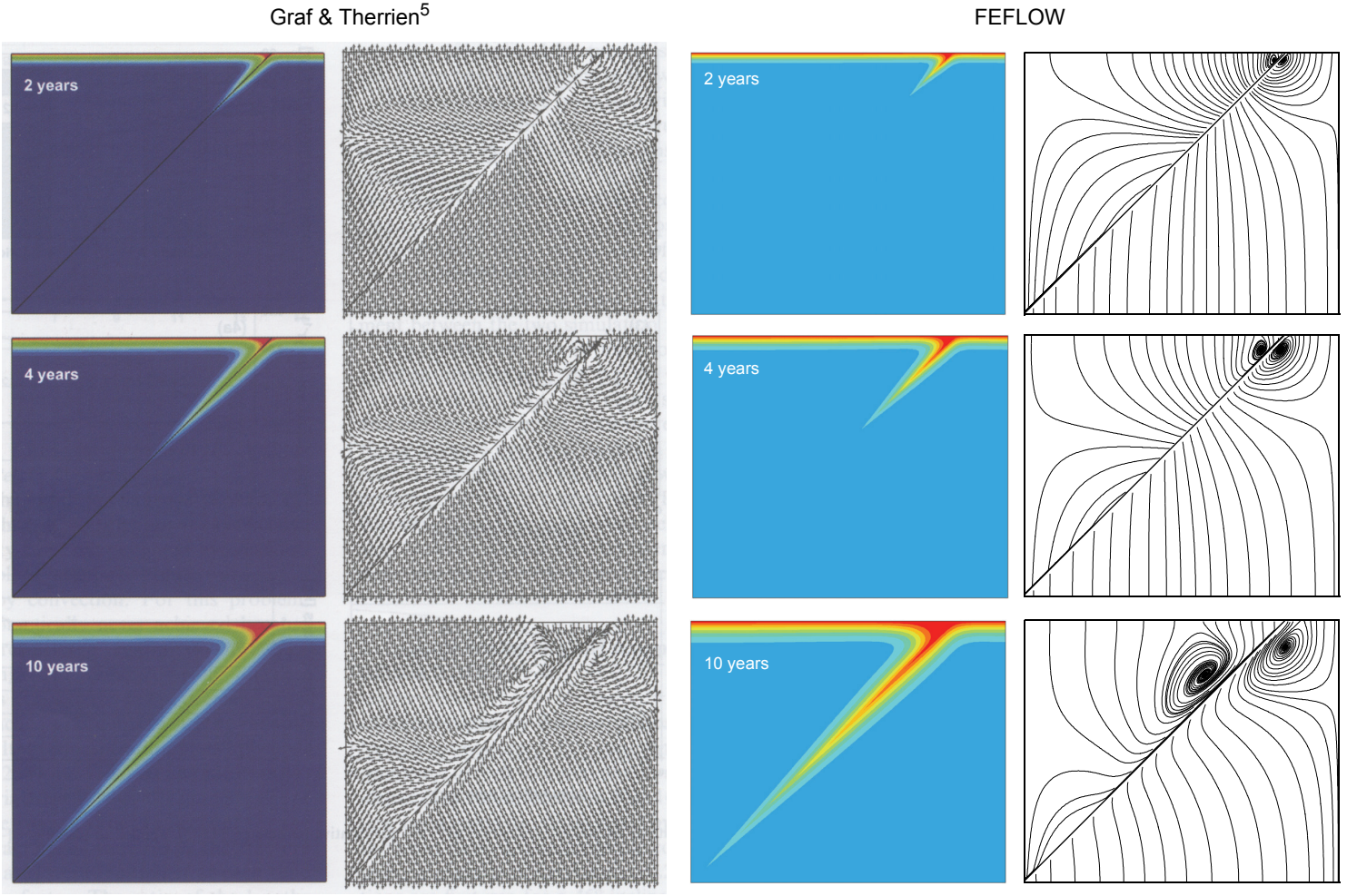

Figure 3.3 Computed concentration distributions and velocity/pathline field after 2, 4 and 10 yr simulation. Comparison of FEFLOW results obtained by an AB/TR time stepping (right) to findings by Graf and Therrien[5] modeled by a fully implicit constant time stepping (left). OB approximation is used.

At a first glance, FEFLOW and FRAC3DVS agree very well. However, as already seen in Fig. 3.3 the advance of solute transport in the fracture seems slightly faster at early times in the FRAC3DVS predictions compared to the FEFLOW results. Indeed, this can be confirmed if evaluating precisely the breakthrough curves of solute at the observation point as shown in Fig. 3.4. While the FEFLOW curves for adaptive time stepping (taking 236 steps) and for constant time steps (100 implicit steps with each of 0.2 yr length) provide reasonably close solutions, Graf and Therrien's breakthrough curve is apparently advanced at early times. Due to the high velocity contrasts between matrix and fracture, the influence of early times on the spreading of solute in the depth is crucial and requires further model comparisons.

The problem was also simulated by using the GW finite-element simulator[1]. The GW results provide a nearly perfect agreement with the FEFLOW predictions (conf. Figs. 3.4, 3.5 and 3.6). As evidenced in Fig. 3.4 FEFLOW's and GW's breakthrough curves are very close. This could be confirmed by using both adaptive and constant time stepping strategies. Note further that the type of solving the resulting sparse equation systems did not influence the outcome. Direct and iterative equation solvers were tested in FEFLOW. Additionally, the Extended Boussinesq approximation (EOB)[2] is also performed. As indicated in Fig. 3.7 the breakthrough curve for the EOB is slightly shifted in advance compared to FEFLOW's OB solution, however, remains further behind Graf and Therrien's OB solution.

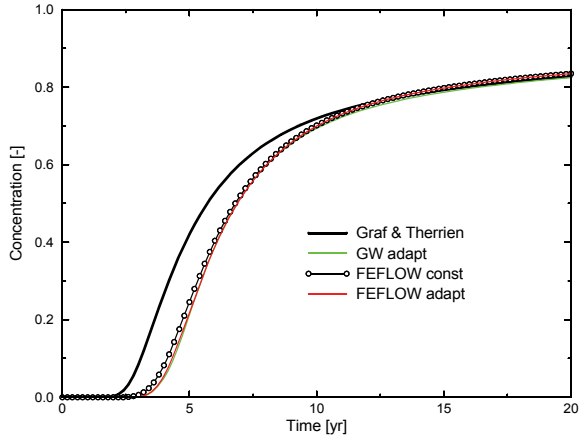

Figure 3.4 Breakthrough curves at the observation point. Comparison of Graf & Therrien's results[5] to GW[1] (with adaptive time stepping) and FEFLOW (with constant and adaptive time stepping) in using OB approximation.

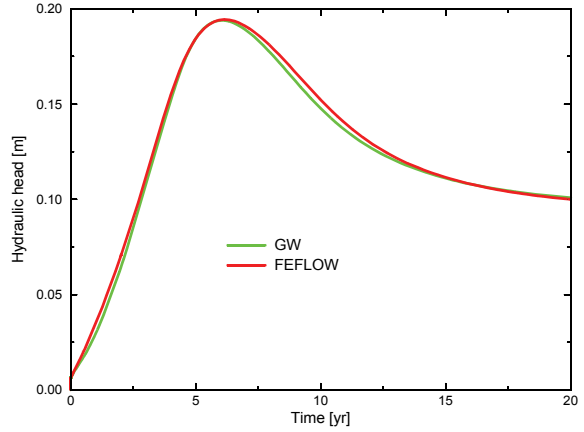

Figure 3.5 History of hydraulic head *h* at the observation point. FEFLOW *versus* GW[1] results (adaptive time stepping) in using OB approximation.

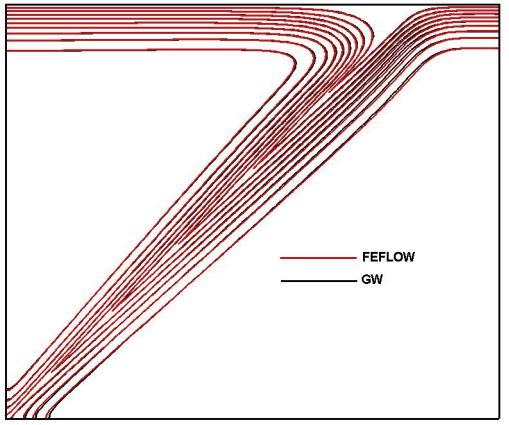

Figure 3.6 Computed solute concentration contours at 15 yr: FEFLOW *versus* GW[1] results in using OB approximation.

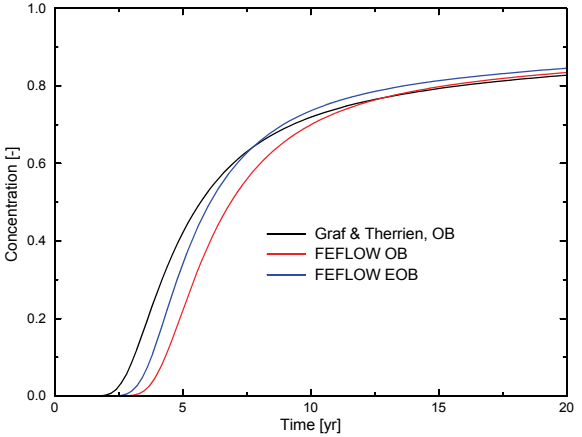

Figure 3.7 Breakthrough curves at the observation point. Comparison between OB approximation and EOB approximation. Adaptive time stepping is used for FEFLOW's solutions.

3.3 Summary and Conclusions

The 45°-inclined fracture benchmark problem firstly proposed and simulated in Graf and Therrien[5] by using FRAC3DVS[9] has been recomputed by using FEFLOW and, additionally, by the research code GW[1]. The major outcome of the comparison analysis is the following:

- In principle, Graf and Therrien's results[5] could be confirmed.
- There is a nearly perfect agreement between FEFLOW and GW solutions.
- FRAC3DVS produces a clearly advanced solute breakthrough in the fractures at early times compared to the FEFLOW and GW simulations.

It has been found that the discrepancies between FRAC3DVS and FEFLOW or GW are not attributed to different time stepping strategies, Boussinesq approximations and different sparse matrix solvers. Furthermore, more spatially refined meshes did not change notably anymore the solutions because the mesh convergence is practically achieved at the analyzed mesh refinement level.

3.4 Notation

Roman letters

B	L	thickness;
b	L	aperture of fracture;
b_{corr}	L	$= b\sqrt{f/f_o}$, corrected aperture of fracture;

C	ML^{-3}	solute concentration;
C^*	1	normalized solute concentration;
C_o	ML^{-3}	initial or reference solute concentration;
C_s	ML^{-3}	maximum or boundary solute concentration;
$\boldsymbol{D}$	L^2T^{-1}	tensor of hydrodynamic dispersion;
D	L^2T^{-1}	free-solution molecular diffusion coefficient;
D_d	L^2T^{-1}	$= \tau D$, medium molecular diffusion;
$\boldsymbol{e}$	1	$= -\boldsymbol{g}/\|\boldsymbol{g}\|$, gravitational unit vector;
f	$L^{-1}T^{-1}$	$= \rho g/\mu$, relation factor;
f_o	$L^{-1}T^{-1}$	$= \rho_o g/\mu_o$, reference relation factor;
$\boldsymbol{g}$	LT^{-2}	gravity vector;
g	LT^{-2}	$= \|\boldsymbol{g}\|$, gravitational acceleration;
h	L	hydraulic head;
$\boldsymbol{I}$	1	unit (identity) tensor;
$\overline{\boldsymbol{K}}$	LT^{-1}	generalized hydraulic conductivity tensor;
K	LT^{-1}	hydraulic conductivity;
k	L^2	permeability of porous medium;
l		mesh refinement level, $l = 1, \ldots$;
Q_{EOB}	T^{-1}	extended Oberbeck-Boussinesq approximation term;
$\boldsymbol{q}$	LT^{-1}	specific flux vector;
S	L^{-1}	$= \alpha_{\mathrm{fl}}\rho_o g$, fluid compressibility;
S_o	L^{-1}	$= [\varepsilon\alpha_{\mathrm{fl}} + (1-\varepsilon)\alpha_{\mathrm{m}}]\rho_o g$, bulk compressibility;
$\overline{S}$	L^{-1}	generalized compressibility:
$\boldsymbol{v}$	LT^{-1}	fluid velocity vector;

Greek letters

α	1	$= (\rho(C_s) - \rho_o)/\rho_o$, density ratio;
α_{fl}	$M^{-1}LT^2$	fluid compressibility coefficient;
α_{m}	$M^{-1}LT^2$	matrix compressibility coefficient;
β_L, β_T	L	longitudinal and transverse dispersivity, respectively;
ε	1	porosity of porous matrix;
$\bar{\varepsilon}$	1	generalized void space;
ρ	ML^{-3}	fluid density;
ρ_o	ML^{-3}	$= \rho(C_o)$, reference fluid density;
μ	$ML^{-1}T^{-1}$	dynamic viscosity of fluid;
μ_o	$ML^{-1}T^{-1}$	$= \mu(C_o)$, reference dynamic viscosity of fluid;
τ	1	tortuosity of porous medium;
ϕ	°	fracture slope angle;

Abbreviations

1D	one-dimensional;
2D	two-dimensional;
EOB	extended Oberbeck-Boussinesq approximation;
OB	Oberbeck-Boussinesq approximation;
RMS	root-mean square;

References

1. Cornaton, F. Ground Water - a 3-D ground water flow and transport finite element simulator. Centre for Hydrogeology, University of Neuchâtel, Neuchâtel, Switzerland, 2006.
2. Diersch, H.-J.G. and Kolditz, O. Variable-density flow and transport in porous media: approaches and challenges. *Adv. Water*

Resour. **25** (2002), 899-944. (also published in FEFLOW White Papers Vol. II, Chapter 1, pp. 5-101).

3. Diersch, H.-J.G. FEFLOW *Reference manual*, WASY Ltd. 2002, Berlin.
4. Diersch, H.-J.G. Discrete feature modeling of flow, mass and heat transport processes by using FEFLOW. *FEFLOW White Papers Vol. I*, Chapter 9, WASY Ltd. 2005, Berlin, pp. 149-195.
5. Graf, T. and Therrien, R. Variable-density groundwater flow and solute transport in porous media containing nonuniform discrete fractures. *Adv. Water Resour.* **28** (2005), 1351-1367.
6. Kolditz, O., Ratke, R., Diersch, H.-J.G. and Zielke, W. Coupled groundwater flow and transport: 1. Verification of variable-density flow and transport models. *Adv. Water Resour.* **21** (1998), 27-46.
7. Shikaze, S.G., Sudicky, E.A. and Schwartz, F.W. Density-dependent solute transport in discretely-fractured geologic media: is prediction possible? *J. Contaminant Hydrol.* **34** (1998)10, 273-291.
8. Simmons, C.T, Fenstemaker, T.R. and Sharp Jr, J.M. Variable-density groundwater flow and solute transport in heterogeneous porous media: approaches, resolutions and future challenges. *J. Contaminant Hydrol.* **52** (2001)11, 245-275.
9. Therrien, R. and Sudicky, E.A. Three-dimensional analysis of variably saturated flow and solute transport in discretely-fractured porous media. *J. Contaminant Hydrol.* **23** (1996), 1-44.

3. Benchmarking variable-density flow and transport in porous media containing an inclined fracture

Numerical simulation of variable-density multi-diffusive fingering convection phenomena

4

H.-J. G. Diersch & V. Clausnitzer

WASY Institute for Water Resources Planning and Systems Research, Berlin, Germany

4.1 Introduction

Fingering instabilities can play an important role in the spreading of heavy leachates with or without temperature influences. Density-driven convection processes in the subsurface are of growing concern in relation to contamination and geothermal problems. There is both a theoretical and a practical need to model variable-density flow, multispecies mass and heat transport phenomena with multiple buoyancy and multidiffusive effects (see Diersch and Kolditz[5]).

A striking feature of such processes is that convection can occur in initially density-stable configurations containing two or more components (solutal species, heat) with diffusivities that make opposing contributions to vertical density gradients. A basic requirement is in diffusivities differences of the components which can result in buoyant instabilities capable of initiating convection. The initial distribution and concentration of each species (or temperature of heat) strongly influence such type of convective pattern. Consider the situation where two solutions are layered with the denser solution on bottom, we can differ in two principal cases: (1) If the slower diffusing species is on top, a parcel of fluid perturbed downward across the interface of the two species takes on mass from the surrounding faster diffusing species so that the parcel continues to fall. Likewise, parcels of fluid perturbed upward continue to rise. This mode of convection is termed *double-diffusive finger convection* (DDFC) or multispecies finger convection and is characterized by patterns driven by long, narrow columns (fingers) of rising and falling fluid. (2) Alternatively, if the species with the higher diffusivity is on top, a parcel of fluid perturbed downward across the interface diffuses mass outward to the surrounding fluid more rapidly than it gains mass from the lower-diffusivity species. The parcel of fluid then becomes less dense than the surrounding fluid, moves upward, and overshoots its original position before repeating the motion. This mode of convection is termed oscillatory double-diffusive convection and can lead to well-mixed convecting layers separated by sharp contrasts in fluid density (e.g., forming staircase-type patterns[5]).

In reality, convective fingers can also be created as a result of a difference in diffusivities between heat and solute, which as been firstly detected in oceans. In this

case double-diffusive finger convection is termed *thermohaline convection*. While thermohaline convection is responsible on large-scale circulation in oceans, it has also been recognized that subsurface environments (porous media and fractures) are favorable to DDFC. It can be important at deep circulation in marine and terrestrial alluvial basins, for interaction of groundwater and surface water, and in transport of dissolved solutes from solid waste landfills.

DDFC processes were studied by Cooper *et al.*[2] and Pringle *et al.*[9] via Hele-Shaw experiments using a light transmission technique that provides high-resolution concentration fields. From a near perturbation-free initial layering of a lighter sucrose solution over a dense salt solution, upward and downward moving fingers quickly form at the interface between the two solutions. Particularly, the recent experimental data obtained by Pringle *et al.*[9] provide a suited baseline for use in the development and evaluation of numerical models.

Numerical models must play an increasing role in a better understanding of DDFC phenomena in porous media. As already argued by Cooper *et al.*[2] a limitation in finger growth due to large-scale circulation controlled by inertial forces as observed in ordinary fluids (nonporous media) does not seem to exist in porous systems characterized by low Reynolds numbers. An intriguing possibility is that the merging and subsequent formation of conduits along which fingers travel could be repeated at larger and larger scales. Cooper *et al.*[2] concluded that larger and greater-spaced conduits for mass transport may naturally evolve in porous media, leading to growth bounded on a much larger scale than has been observed in any laboratory experiments.

Recently, the Hele-Shaw experiments collected by Pringle *et al.*[9] were successfully simulated by Hughes *et al.*[7] using a modified version of the SUTRA code (Voss and Provost[11], Hughes and Sanford[6]) that combines Galerkin finite-element and integrated finite-difference techniques. Their modeling results have prompted our own numerical experiments based on the commercial finite-element simulator FEFLOW.

The data set of Pringle *et al.*[9] is well-suited for code verification of DDFC numerical models because, unlike most previous experimental Hele-Shaw data sets, it is of sufficient spatial and temporal resolution to allow accurate comparisons of simulated and measured convective fingering. In addition, computational high-resolution results obtained by different numerical approaches and full-field images from the experimental data set allow qualitative comparison of the evolving flow field and quantitative comparison of mass transfer rates.

4.2 Basic Equations

Following the experimental and numerical studies by Pringle *et al.*[9] and Hughes *et al.*[7], respectively, the focus is on DDFC phenomena with solutes. Accordingly, variable-density multispecies convection processes involving multiple buoyancy and multidiffusive effects require the solution of the following coupled equation system for fluid mass conservation, Darcy law, and mass balance assuming isothermal, nonreactive, and fully saturated conditions:

$$\left.\begin{aligned} S\frac{\partial h}{\partial t} + \nabla \cdot \boldsymbol{q} &= Q + Q_{\mathrm{EOB}} \\ \boldsymbol{q} &= -\boldsymbol{K} f_{\mu}\left(\nabla h - \frac{\rho - \rho_o}{\rho_o}\boldsymbol{e}\right) \\ \frac{\partial}{\partial t}(\varepsilon C_k) + \nabla \cdot (\boldsymbol{q} C_k) - \nabla \cdot (\boldsymbol{D}_k \cdot \nabla C_k) &= R_k \qquad (k = 1, \ldots, \mathrm{N}) \end{aligned}\right\} \tag{4-1}$$

with the constitutive relationships

$$\left.\begin{aligned} \rho &= \rho_0\left[1 + \sum_k \frac{\alpha_k}{(C_{ks} - C_{k0})}(C_k - C_{k0})\right] \qquad f_{\mu} = \frac{\mu_o}{\mu(C_k)} \approx \frac{\mu_o}{\mu_o + \sum_k \vartheta_k (C_k - C_{k0})} \\ \boldsymbol{D}_k &= (\varepsilon D_k^d + \beta_T \|\boldsymbol{q}\|)\boldsymbol{I} + (\beta_L - \beta_T)\frac{\boldsymbol{q} \otimes \boldsymbol{q}}{\|\boldsymbol{q}\|} \qquad Q_{\mathrm{EOB}} = -\boldsymbol{q} \cdot \left(\sum_k \alpha_k \nabla C_k\right) - \varepsilon\left(\sum_k \alpha_k \frac{\partial C_k}{\partial t}\right) \end{aligned}\right\} \tag{4-2}$$

where h denotes hydraulic head, $\boldsymbol{q}$ the Darcy flux vector, C_k solute concentration of species k (with N as the maximum number of species), C_{ks} is the maximum concentration and C_{k0} is the reference concentration of species k, respectively, S the storage coefficient due to fluid and skeleton compressibility, Q the sink/source term, Q_{EOB} the Extended Oberbeck-Boussinesq term, ρ the fluid density, $\boldsymbol{K}$ the tensor of hydraulic conductivity, μ the dynamic fluid viscosity, f_{μ} the viscosity relation function, $\boldsymbol{e}$ the gravitational unit vector, ε the porosity, $\boldsymbol{D}_k$ the tensor of hydrodynamic dispersion of species k (assuming Fickian-based dispersive mass flux), R_k the reaction term, α_k the density difference ratios (as dimensionless concentration expansion coefficients), ϑ_k the coefficients of fluid viscosity change, D_k^d the coefficients of molecular diffusivity of species k, β_L, β_T the longitudinal and transverse dispersivities, respectively, t the time, and $\boldsymbol{I}$ the unit tensor. Subscript 0 identifies reference values.

4.3 Finger Model Problem

Pringle *et al.*[9] used a Hele-Shaw cell to study the temporal and spatial distribution of DDFC phenomena of two solutes initially in a density-stable configuration with a mean interface thickness of about $1 \cdot 10^{-3}$ m. The Hele-Shaw cell was filled with a sucrose solution over a denser sodium chloride solution (NaCl). The 2D domain measures 0.2541 m (cell length L) by 0.1625 m (cell height H), see Fig. 4.1. The Hele-Shaw cell is inclined at an angle of 25° relative to horizontal. To visualize sodium chloride concentrations and quantify convective motion, a dye tracer with a low concentra-

tion was mixed with the sodium chloride. The dye had a negligible effect on fluid density. Accordingly, three species ($N = 3$) have to be considered: sucrose ($k = s$), sodium chloride ($k = c$), and dye ($k = \text{dye}$). The used parameters are summarized in Table 4.1. Note that NaCl concentrations are not mapped perfectly by the dye tracer because the diffusivity of sodium chloride is approximately 2.5 times greater than the diffusivity of the dye (Table 4.1). Because the motion is convective through most of the experiment, Pringle *et al.*[9] suggested the diffusivity differences had little impact on the mapping of sodium chloride concentrations over the length of time of the experiment.

The parameters in Table 4.1 are related to the dimensionless Rayleigh numbers Ra_k ($k = s, c$), Lewis number Le and Turner number R_ρ as given in Table 4.2, where $Ra_c = Ra_s\, Le\, R_\rho$. The Le number is defined with the smaller diffusivity in the numerator such that $0 < Le < 1$.

To maintain the full physical equivalence to the experimental and numerical studies done by Pringle *et al.*[9] and Hughes *et al.*[7] the most important physical quantities characterizing the DDC fingering problem are the Turner number R_ρ given by 1.22, the Lewis number Le according to 0.3303 and one Rayleigh number given for sodium chloride as $Ra_c = 26{,}460$. The remaining quantities can be directly derived from these characteristic numbers. Note that by using the dimensionless density difference ratios α_k in the fluid density ρ of (4-2), the density expansion becomes independent of the real values of species concentrations and the maximum concentrations C_{ks} can be arbitrarily chosen. In agreement to the physical experiment C_{ks} and C_{k0} are chosen as listed in Table 4.3

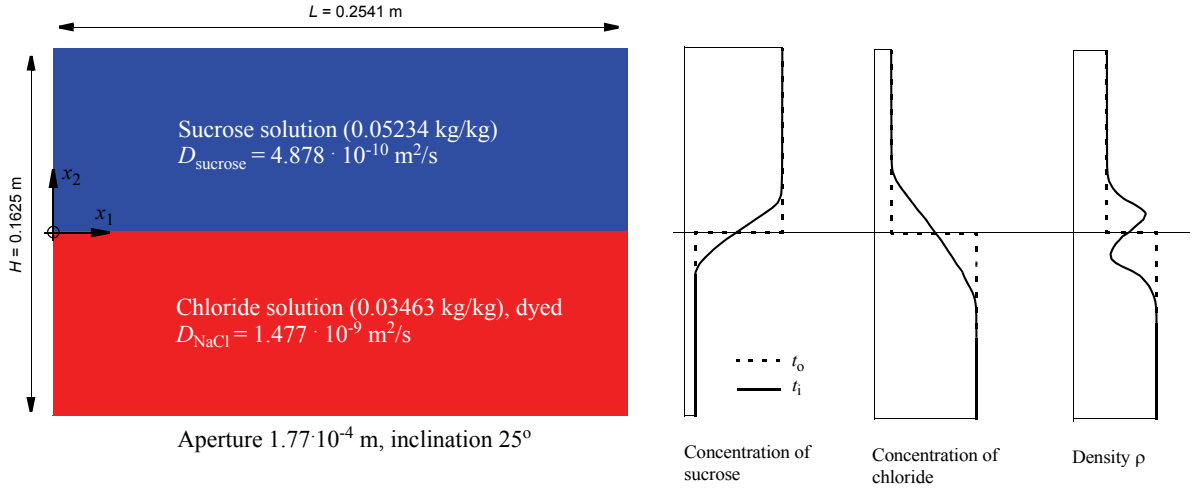

Figure 4.1 Hele-Shaw study experiment by Pringle *et al.*[9].

Table 4.1 Parameters of the three-species finger model problem

Parameter	Value	Unit
hydraulic conductivity, $K = k\rho_o(g\sin 25°)/\mu_o$	$1.07838 \cdot 10^{-2}$	$m\ s^{-1}$
intrinsic permeability, k	$2.61 \cdot 10^{-9}$	m^2
reference density, ρ_o	998.0	$kg\ m^{-3}$
reference viscosity, μ_o	10^{-3}	$kg\ m^{-1}s^{-1}$
storativity, S	0.0	m^{-1}
sucrose density expansion, α_s	0.0182787	$kg\ kg^{-1}$
chloride density expansion, α_c	0.022302	$kg\ kg^{-1}$
dye density expansion, α_{dye}	0.0	$kg\ kg^{-1}$
sucrose diffusivity, D_s^d	$4.878 \cdot 10^{-10}$	$m^2\ s^{-1}$
chloride diffusivity, D_c^d	$1.477 \cdot 10^{-9}$	$m^2\ s^{-1}$
dye diffusivity, D_{dye}^d	$5.670 \cdot 10^{-10}$	$m^2\ s^{-1}$
porosity, ε	1.0	m^3m^{-3}
dispersivity, β_L, β_T	0.0	m
viscosity change to sucrose, ϑ_s	$2.75 \cdot 10^{-3}$	m^2s^{-1}
viscosity change to chloride, ϑ_c	$1.59 \cdot 10^{-3}$	m^2s^{-1}
viscosity change to dye, ϑ_{dye}	0.0	m^2s^{-1}

Table 4.2 Rayleigh, Lewis and Turner numbers

Number	Value
sucrose Rayleigh number, $Ra_s = \frac{\alpha_s KH}{\varepsilon D_s^d}$	65,664
chloride Rayleigh number, $Ra_c = \frac{\alpha_c KH}{\varepsilon D_c^d}$	26,460
Lewis number, $Le = D_s^d/D_c^d$	0.3303
Turner number, $R_\rho = \frac{\alpha_c}{\alpha_s}$	1.22

Table 4.3 Maximum and reference concentrations

Number	Value	Unit
sucrose concentration, C_{ss}	52.34	$kg\ m^{-3}$
chloride concentration, C_{cs}	34.63	$kg\ m^{-3}$
dye concentration, C_{dyes}	0.25	$kg\ m^{-3}$
reference concentrations, C_{k0} $(k = s, c, \text{dye})$	0.0	$kg\ m^{-3}$

It has been shown in stability analysis[8] and Hele-Shaw experiments[1] as the Turner number R_ρ decreases from the stability boundary at Le^{-1}, the system transitions from being diffusion-dominated to convection-dominated. The corresponding stability and instability domains in the Rayleigh parameter space are shown in Fig. 4.2. The current situation with a Turner number of 1.22 is clearly located in the DDFC domain with increasing mass fluxes and finger velocities. DDFC exists in the range $1 < R_\rho < Le^{-1}$. For $R_\rho < 1$ there is no more an initially density-stable stratification of the solutes and the system becomes gravitationally instable.

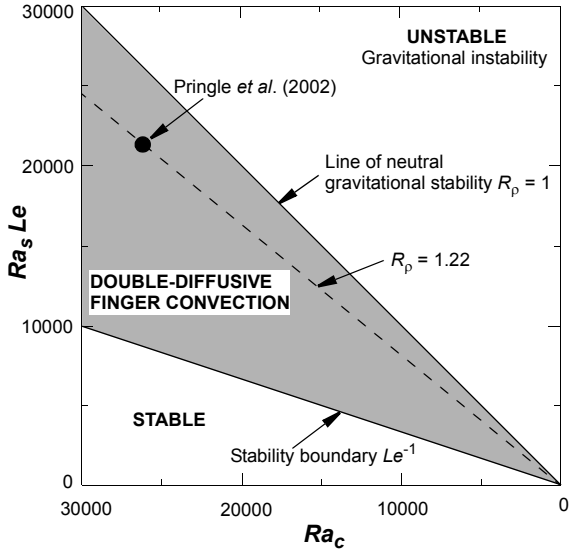

Figure 4.2 Stability and instability domains in the Rayleigh parameter space with the location of the current double-diffusive finger problem at $R_\rho = 1.22$.

In the 16-hour Hele-Shaw experiments done by Pringle *et al.*[9] a total of 300 images of the evolving concentration field were collected. A sequence of dye concentrations from the experiment is shown in Fig. 4.3. Time is presented as dimensionless ($t^* = tD_c^d/H^2$). The measured time stages (t and t^*) are listed in Table 4.4.

Table 4.4 Measured time stages

Stages		t^* [-]	t [sec]	t [hr]
a	*Early* stage	$4.03 \cdot 10^{-5}$	720.5	0.20
b	*Mature* stage: vertical growth of fingers	$1.31 \cdot 10^{-4}$	2342.1	0.65
c		$2.21 \cdot 10^{-4}$	3951.1	1.10
d		$3.22 \cdot 10^{-4}$	5756.8	1.60
e	Fingers reach top and bottom boundaries	$4.23 \cdot 10^{-4}$	7562.5	2.10
f		$5.24 \cdot 10^{-4}$	9368.2	2.60
g	*Roundown* stage	$6.04 \cdot 10^{-4}$	10798.5	3.00
h		$7.25 \cdot 10^{-4}$	12961.8	3.60
i		$7.85 \cdot 10^{-4}$	14034.5	3.90
j		$1.03 \cdot 10^{-3}$	18414.7	5.12
k		$1.77 \cdot 10^{-3}$	31644.6	8.79
l		$3.17 \cdot 10^{-3}$	56674.2	15.7

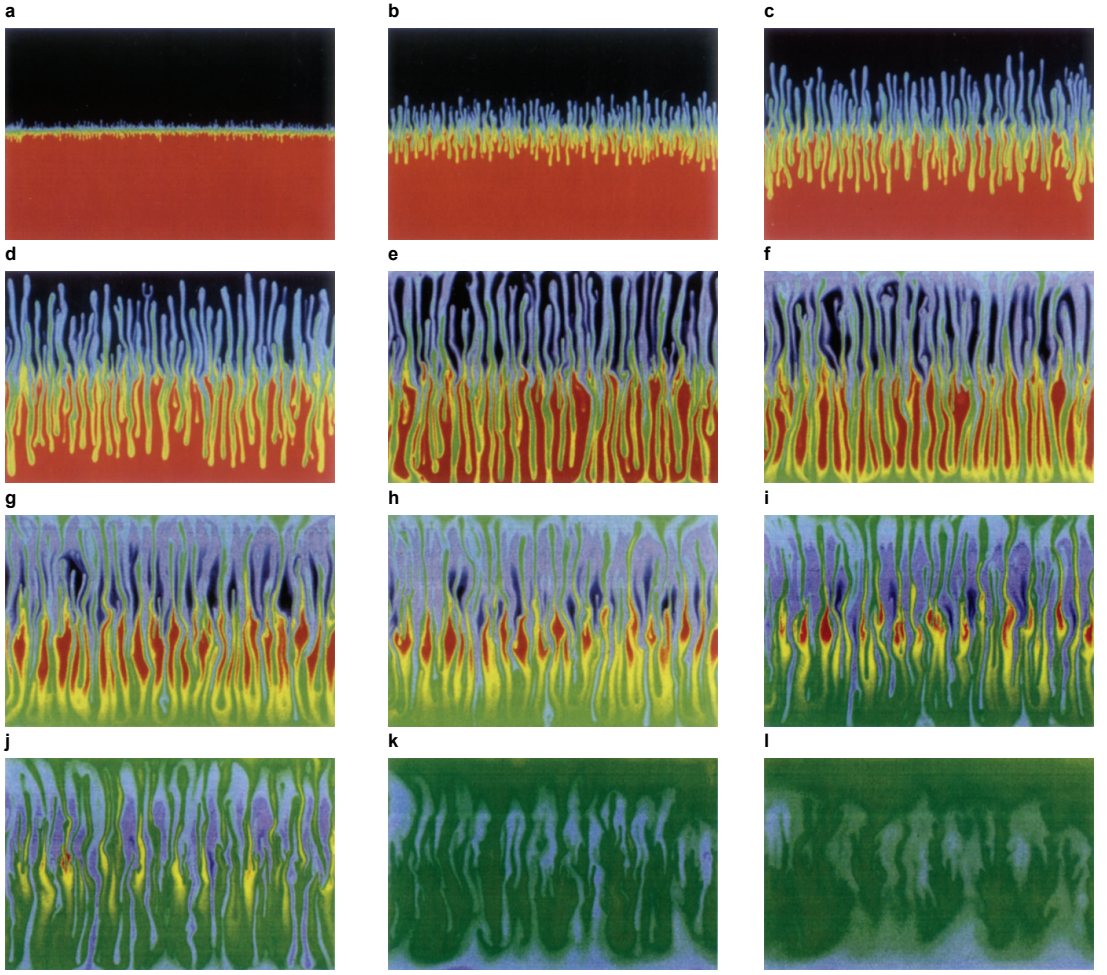

Figure 4.3 Hele-Shaw observation results from Pringle *et al.*[9] for the dye component at (a) $t^* = 4.03 \cdot 10^{-5}$, (b) $t^* = 1.31 \cdot 10^{-4}$, (c) $t^* = 2.21 \cdot 10^{-4}$, (d) $t^* = 3.22 \cdot 10^{-4}$, (e) $t^* = 4.23 \cdot 10^{-4}$, (f) $t^* = 5.24 \cdot 10^{-4}$, (g) $t^* = 6.04 \cdot 10^{-4}$, (h) $t^* = 7.25 \cdot 10^{-4}$, (i) $t^* = 7.85 \cdot 10^{-4}$, (j) $t^* = 1.03 \cdot 10^{-3}$, (k) $t^* = 1.77 \cdot 10^{-3}$, and (l) $t^* = 3.17 \cdot 10^{-3}$. ($t^* = tD_c^d / H^2$ dimensionless time). Color sequence black-blue-green-yellow-orange-red depicts normalized dye concentration from 0 to 1.

As seen in a sequence of concentration fields in Fig. 4.3 there are interesting features in the behavior of the DDC system. Due to the initially perturbed solution interface an array of distinct fingers rapidly grow in unison at the early time stage (Fig. 4.3a,b). These fingers begin to interact with one another causing a reorganization of the initial uniform finger structure (Fig. 4.3c,d). A typical feature at this stage is a large number of very small fingers with a wide variation in vertical extent. As convection proceeds, small-scale fingers continuously emerge from the region of the initial solution interface referred to as the *finger generation zone* by Cooper *et al.*[2]. These newly generated fingers add to the structural intricacy of the field by growing, and in many cases, merging with, and convecting up through the stems of early formed neighbors. The generation of new finger pairs as the tips of some upward and downward growing fingers can also be observed (Fig. 4.3c-f). At $t^* = 4.23 \cdot 10^{-4}$ (Fig. 4.3e), the fastest growing fingers reach the top and bottom boundaries of the cell and begin to spread laterally forming more dense (at the bottom) and less dense (at the top) 'clouds' of fluid (Fig. 4.3f-h). Within the finger generation zone, far from the boundaries, new fingers continue to form from isolated pockets of nearly pristine solution located about the initial solution interface (Fig. 4.3g-j). Finally, at late time, the finger structure becomes 'tree-like' with a branching pattern that has greater lateral travel than a early time. This final convective structure remains long after motion has stopped, diffusion now acting to slowly uniformize the field (Fig. 4.3l).

4.4 Numerical Modeling

4.4.1 Spatial and temporal discretization, iteration strategy and used solvers

To solve successfully the DDFC problem a sufficiently fine spatial discretization is fundamental. Because most transfer in a DDFC system is a result of convection, small finger dimensions may evolve. Damping effects by artificial numerical dispersion should be hold down on a lowest level to resolve accurately the minimum finger dimension occurring in a DDFC simulation. A further important point in DDFC computations refers to arising numerical perturbations which can affect the evolution of DDFC[5]. It is to be expected that uniform and aligned structured meshes with square elements can minimize uncontrollable numerical perturbations during the simulation.

Quadrilateral meshes with different resolution were studied by Hughes *et al.*[7]. It can be recognized as a stepwise global refinement Υ_l of meshing according to

$$\Upsilon_l \qquad l = 0, 1, 2, \ldots \tag{4-3}$$

where l is the refinement level. In the global refinement Υ_l of the mesh starting with the 2D discretization Υ_0 each quadrilateral is subdivided into four equally sized quadrilaterals. The number of quadrilaterals NE and number of nodes NP then increase according to the refinement level $l = 0, 1, \ldots$:

$$\begin{aligned} NE &= 41 \cdot 2^{(10+2l)} \\ NP &= NE + 105 \cdot 2^{(2+l)} + 1 \end{aligned} \tag{4-4}$$

Table 4.5 summarizes the mesh properties up to level 4.

Table 4.5 Meshes according to refinement levels *l*

Level *l*	Used FEFLOW mesh	Number of elements (*NE*)	Number of nodes (*NP*)	Spatial increment [mm]
0	-	41,984 (256 · 164)	42,405 (257 · 165)	0.992
1	-	167,936 (512 · 328)	168,777 (513 · 329)	0.496
2	**mesh A**	671,744 (1024 · 656)	673,425 (1025 · 657)	0.248
3	**mesh B**	2,686,976 (2048 · 1312)	2,690,337 (2049 · 1313)	0.124
4	-	10,747,904 (4096 · 2624)	10,754,625 (4097 · 2625)	0.062

Hughes *et al.*[7] simulated meshes at levels l of 0, 1 and 2. Their computations with the finest mesh at $l = 2$ agreed rather well with Pringle *et al.*'s Hele-Shaw experiments. They found that the coarser discretizations with $l = 0$ and $l = 1$ are inappropriate to model the finger development with a reasonable accuracy. However, even their finest discretization at $l = 2$ with a spatial increment of 0.248 mm is still larger than the pixel size with 0.154 mm of the Hele-Shaw experiment by a factor of 1.6. More refined meshes could not be simulated by Hughes *et al.*[7] due to their computational limitations.

In the present FEFLOW simulations we recompute the DDFC problem in using Hughes *et al.*'s finest 671,744-element mesh at $l = 2$. Additionally, FEFLOW simulations are performed on a further refined mesh having the refinement level $l = 3$. In the following FEFLOW simulations we denote these meshes as mesh A consisting of 1024 · 656 quadrilateral elements (673,424 nodes) and mesh B consisting of 2048 · 1312 quadrilateral elements (2,690,337 nodes), see Table 4.5. Mesh A is comparable to the finest spatial discretization used by Hughes *et al.*[7]. Note that the high-resolution mesh B is more refined than the length scales of in the Hele-Shaw experiment. The spatial increment in mesh B with 0.124 mm is smaller than the pixel size of the Hele-Shaw experiment with 0.154 mm.

It is important to note that mesh B requires 64-bit execution because the needed RAM is on the order of 4 GB. In the present study we prefer a fully implicit forward Euler/backward Euler (FE/BE) adaptive error-controlled predictor-corrector time stepping strategy[5] and parallel computations. A sequential iterative Picard-type strategy for the flow and transport equations (4-1) is performed as thoroughly described in Diersch[4]. The adaptive time stepping and iterative procedure is controlled via a RMS error criterion using 10^{-4} as dimensionless tolerance length. While the flow equations are solved by the algebraic multigrid solver SAMG (Stüben[10], Diersch[3]), the transport equations are solved by an iterative BiCGSTAB equation solver with an incomplete LU preconditioning. Both solvers are applied with a reduced stop criteria of 10^{-12} to termi-

nate iterations in solving the sparse finite-element matrix equation systems. Table 4.6 summarizes the numerical features used in the FEFLOW simulations.

Table 4.6 Numerical features used in the FEFLOW simulations

Feature	Description
Spatial discretization	Structured meshes A and B of quadrilateral bi-linear finite elements
Temporal discretization	Implicit predictor-corrector FE/BE time stepping method with RMS error criterion of 10^{-4}
Iteration method	Sequential iterative Picard-type terminated with RMS error criterion of 10^{-4}
Iterative sparse matrix solvers	*Flow equations (symmetric):* SAMG with stop criteria 10^{-12} *Transport equations (unsymmetric):* BiCGSTAB with stop criteria 10^{-12} using incomplete LU preconditioning
Parallelization	Assembly of finite element matrices OpenMP for SAMG equation solver Auto-parallelizing compiler options used for BiCGSTAB equation solver
Address space	64-bit

4.4.2 Boundary and initial conditions, perturbation of initial solute interface

All external boundary faces represent no-flux conditions both for fluid flow and for species mass transport. This is automatically satisfied by natural (zero-value) Neumann-type boundary conditions and no specifications are required. But, there is one exception. Because the storativity S is zero in the flow equation (4-1) there is no more a regular time-derivative term and the flow equations should be linked with a Dirichlet-type boundary condition to stabilize the numerical solution. It is sufficient to specify at least one node with an arbitrary head value h. While Hughes *et al.*[7] specified both the upper left and upper right corner nodes with values for pressure and species concentrations, in our simulations only the node at the centre of the mesh is specified with a hydraulic head h of 0.0, no extra boundary conditions are introduced for the species concentrations.

At initial time t_o the three species are distributed as follows within the 2D domain $(0 \le x_1 \le L, 0 \le x_2 \le H)$ in a layered configuration, where the solute interface is located at $x_2 = 0$ (see Fig. 4.1):

$$C_s(\boldsymbol{x}, t_o) = \begin{cases} C_{ss}\left(0 \le x_1 \le L, 0 \le x_2 \le \frac{H}{2}\right) \\ C_{s0}\left(0 \le x_1 \le L, -\frac{H}{2} \le x_2 < 0\right) \end{cases} \quad (4\text{-}5a)$$

$$C_c(\boldsymbol{x}, t_o) = \begin{cases} C_{c0}\left(0 \le x_1 \le L,\ 0 < x_2 \le \frac{H}{2}\right) \\ C_{cs}\left(0 \le x_1 \le L,\ -\frac{H}{2} \le x_2 \le 0\right) \end{cases} \quad \text{(4-5b)}$$

$$C_{\text{dye}}(\boldsymbol{x}, t_o) = \begin{cases} C_{\text{dye}0}\left(0 \le x_1 \le L,\ 0 < x_2 \le \frac{H}{2}\right) \\ C_{\text{dye}s}\left(0 \le x_1 \le L,\ -\frac{H}{2} \le x_2 \le 0\right) \end{cases} \quad \text{(4-5c)}$$

The present finger convection problem is very sensitive with respect to perturbations. Pringle *et al.*[9] expended significant effort in minimizing initial perturbations for the Hele-Shaw experiment. Although the thickness of the solute interface was small (about 1 mm), perturbations at the start of the experiment could not be avoided. They were seeds for initial finger developments. For the numerical simulation a control of such type of initial seeds for finger developments is needed. This should be mimicked by the following random procedure as proposed by Hughes *et al.*[7].

Random noise with a mean of zero and maximum amplitude of 0.5% of maximum initial concentrations C_{ks} is applied for both sucrose and sodium chloride at the initial solution interface. Dye concentrations at the interface are not perturbed. To develop initial perturbations for sucrose and sodium chloride their nodal concentrations at nodes sharing the solute interface at $x_2 = 0$ are modified as follows:

DO FOR ALL INTERFACE NODES I {
  RN1 = RANDOM NUMBER BETWEEN 0 AND 1
  IF (RN1 < 0.5) {
    $C_s(x_1^I, x_2^I = 0, t_o) = 0.01 \cdot \text{RN1} \cdot C_{ss}$
  }
  ELSE {
    $C_s(x_1^I, x_2^I = 0, t_o) = C_{ss}$
  }

  RN2 = RANDOM NUMBER BETWEEN 0 AND 1
  IF (RN2 < 0.5) {
    $C_c(x_1^I, x_2^I = 0, t_o) = 0.01 \cdot \text{RN2} \cdot C_{cs}$
  }
  ELSE {
    $C_c(x_1^I, x_2^I = 0, t_o) = C_{cs}$
  }
}

where x_1^I and x_2^I correspond to the x_1 - and x_2 -coordinates of node I.

To have comparable initial perturbations for both mesh A and B the perturbation procedure at the interface nodes is firstly applied to mesh A. This perturbation pattern is then inherited to mesh B when mesh A is globally refined from level $l = 2$ to level $l = 3$ by subdivision (each quadrilateral element is subdivided into four quadrilateral elements). However, in a last case we will deviate from this inherited perturbation and present simulations with initial perturbations directly generated on the refined mesh B.

4.5 Results

Table 4.7 summarizes the performance results

attained in the FEFLOW simulations for meshes A and B. While the run time of mesh A required about 1 day on a double processor machine (6 GB RAM, 3 GHz clock speed, MS XP Enterprise x64 Edition), mesh B took a run time of about one week. It is interesting to note that the parallel-version of the SAMG solver have accelerated the simulation time by a factor of about two as indicated in Table 4.7. The simulation of mesh A and B required 3205 and 3626 adaptive time steps, respectively. The time step history for the mesh B simulation is plotted in Fig. 4.4.

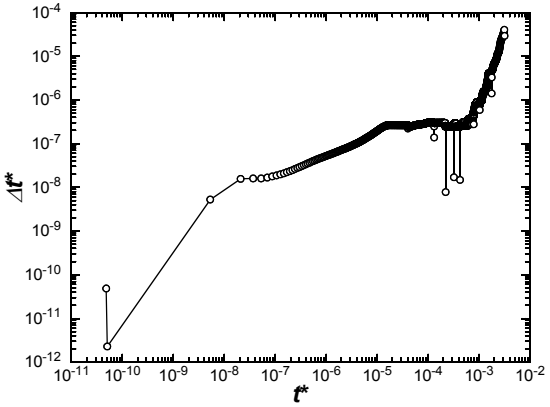

Figure 4.4 Time stepping history for mesh B.

Figure 4.6 shows the FEFLOW-simulated dye concentrations for mesh A at the same dimensionless times of Pringle *et al.*[9] (cf. Table 4.4). The results agree rather well with the computations obtained by Hughes *et al.*[7] as displayed in Fig. 4.7. Qualitatively, the numerical results are similar to the experimental results as seen in Fig. 4.8 in comparison to the mesh B results. As already indicated by Hughes *et al.*[7] the experimental vertical finger evolution appears to be slightly ahead of the simulated fingers.

Table 4.7 FEFLOW performance results

Mesh	Number of adaptive time steps	CPU time[a)]
A	3205	~1 day (~2.5 days)[b)]
B	3626	~7.5 days (~16 days)[b)]

a) Approximate total simulate time on a double processor server with 3 GHz clock speed, 6 GB RAM, MS Windows XP Enterprise x64 Edition, two single-core Intel Xeon CPUs. Executable and libraries are compiler-optimized using options of auto-parallelization.
b) SAMG solver without OpenMP parallelization.

A more quantitative comparison can be done by using the vertical mass flux exemplified for the dye concentrations. A normalized mass transfer of dye upward across the centerline of the cell can be defined according to

$$M^* = M/M_o \tag{4-6}$$

where M is the dye mass above the centerline of the Hele-Shaw cell at time t^* and M_o is the total dye mass in the cell. Numerical results compare reasonably well to observed values of M^* as depicted in Fig. 4.5. As

also seen there FEFLOW's and Hughes *et al.*[7]'s results agree very well. Their agreement with the Hele-Shaw experiment is acceptable until $t^* = 1 \cdot 10^{-3}$. After $t^* = 1 \cdot 10^{-3}$, the simulated mass transfer M^* is less than observed mass transfer. Larger percent errors at early times are an artifact of small M^* values and represent small absolute differences in mass transfer (e.g., 0.011 observed and 0.017 simulated) influenced by the initial perturbation at the interface nodes for the given spatial discretization. Note further that the simulated mass transfer M^* did not changed anymore if using a more refined mesh (cf. mesh A and mesh B results in Fig. 4.5). It indicates that the numerical accuracy with respect to the mass transfer is sufficiently achieved at a lower refinement level as given for mesh A. Table 4.8 compares the measured mass transfer M^* against the FEFLOW results obtained for mesh B.

A comparison of the finger evolution for the two meshes A and B are exhibited in Fig. 4.9. It reveals a slightly faster finger development for the more refined mesh B compared to the coarser mesh A. While for mesh A at the front of the fingers small wiggles in the numerical solution could be observed at early times (indicated by white color spots in the fringed distributions of Fig. 4.9 left), the solution for mesh B is fully wiggle-free.

We also studied the influence of the Oberbeck-Boussinesq approximation and the fluid viscosity on the simulation results. Noticeable but not significant differences exist in the simulated finger patterns when comparing the solutions with and without the Oberbeck-Boussinesq approximation as seen in Fig. 4.10. More influence on the finger pattern results from the fluid viscosity effect. As evidenced in Fig. 4.11 a constant viscosity solution produces a slightly faster finger development as for the case with a variable (concentration-dependent) viscosity.

Table 4.8 Measured vs. simulated *M

	t^*	M^*	
		Hele-Shaw experiment Pringle *et al.*[9]	FEFLOW mesh B
a	$4.03 \cdot 10^{-5}$	0.01	0.02
b	$1.31 \cdot 10^{-4}$	0.05	0.05
c	$2.21 \cdot 10^{-4}$	0.10	0.08
d	$3.22 \cdot 10^{-4}$	0.15	0.12
e	$4.23 \cdot 10^{-4}$	0.20	0.16
f	$5.24 \cdot 10^{-4}$	0.25	0.20
g	$6.04 \cdot 10^{-4}$	0.30	0.23
h	$7.25 \cdot 10^{-4}$	0.35	0.28
i	$7.85 \cdot 10^{-4}$	0.40	0.30
j	$1.03 \cdot 10^{-3}$	0.45	0.36
k	$1.77 \cdot 10^{-3}$	0.50	0.41
l	$3.17 \cdot 10^{-3}$	0.51	0.42

The influence of the initial perturbation on the finger development can be seen in Fig. 4.12 resulting for a mesh B simulation. On the one hand, it shows the finger pattern evolving from a perturbation which has

been inherited from the coarser mesh A. On the other hand, it also exhibits the case of initial perturbations which has been directly generated on the refined mesh B. As revealed the perturbation significantly affects the local finger structure of the convection system while the average quantities, such as the mass transfer, remain comparable. In this case the growth of fingers in the vertical extent is slightly slower because the perturbation of the interface nodes on the refined mesh has a smaller scale (nodal spacing is smaller) compared to the perturbation inherited from the coarser mesh (spacing of the perturbed nodes is larger).

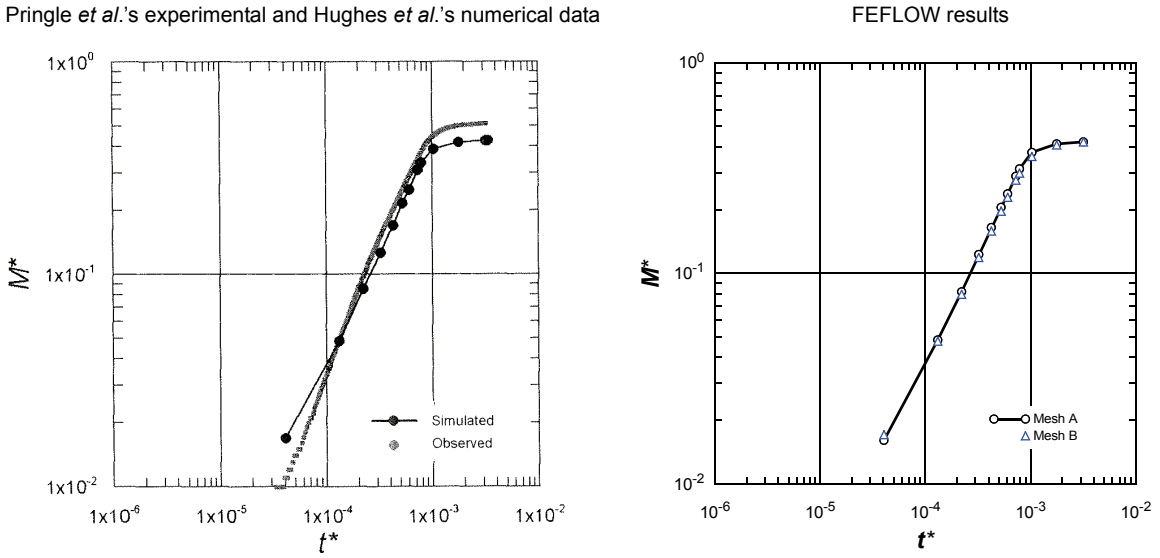

Figure 4.5 Normalized mass transfer across the center line M^*. Comparison of observed data taken by Pringle *et al.*[9] and numerical results by Hughes *et al.*[7] (left) with FEFLOW results computed for meshes A and B (right).

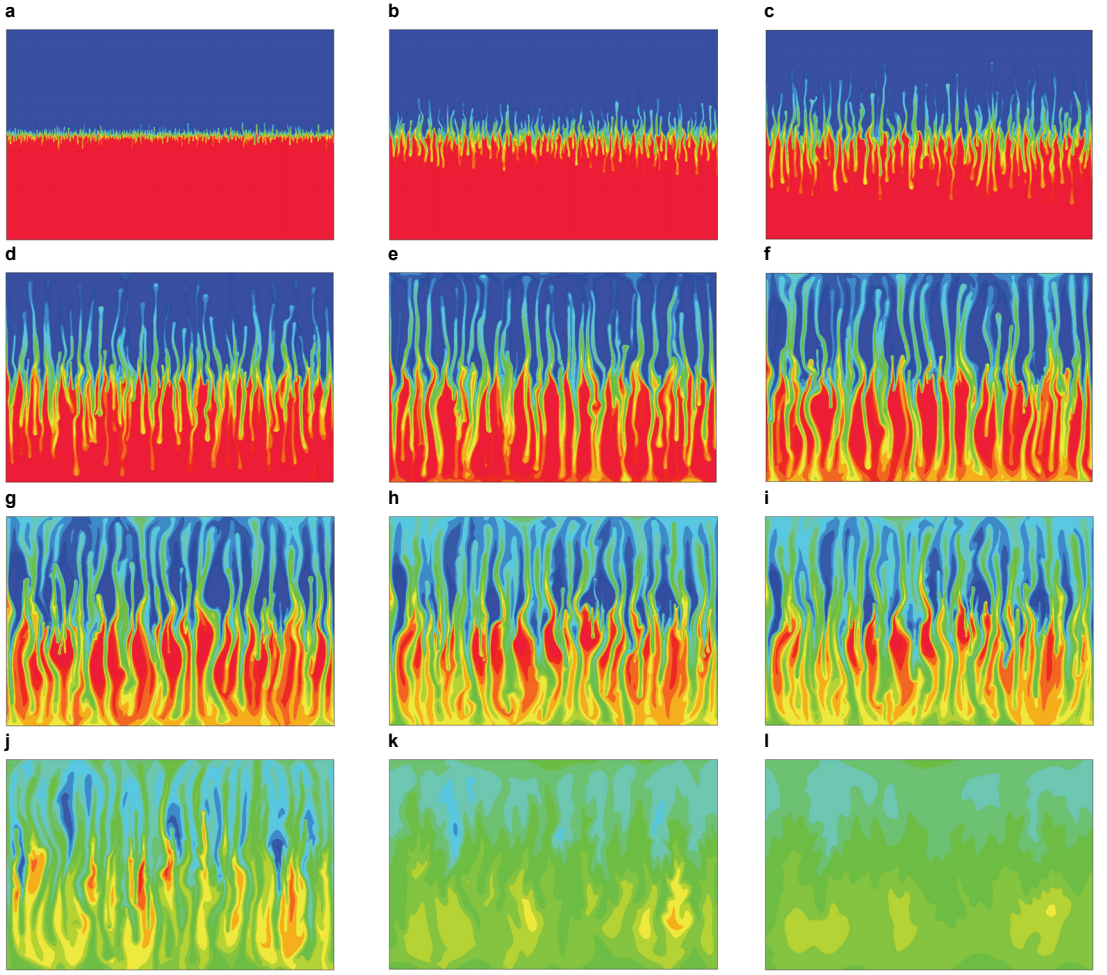

Figure 4.6 FEFLOW results simulated with mesh A for the dye component at (a) $t^* = 4.03 \cdot 10^{-5}$, (b) $t^* = 1.31 \cdot 10^{-4}$, (c) $t^* = 2.21 \cdot 10^{-4}$, (d) $t^* = 3.22 \cdot 10^{-4}$, (e) $t^* = 4.23 \cdot 10^{-4}$, (f) $t^* = 5.24 \cdot 10^{-4}$, (g) $t^* = 6.04 \cdot 10^{-4}$, (h) $t^* = 7.25 \cdot 10^{-4}$, (i) $t^* = 7.85 \cdot 10^{-4}$, (j) $t^* = 1.03 \cdot 10^{-3}$, (k) $t^* = 1.77 \cdot 10^{-3}$, and (l) $t^* = 3.17 \cdot 10^{-3}$. ($t^* = tD_c^d / H^2$ dimensionless time). Color sequence blue-green-yellow-orange-red depicts normalized dye concentration from 0 to 1.

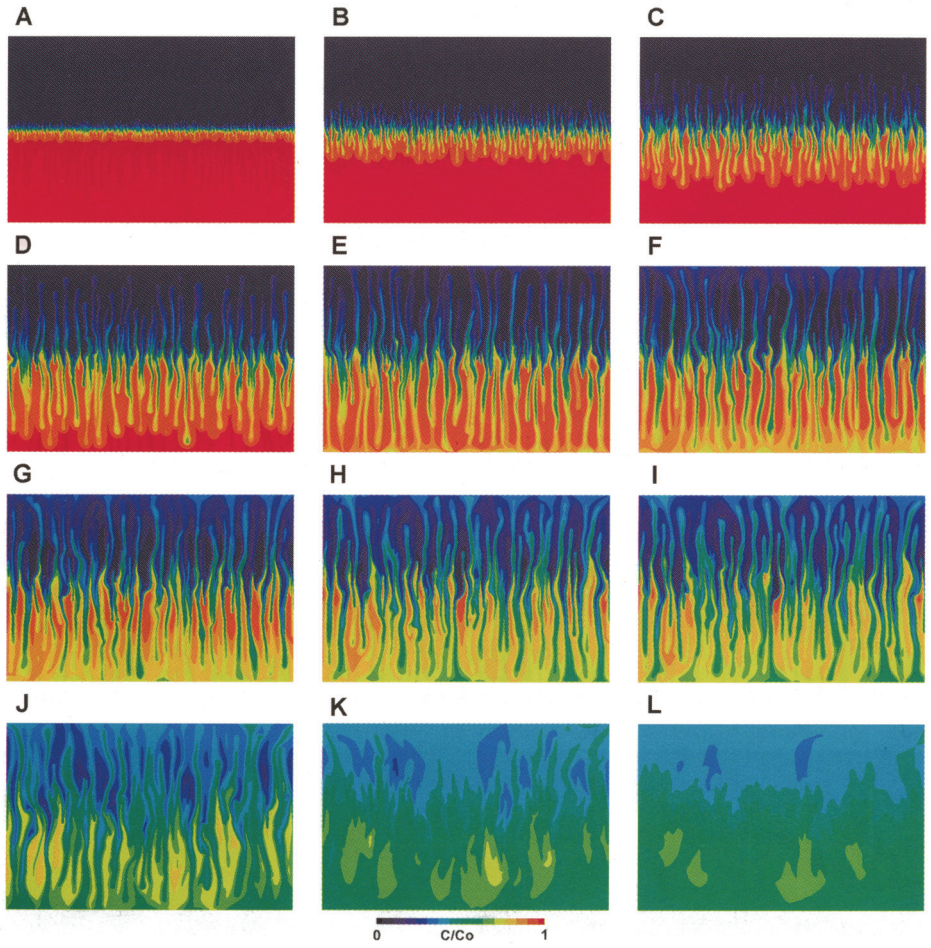

Figure 4.7 Simulated results by Hughes *et al.*[7] for the dye component at (a) $t^* = 4.03 \cdot 10^{-5}$, (b) $t^* = 1.31 \cdot 10^{-4}$, (c) $t^* = 2.21 \cdot 10^{-4}$, (d) $t^* = 3.22 \cdot 10^{-4}$, (e) $t^* = 4.23 \cdot 10^{-4}$, (f) $t^* = 5.24 \cdot 10^{-4}$, (g) $t^* = 6.04 \cdot 10^{-4}$, (h) $t^* = 7.25 \cdot 10^{-4}$, (i) $t^* = 7.85 \cdot 10^{-4}$, (j) $t^* = 1.03 \cdot 10^{-3}$, (k) $t^* = 1.77 \cdot 10^{-3}$, and (l) $t^* = 3.17 \cdot 10^{-3}$. ($t^* = tD_c^d/H^2$ dimensionless time). Color sequence black-blue-green-yellow-orange-red depicts normalized dye concentration from 0 to 1. Figure taken from Hughes *et al.*[7].

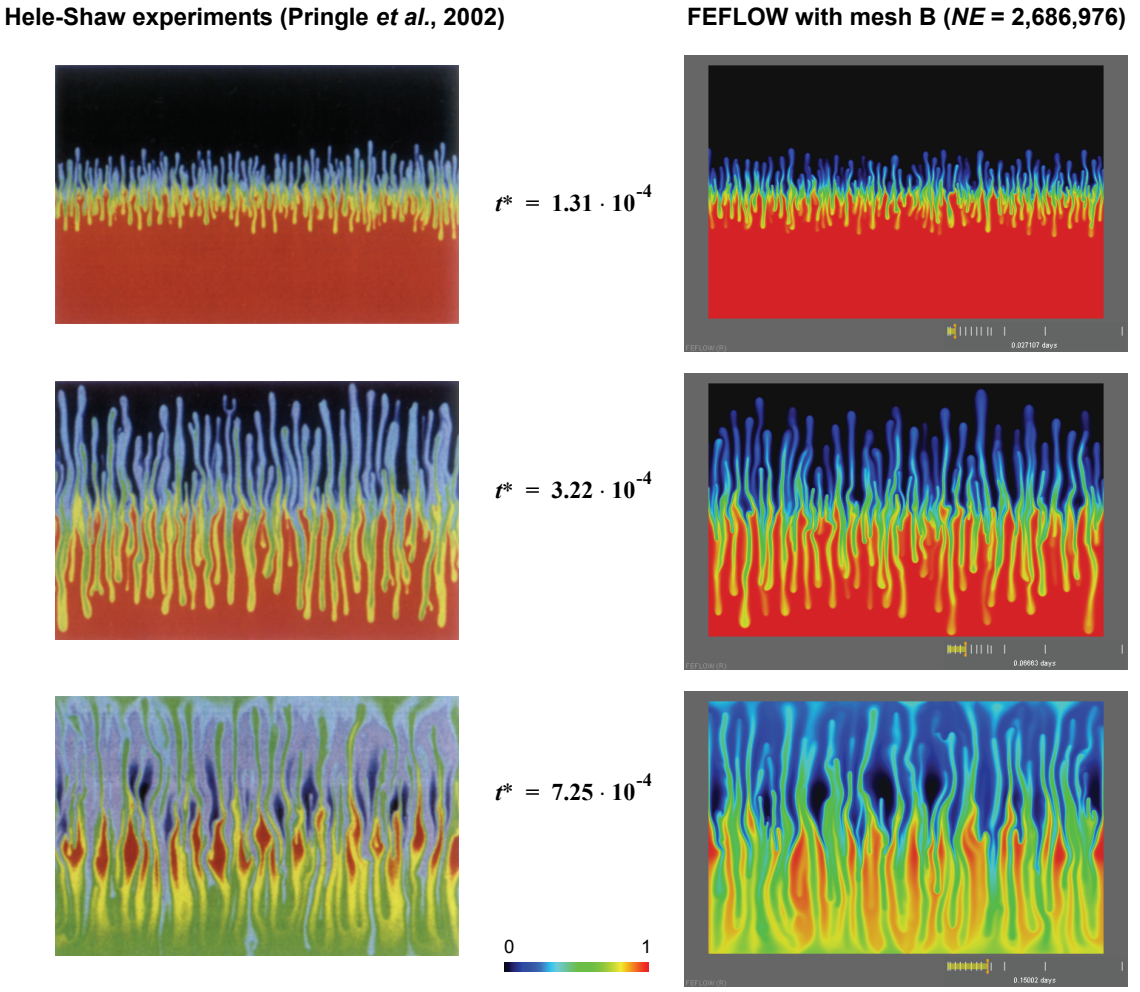

Figure 4.8 Comparison of Hele-Shaw experiments from Pringle *et al.*[9] to FEFLOW results simulated with mesh B for the dye component at different times t^*. ($t^* = tD_c^d/H^2$ dimensionless time). Case of variable fluid viscosity $f_\mu = \mu_o/\mu(C_k)$. Color sequence black-blue-green-yellow-orange-red depicts normalized dye concentration from 0 to 1.

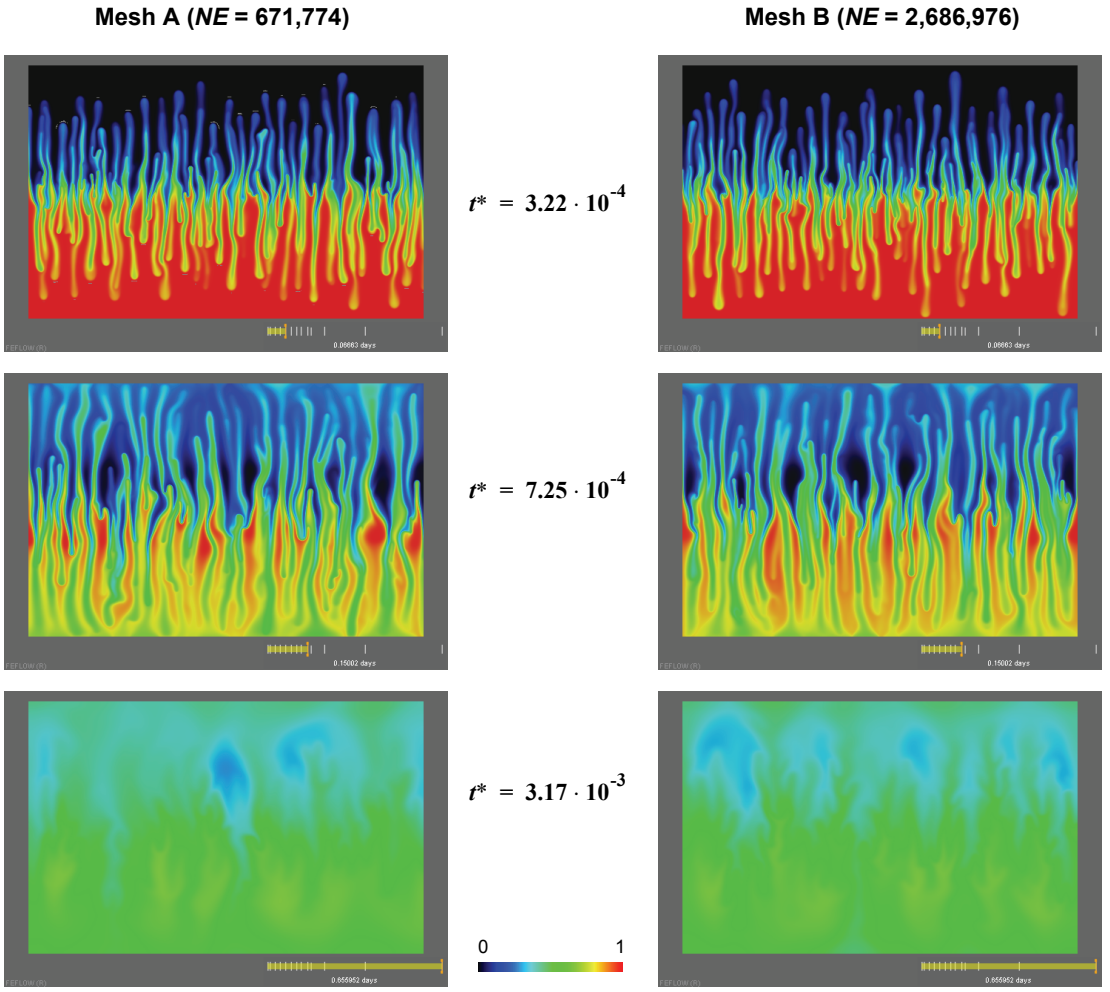

Figure 4.9 FEFLOW results simulated for the dye component at different times t^*. ($t^* = tD_c^d/H^2$ dimensionless time). Comparison between mesh A (left) and mesh B (right) for the case of variable fluid viscosity $f_\mu = \mu_o/\mu(C_k)$. Color sequence black-blue-green-yellow-orange-red depicts normalized dye concentration from 0 to 1.

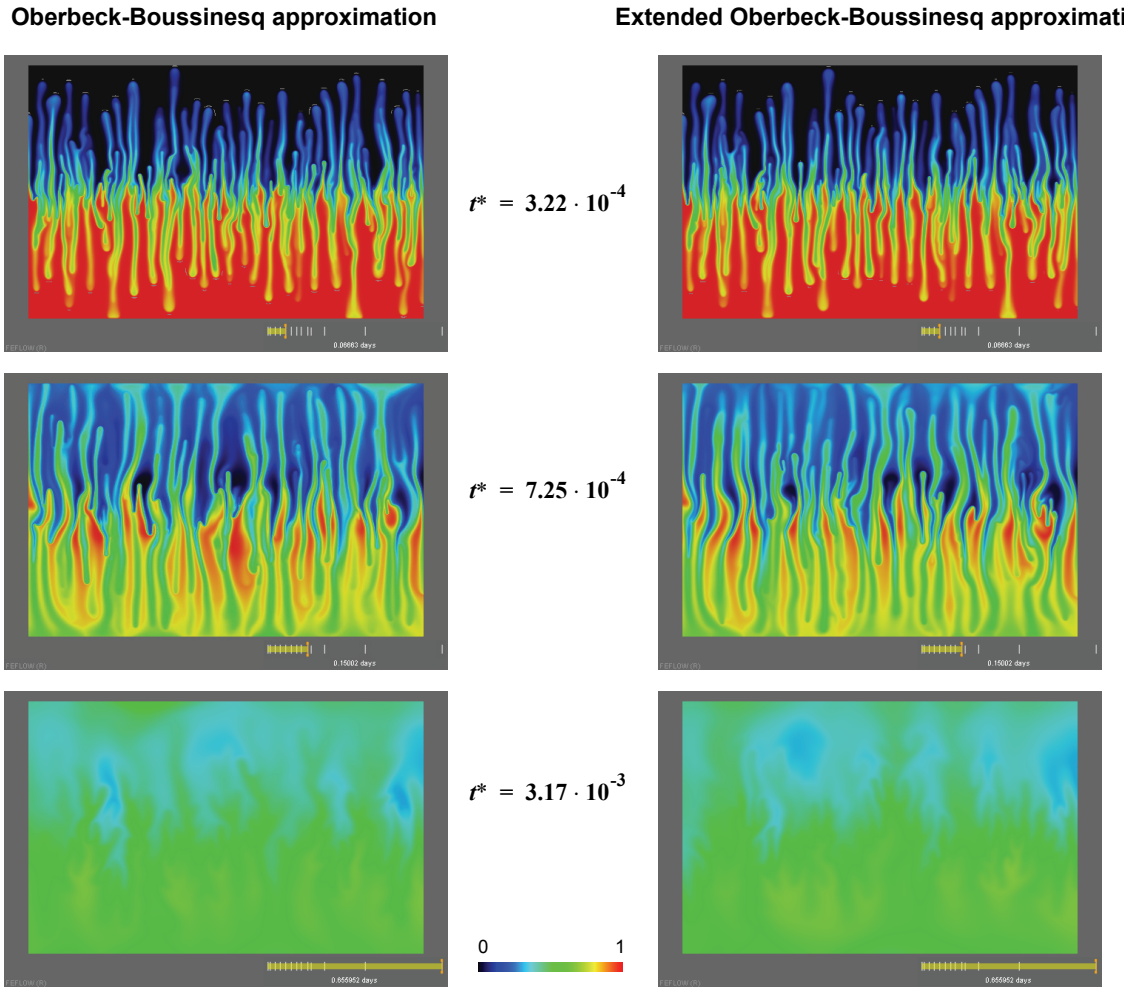

Figure 4.10 FEFLOW results simulated with mesh A for the dye component at different times t^*. ($t^* = tD_c^d/H^2$ dimensionless time). Comparison of Oberbeck-Boussinesq approximation $Q_{\mathrm{EOB}} \equiv 0$ (left) to the Extended Oberbeck-Boussinesq approximation $Q_{\mathrm{EOB}} \neq 0$ (right) for the case of constant fluid viscosity $f_\mu \equiv 1$. Color sequence black-blue-green-yellow-orange-red depicts normalized dye concentration from 0 to 1.

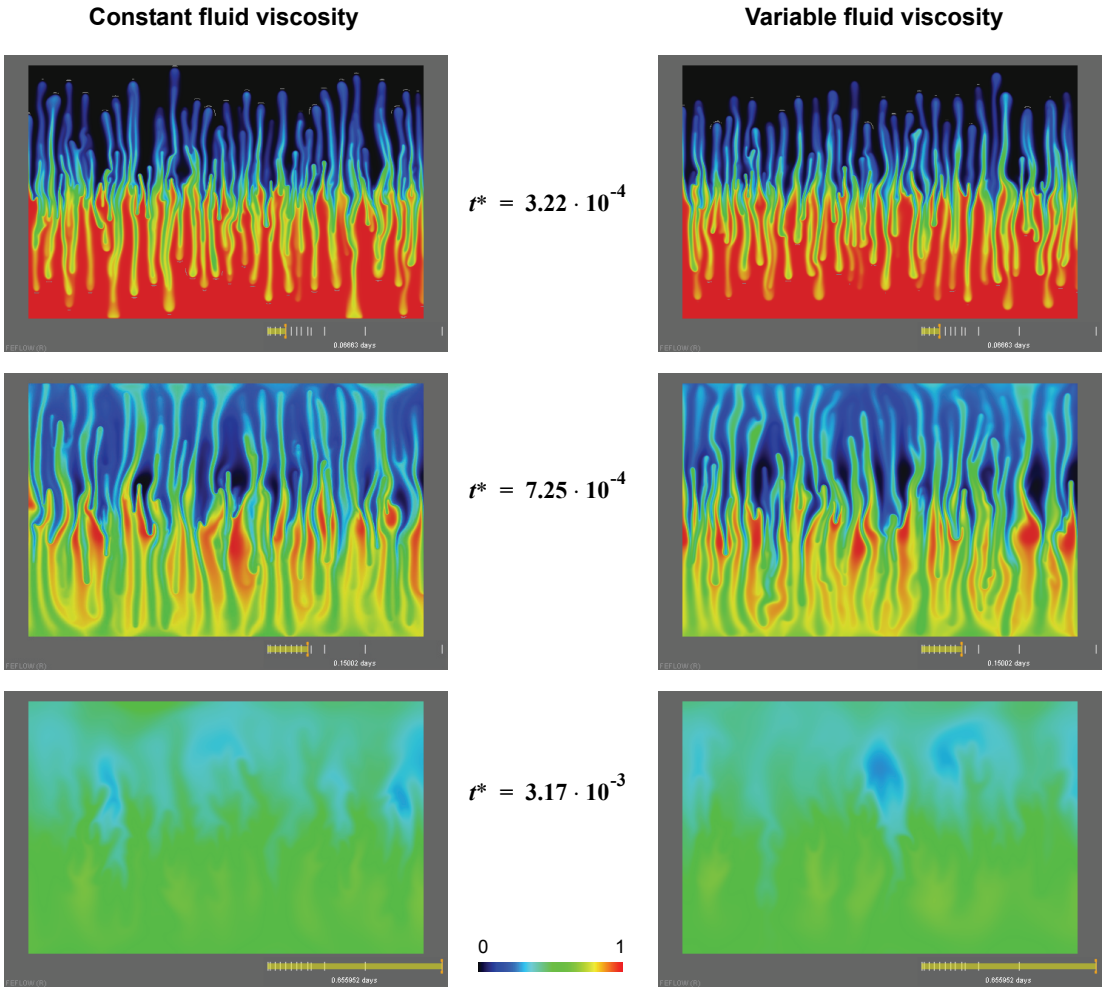

Figure 4.11 FEFLOW results simulated with mesh A for the dye component at different times t^*. ($t^* = tD_c^d/H^2$ dimensionless time). Comparison of constant fluid viscosity $f_\mu \equiv 1$ (left) to the variable fluid viscosity case $f_\mu = \mu_o/\mu(C_k)$ (right). Color sequence black-blue-green-yellow-orange-red depicts normalized dye concentration from 0 to 1.

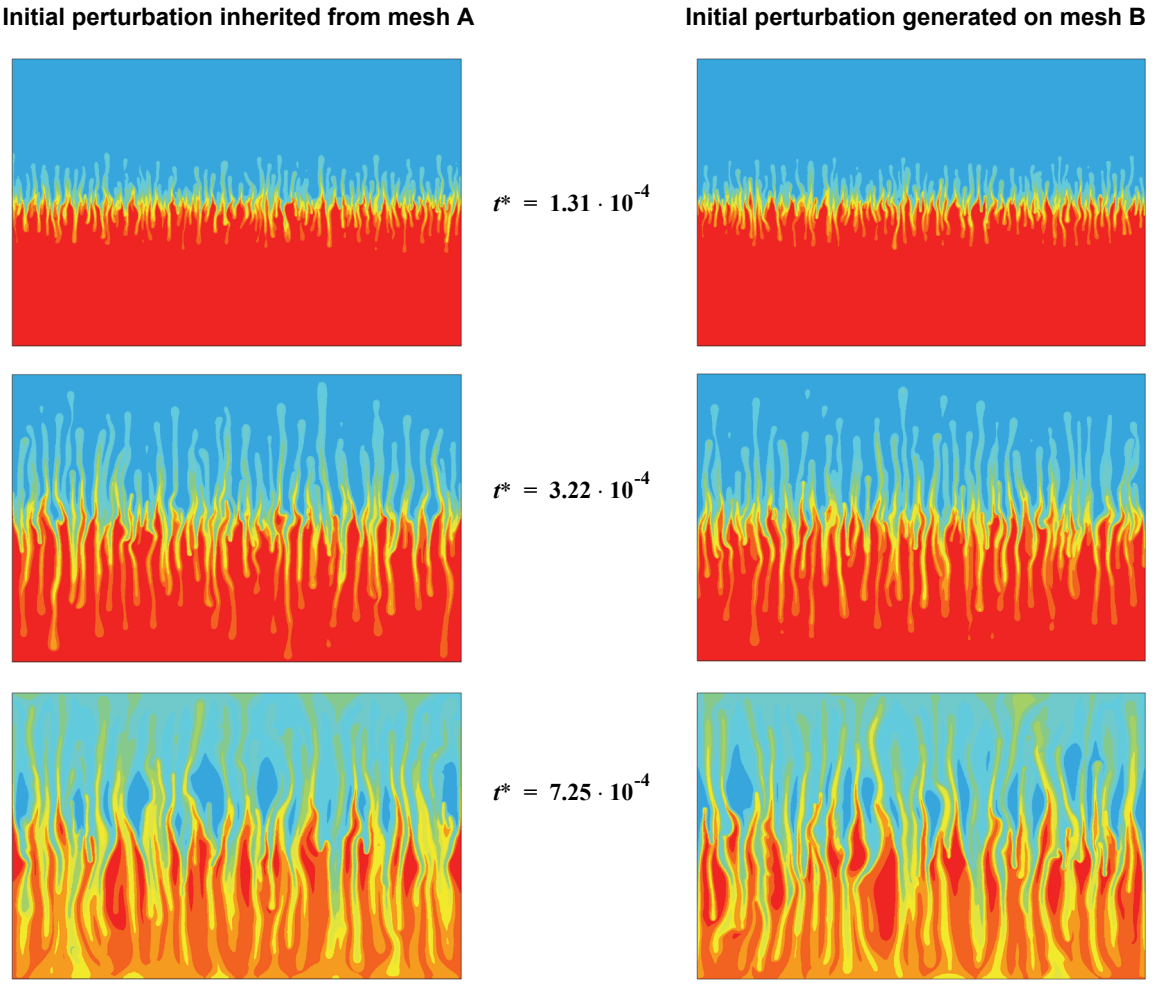

Figure 4.12 FEFLOW results simulated with mesh B for the dye component at different times t^*. ($t^* = tD_c^d/H^2$ dimensionless time). Influence of perturbation applied to the initial solution interface. Case of variable fluid viscosity $f_\mu = \mu_o/\mu(C_k)$. Color sequence blue-green-yellow-orange-red depicts normalized dye concentration from 0 to 1.

4.6 Conclusions

The FEFLOW simulator provides the capability to simulate complex DDFC phenomena for fine mesh resolutions. For each species (and in addition temperature in case of need) multiple density expansions and viscosity change parameters can be specified. The viscosity relationship can be freely defined for species (and temperature) via a flexible formula editor. FEFLOW is parallelized and uses an efficient algebraic multigrid solver to speed-up the computations.

The FEFLOW simulations have been tested for a 2D DDFC problem against the Hele-Shaw experiment done by Pringle *et al.*[9] and the numerical study performed by Hughes *et al.*[7], where good agreements could be found. Structured meshes (A and B) of higher resolution at a refinement level of 2 and 3 consisting of 673,425 and 2,690,337 nodes were applied. The finest discretization B with 0.124 mm is smaller than the pixel size of the Hele-Shaw experiment with 0.154 mm.

Within the extensive numerical investigations we studied the influence of following features:

- mesh effects,
- computational acceleration by parallelization,
- viscosity effects,
- mass transfer across the centerline,
- extensions to the Oberbeck-Boussinesq approximation,
- perturbation of the initial solution interface.

For this complex and difficult problem class of convection phenomena FEFLOW has shown a robust and efficient simulator in 2D applications. Even 3D DDFC applications seem to be possible in the future.

Notation

Roman letters

C	ML^{-3}	concentration;
$\boldsymbol{D}$	L^2T^{-1}	tensor of hydrodynamic dispersion;
D^d	L^2T^{-1}	coefficient of molecular diffusion;
$\boldsymbol{e}$	l	gravitational unit vector;
f_μ	l	fluid viscosity relation function;
g	LT^{-2}	gravitational acceleration;
H	L	cell height;
h	L	hydraulic (piezometric) head;
$\boldsymbol{I}$	l	unit vector;
$\boldsymbol{K}$	LT^{-1}	tensor of hydraulic conductivity;
K	LT^{-1}	constant hydraulic conductivity;
k	L^2	intrinsic permeability;
L	L	cell length;
Le		Lewis number;
l		mesh level;
M	M	mass;
M^*	l	dimensionless mass;
N		maximum number of species;
NE		number of elements;
NP		number of nodes (points);
Q	T^{-1}	sink/source term;
Q_{EOB}	T^{-1}	extended Oberbeck-Boussinesq approximation term;
$\boldsymbol{q}$	LT^{-1}	Darcy velocity;
R	$ML^{-3}T^{-1}$	reaction term;
Ra		Rayleigh number;

R_ρ		Turner number;
S	L^{-1}	storage coefficient / storativity;
t	T	time;
t^*	1	dimensionless time;
$\boldsymbol{x}$	L	global Cartesian coordinate vector;
x_1, x_2	L	2D Cartesian coordinates;

Greek letters

α	1	density difference ratio;
β_L, β_T	L	longitudinal and transverse dispersivity, respectively;
ε	1	porosity, void space;
ϑ	L^2T^{-1}	coefficient of fluid viscosity change;
μ	$ML^{-1}T^{-1}$	dynamic viscosity of fluid;
ρ	ML^{-3}	fluid density;
Υ		global refinement;
∇	L^{-1}	Nabla (vector) operator;

Subscripts

c	chloride;
dye	dye;
k	species indicator;
0	reference / initial;
s	sucrose;
s	maximum;

Superscripts

d	diffusive;
I	nodal index;

Abbreviations

2D	two-dimensional;
3D	three-dimensional;
CPU	central processing unit
DDC	double-diffusive convection;
DDFC	double-diffusive finger convection;
FE/BE	forward Euler/backward Euler scheme;
GB	gigabyte;
EOB	extended Oberbeck-Boussinesq approximation;
RAM	random access memory;
RMS	root-mean square;

References

1. Cooper, C.A., Glass, R.J. and Tyler, S.W. Experimental investigation of stability boundary for double-diffusive finger convection in a Hele-Shaw cell. *Water Resour. Res.* **33** (1997), 517-526.
2. Cooper, C.A., Glass, R.J. and Tyler, S.W. Effect of buoyancy ratio on the development of double-diffusive finger convection in a Hele-Shaw cell. *Water Resour. Res.* **37** (2001)9, 2323-2332.
3. Diersch, H.-J.G. Using and testing the algebraic multigrid equation solver SAMG in FEFLOW. White Papers Vol. III, pp. 25-37, 2004, WASY Berlin, Germany.
4. Diersch, H.-J.G. Reactive multi-species transport. White Papers Vol. IV, pp. 5-56, 2005, WASY Berlin, Germany.
5. Diersch, H.-J.G. and Kolditz, O. Variable-density flow and transport in porous media: approaches and challenges. A*dv. Water Resour.* **25** (2002), 899-944. (also published in FEFLOW White Papers Vol. II, Chapter 1, 2004, pp. 5-101, WASY Berlin, Germany).
6. Hughes, J.D. and Sanford, W.E. SUTRA-MS, A version of SUTRA modified to simulate heat and multiple-solute transport. USGS, Open-File Report 2004-1207, Reston, Virginia, 2004, 141pp.

7. Hughes, J.D., Sanford, W.E. and Vacher, H.L. Numerical simulation of double-diffusive finger convection. *Water Resour. Res.* **41** (2005), W01019, doi:10.1029/2003WR002777.
8. Nield, D.A. and Bejan, A. *Convection in porous media*. Springer, New York, 1992.
9. Pringle, S.E., Glass, R.J. and Cooper, C.A. Double-diffusive finger convection in a Hele-Shaw cell: An experiment exploring the evolution of concentration fields, length scales and mass transfer. *Transp. Porous Media* **47** (2002)2, 195-214.
10. Stüben, K. User's manual SAMG, Release 2.1, Fraunhofer Institute SCAI, 2002, St. Augustin, Germany.
11. Voss, C.I. and Provos, A.M. SUTRA - A model for saturated-unsaturated, variable-density groundwater flow with solute or energy transport, U.S. Geol. Surv. Water Resour. Invest. Rep., 02-4231, 2002, 260 pp.

Subject Index

S

T

V

Subject Index

Author Index

Author Index